NIST Technical Note 1752

Digital image correlation measurements during gusset plate connection testing to structural failure.

Mark A. Iadicola

http://dx.doi.org/10.6028/NIST.TN.1752

National Institute of
Standards and Technology
U.S. Department of Commerce

NIST Technical Note 1752

Digital image correlation measurements during gusset plate connection testing to structural failure.

Mark A. Iadicola
Metallurgy Division
Material Measurement Laboratory

http://dx.doi.org/10.6028/NIST.TN.1752

August 2012

U.S. Department of Commerce
Rebecca Blank, Acting Secretary

National Institute of Standards and Technology
Patrick D. Gallagher, Under Secretary of Commerce for Standards and Technology and Director

National Institute of Standards and Technology Technical Note 1752
Natl. Inst. Stand. Technol. Technical Note 1752, 118 pages (August 2012)
CODEN: NTNOEF

Abstract

This report describes the use of three-dimensional (3D) digital image correlation to measure the shape, displacement, and in-plane strain fields, during testing of gusset plate structural connections. Twelve full-scale bridge gusset plate connections of various geometries and boundary conditions were tested at the the Federal Highway Administration (FHWA) Turner-Fairbank Highway Research Center (Ocel et al., 2012). These experiments are part of the verification of numerical models as part of the National Cooperative Highway Research Program (NCHRP) Project 12-84 "Guidelines for the Load and Resistance Factor Design and Rating of Riveted and Bolted Gusset Plate Connections for Steel Bridges". The measurements described here are in regards to the tests performed to failure (i.e., maximum load carrying capacity of the connection). During each of the twelve tests to failure, a series (typically about 150) of image pairs were taken for subsequent digital image correlation analysis. Although all of the image pairs were processed, only a very small portion of the results are explicitly presented here. General access to the overall data set will be given to other researchers. Overall, the measurements showed reasonable uncertainties on the order of $\pm$ 175 μm/m of maximum in-plane shear strain, and the measured out of plane initial shapes of the plates typically matched qualitative inspections of the connections.

In this report, the layout, calibration, and measurement procedure associated with the digital image correlation system are described in detail to aid in understanding of the results. The results shown here include a sample of the measured and derived variables for one experiment at two conditions, to inform the reader of the type of data that is available. The results also include an abbreviated set of results that show the evolution of the out of plane shape and maximum shear strain field at four points in loading from the initial condition to failure. These are very useful in visualizing the mechanisms (buckling and/or shear failure of the plate) that lead to eventual failure of the connection. The evolution of strain bands of maximum in-plane shear is seen quite clearly in many of the plates. These localized bands of deformation frequently extended from the bolt lines of one member to another member through the large open areas of the plate. Comparison between all of the plates at failure, in terms of the maximum in-plane strain fields, is also presented. This comparison helps delineate plates that failed after significant shearing versus the ones that failed with minimal or no shearing. The comparison also shows very clearly the effect of reduced thickness, which was used as an analog to section loss due to corrosion.

Keywords: digital image correlation, strain measurement, buckling, gusset plate connections, steel truss bridges

Contents

1 INTRODUCTION

The work reported here was performed in collaboration with the Federal Highway Administration (FHWA) on the National Cooperative Highway Research Program (NCHRP) Project 12-84 titled "Guidelines for the Load and Resistance Factor Design and Rating of Riveted and Bolted Gusset Plate Connections for Steel Bridges". For this project, large-scale gusset-plate experiments were performed at the FHWA Turner-Fairbank Highway Research Center in the Structures Laboratory (Ocel et al., 2012). Researchers from the National Institute of Standards and Technology (NIST) worked in conjunction with FHWA to perform digital image correlation (DIC) deformation measurements during these experiments, and this report presents the results of the NIST measurements taken during loading to failure of the specimen connections.

The type of connection being tested is a five member structural connection joined by gusset plates on each side of the members (Fig. 1). The load frame setup is designed to permit testing of a variety of gusset plates to failure using the same set of members (i.e., a new specimen is comprised only of two new gusset plates and associated chord splice plates, cover plates, and any retrofits being tested). Failure is defined here as the point when the connection can no longer carry more load (i.e., maximum load). The five members engage reaction walls (shear walls) through four sets of hydraulic actuators. The Vertical member can be in either tension or compression during loading, whereas the East Chord is set in either the compression only or tension only configuration from the time of the connection assembly. The West Chord is grouted and post-tensioned to the West abutment allowing horizontal reaction to be either tension or compression depending upon the particular loading scenario. The symmetric design of the connection results in a South and a North gusset plate that are mirror images of each other.

In this report, the test specimens are referred to by the FHWA selected labeling convention as GP*vvv-wxy-z*, where *vvv* is the bolt type (either "307" for standard A307 or "490" for high-strength A490 7/8-9 UNC bolts), *w* refers to the gap between the corner of the Compression Diagonal and the Chord member ("S" for short,"L" for long), and *x* refers to the edge length or connection length ("S" for short or "L" for long), *y* is the plate thickness where 3 refers to 3/8 in (9.5 mm) and 4 refers to 1/2 inch (12.5 mm), and *z* differentiates repeat tests of the same plate geometries. For example, the first repeat test with A490 bolts, a 3/8 in (9.5 mm) thick plate, a long gap to the chord and short edges is named GP490-LS3-1. Figure 2 shows the plates schematically as viewed from the North side of the connection (detailed dimensions of the plates may be found in Ocel et al. (2012)). The five member edges are also shown in the figure. As an analog to section loss due to corrosion, one plate geometry GP307-SS3 was further machined (from the interior face) to reduce the plate thickness between the members and along the chords in three patterns. These are shown schematically as grey areas with dashed lines in Fig. 2 (again detailed dimensions of the plates may be found in Ocel et al. (2012)). A special case occurs for the test on plate GP307-SS3-4, which added a shingle plate to the North face of the connection. These plates which cover a portion of the gusset plate and connect all five members are intended as a retrofit to reinforce a plate with substantial corrosion. This shingle plate is denoted as GP307-SS3-shingle in the remainder of this report. It should also be noted that although most of the North and South plate connections are

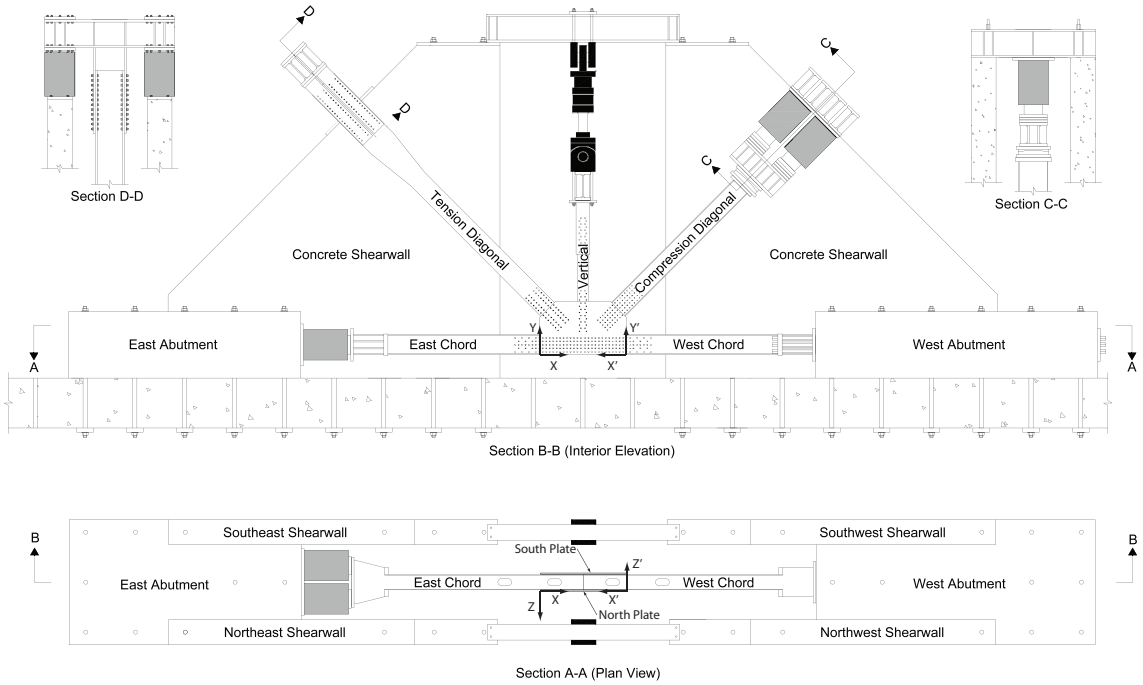

(a)

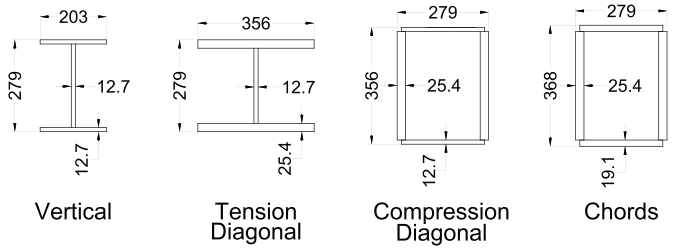

(b)

Figure 1: Structural connection being tested in the load frame: (a) schematic of load frame with East Chord hydraulic cylinders in the compression configuration (hydraulic jacks used to apply loads are shown in grey; the vertical uses a different type of actuator that can apply tension or compression) and (b) shape and dimensions of member cross-sections in mm. Note: section B-B is as viewed from North side of the load frame unlike Ocel et al. (2012).

symmetric, there were a couple exceptions. Specimens GP307-SS3-3 and GP307-SS3-4 had the reduced thicknesses shown in Fig. 2 only for the North gusset plates, and only the GP307-SS3-4 North plate had an added shingle plate to reinforce the plate. For more details on these particular connections see Ocel et al. (2012).

There are four main deformation/strain measurement methods used in the tests to failure: 3D laser point tracking, foil strain gauges, DIC, and a brittle coating method. Most of the methods are used on a dedicated side of one plate to prevent interference from the other methods during testing. Additionally before and after each test, the laser tracking system is used to perform thorough scans of the 3D shape of the gusset plates (including both plate external surfaces, and plate edges). During the test, the laser tracker is used to measure the displacement of specific bolt ends and member reference points on the North face of the connection, while DIC is performed on the outer surface of the North plate, and the brittle coating is used on the outer surface of the South plate. Strain gauges are attached to the members, splice plates, and the inner surfaces of both the North and South gusset plates (i.e., the South face of the North plate and the North face of the South plate).

Full-field shape and strain mapping data is very desirable for the testing of structural connections. Point measurement methods like strain gauges and point displacement sensors may be used in large deformation testing, but sensor placement is selected *a priori* and may not detect local deformations that do not occur at those exact locations. Laser trackers, like the one used in these experiments, is a special case that can be used as a single point tracker or can scan many points to form a point cloud to approximate the full-field behavior. Unfortunately, there is no indexing of these points to exact locations on the plate, therefore the current shape can not be indexed to the original shape making strain field calculation impossible. Photo-elastic techniques can be used in the elastic range, but can not extend very far into the plastic strain range. An example of photo-elastic measurements applied in the elastic range for these same experiments see Iadicola et al. (2012). The brittle coating method does produce some full-field data, but it is not very quantitative. Even if calibrated, the method acts as a threshold for one strain level. DIC, however, is not only a quantitative full-field method to measure 3D shape, but it is also capable of quantitative measurement of surface strains during plastic deformation.

The use of DIC for full-scale *in situ* testing of civil engineering structures as a method of structural health monitoring or inspection has been suggested (Junda et al., 2007; Kitagawa et al., 2007; Kohut et al., 2008; Kujawińska et al., 2010; Kujawińska et al., 2009; Malesa et al., 2010; McCormick and Lord, 2010; Wei and Xiaoyuan, 2009; Yoneyama et al., 2007). Often this is done only for a small portion of the structure. In the case of bridges, the displacement of a span might be measured at specific points (Malesa et al., 2010) along the length, along the entire length (Yoneyama et al., 2007), or used to determine the full-field strain response at a single connection of interest (Junda et al., 2007; Malesa et al., 2010; McCormick and Lord, 2010). Laboratory testing that incorporates DIC typically uses reduced-scale structures for testing and focuses on either a connection (De Roover et al., 2002; Junda et al., 2007; McCormick and Lord, 2010; Sadowski et al., 2010; Smith et al., 2011; Souid et al., 2009; Sozen and Guler, 2011; Wei and Xiaoyuan, 2009) or other small area of interest (Hild et al., 2011; Kujawinska et al., 2011). Yoneyama et al.

(2005) performed laboratory tests on a reduced-scale single girder "bridge" before their field load testing of a single span bridge (Yoneyama et al., 2007). The laboratory and *in situ* testing verified DIC performance with and without an added pattern for correlation by comparing the DIC results to point displacement transducers. The work presented here is the laboratory testing of a single full-scale bridge connection. Unlike some of the previous work that only looked at the strain fields for a small section on the connection, the measurements here use DIC over the entire plate. These experiments are keenly interested in the evolving strain fields over the plate, as well as the out of plane displacements, as the specimen approaches failure. Comparisons can be made to the other measurement methods in common displacement and strain ranges (Iadicola et al., 2012), but are not the focus of this report, nor is the modeling of the results (Mentes et al., 2011).

A stereo (two-camera) digital image correlation system and processing software from Correlated Solutions Inc. is used to perform 3D displacement measurements on the outer surface of the North gusset plate. The system uses a combination of stereo-photogrametry and digital image correlation to measure and track a semi-random surface pattern to determine 3D displacements on a surface and derive strains from those displacements. The method requires a high contrast pattern that moves with the surface of the specimen and clear line of sight to both cameras. A black and white pattern is applied to the plate surface for all the experiments reported here. Plate surface areas obscured directly by the washer, nuts, and bolt ends are not measurable, as well as the areas to either side of the bolt end that are obscured in the images viewed from either the left or right camera.

The coordinate system used for the DIC measurements performed on the outer surface of the North gusset plate shown here has an origin approximately at the lower East corner of the plate (Figs. 1a). The X-axis is nominally aligned with the bottom edge of the North gusset plate, with a Y-axis aligned with the vertical face of the plate. A more detailed definition of the coordinate system is presented in Section 6 below. Note: an alternative coordinate system is used by the other measurement methods that essentially has its origin at the lower West corner of the North gusset plate with the X'-axis to the East and the Y'-axis vertically along the west edge of the plate (Figs. 1a). This alternate system has a positive Z' direction toward the South, which is in the opposite direction from the DIC Z-axis.

Table 1 describes the nomenclature used in this report. The report details the setup (Section 2), specimen preparation (Section 3), calibration (Section 4), procedures (Section 5), and post processing (Section 6) associated with the digital image correlation measurements. A selection of results (Section 7) for the test to structural failure of the connections is shown to illustrate some key results and describe the data that is available for further detailed analysis.

2 SETUP

In the measurements described here, black and white CCD cameras are used in combination with compact 8 mm lenses with locking focus rings and apertures. The cameras are mounted to a continuous aluminum bar to ensure that their spacing and orientation remain unchanged during each experiment (Fig. 3a). The bar is mounted horizontally level on a tripod setting the lens centerline height to the center height of the plate (Fig. 3c). The bar is approximately parallel to the surface of

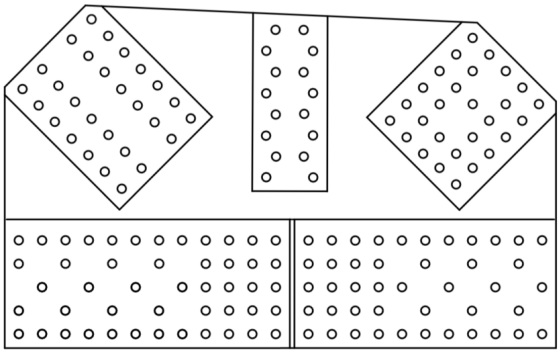

GP307-SS3

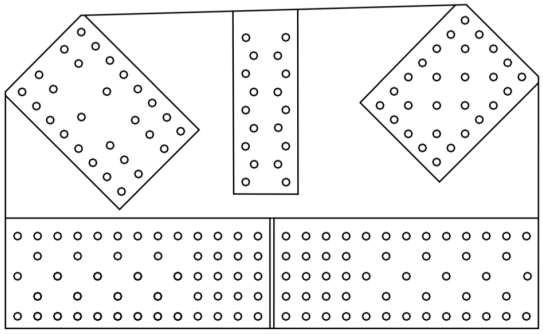

GP307-LS3

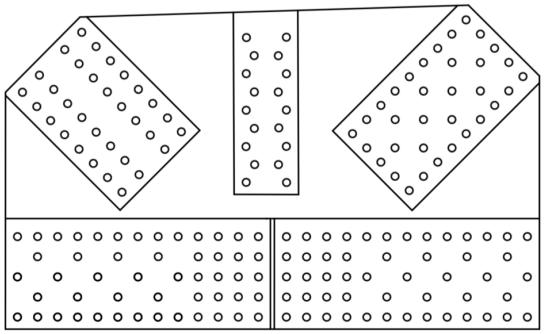

GP307-SL3;
GP307-SL4

Figure 2: Schematic view of the gusset plate specimens as viewed from the North similar to Figs. 1 (Tension Diagonal on the left and Compression Diagonal on the right). The member edge locations are also shown. Four GP307-SS3 samples are described with areas of reduced thickness (shown in grey with dashed edges).

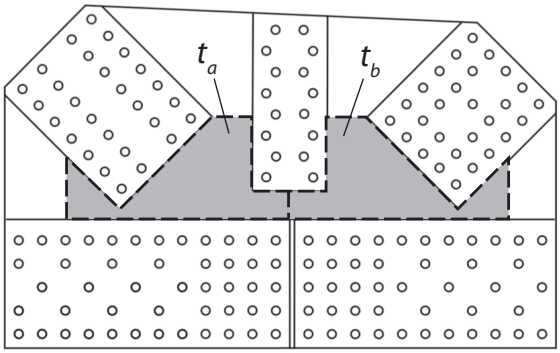

GP307-SS3-1: t_a = 6.48 mm, t_b = 4.75 mm;
GP307-SS3-2: t_a = 4.75 mm, t_b = 6.48 mm

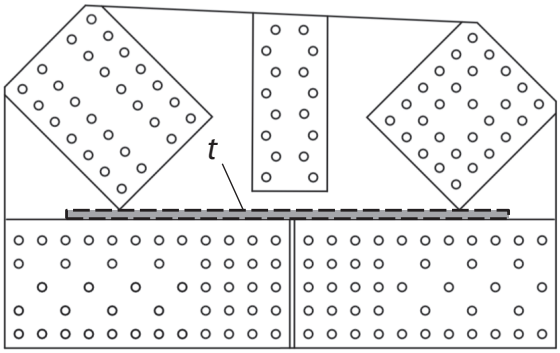

GP307-SS3-3: t = 4.70 mm;
GP307-SS3-4: t = 7.87 mm

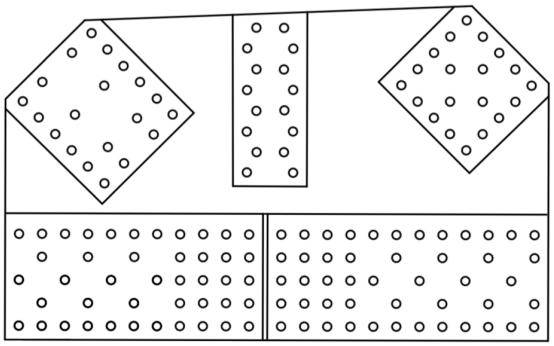

GP490-LS3-1;
GP490-LS3-2
(has added L3”x3”x1/2” angle sections, not shown)

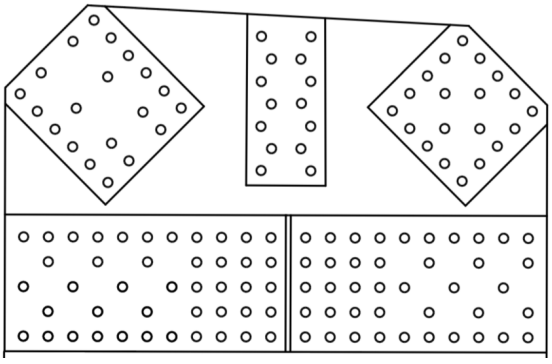

GP490-SS3;
GP490-SS3-1;
GP490-SS3-2;
GP490-SS3-3

Figure 2 (continued)

Table 1: Nomenclature

Symbol	**Symbol in Plot Legends**	**Units**	**Description**
X	X [mm]	mm	3-dimensional orthogonal coordinate
Y	Y [mm]	mm	3-dimensional orthogonal coordinate
Z	Z [mm]	mm	3-dimensional orthogonal coordinate
U	U [mm]	mm	displacement in X-direction
V	V [mm]	mm	displacement in Y-direction
W	W [mm]	mm	displacement in Z-direction
$\varepsilon_{\mathrm{XX}}$	exx [um/m] - Lagrange	μm/m	Lagrangian strain in X-direction
$\varepsilon_{\mathrm{YY}}$	eyy [um/m] - Lagrange	μm/m	Lagrangian strain in Y-direction
$\varepsilon_{\mathrm{XY}}$	exy [um/m] - Lagrange	μm/m	Lagrangian shear strain in XY-plane
ε_1	e1 [um/m] - Lagrange	μm/m	1^{st} principal in-plane Lagrangian strain
ε_2	e2 [um/m] - Lagrange	μm/m	2^{nd} principal in-plane Lagrangian strain
$(\varepsilon_{\mathrm{XY}})_{\mathrm{max}}$	Tresca Strain [um/m] - Lagrange	μm/m	max. in-plane Lagrangian shear strain
θ	n/a	$^{\mathrm{o}}$	included angle between cameras
A	n/a	mm	camera spacing from one another
B	n/a	mm	standoff, camera to plate distance
S	n/a	pixels	digital image correlation subset size
P	n/a	pixels	digital image correlation subset spacing
t	n/a	mm	gusset plate thickness in reduced section
ALF	n/a	N/N	applied load fraction
DIC	n/a	n/a	digital image correlation

the plate (Fig. 3b). The cameras are mounted with an included angle between $\theta = 30^{o}$ and 35^{o} with the bisector of that angle passing through the centerline of the plate width (Fig. 3b). The cameras are spaced at about distance A and set back from the plate by approximately distance B, resulting in the intersection of the optical centerlines of the cameras being located behind the plate surface (Fig. 3b). This was necessary to fill as much of the field of view as possible with the plate. Since the cameras are angled there is no single magnification for either image, but an average magnification value for the plate area of each image can be calculated for the specific camera/lens position for each experiment (see Table 2).

Table 2: Parameters describing the DIC camera orientations. Included angle and spacing between cameras values are based on the system calibration, and are reported here to the same number of decimal places as used in the software.

Plate ID	**Camera Resolution (Mpixel)**	**Angle (^{o})**	**Spacing A (mm)**	**Standoff B (mm)**	**Magnification (pixel/mm)**	**Exposure Time (ms)**
GP307-SS3	2	30.7367	1062.10	1995	1.04	50
GP307-LS3	2	34.2315	1350.50	1850	0.92	50
GP307-SL3	5	32.6439	1151.84	1565	1.41	40–50
GP307-SL4	5	33.3695	1129.11	1570	1.41	25–34
GP307-SS3-1	5	32.8026	1012.12	1420	1.57	35–45
GP307-SS3-2	5	33.0080	1012.04	1390	1.59	25–40
GP307-SS3-3	5	32.6243	1011.84	1395	1.59	30–40
GP307-SS3-4	5	32.7176	1012.09	1385	1.57	25–39
GP307-SS3-4 after reassembly	5	32.7176	1011.81	1385	1.57	25–40
GP490-SS3	2	32.2019	1028.62	1570	1.10	50
GP490-SS3-1	5	32.6302	937.919	1280	1.72	25–38
GP490-LS3-1	5	33.0275	1024.93	1370	1.62	40
GP490-LS3-2	5	33.6706	1025.19	1395	1.60	40–62

Two photographic lights were used to reduce shadowing on the plate surface from the bolt ends and allow the aperture diameters to be reduced (to increase the depth of field). These lights were located behind each of the cameras about 2.7 m from the plate (Fig. 3), and were only on when acquiring images to reduce excessive heating.

3 SPECIMEN PREPARATION

Each North plate specimen was sand blasted after machining to remove the mill-scale and was cleaned of dirt and oil. Subsequently, the surface pattern was applied prior to connection assembly.

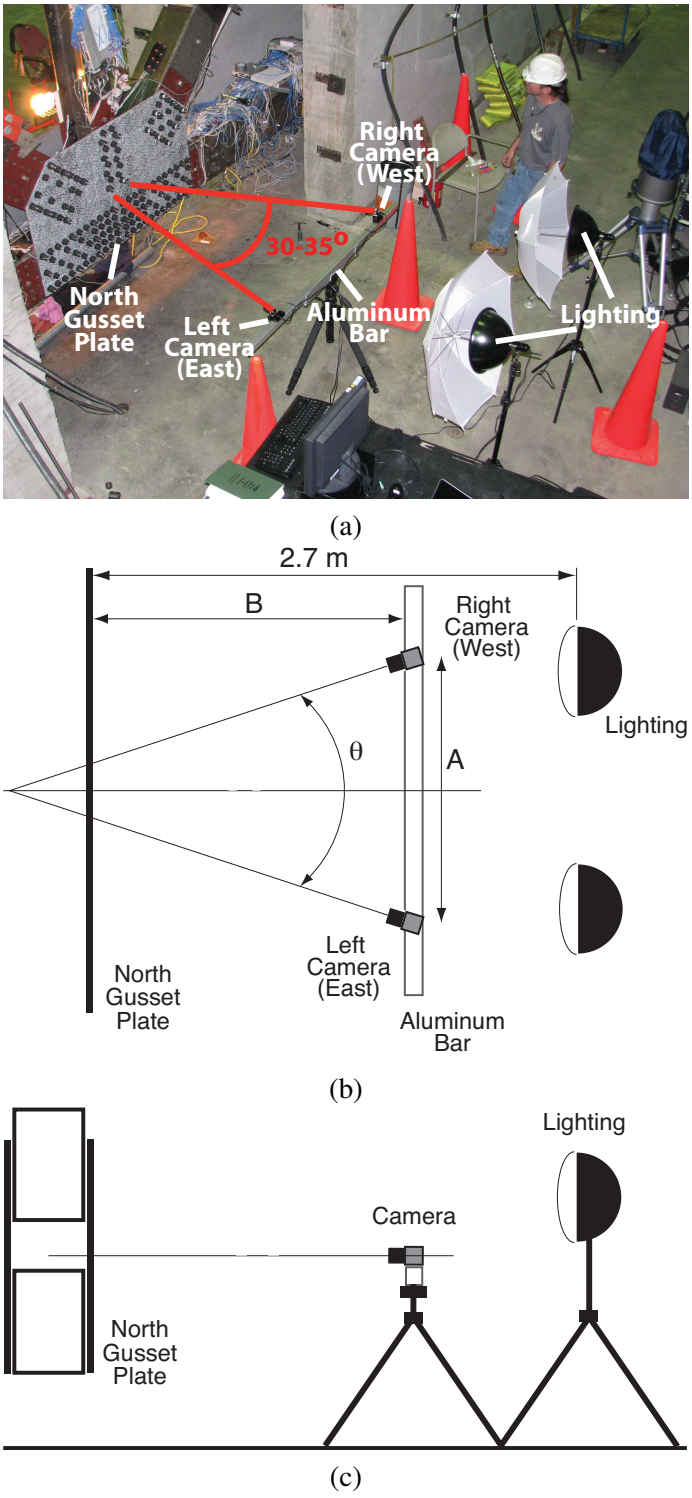

Figure 3: DIC setup (a) annotated photo, (b) schematic plan view, and (c) schematic side view.

Figure 4: Pattern used for digital image correlation measurements as painted on a gusset plate specimen. A 19.0 mm diameter coin is shown for reference.

The North gusset plate was first painted matte white, then patterned with matte black ink stamped on the surface. Minor scratches and other damage to the pattern due to assembly were touched-up using paints of both black and white before testing began. The stamp pattern is 130 mm by 180 mm, which results in a slight chance of aliasing during correlation, due to the pattern repetition. This is rarely an issue because of the natural variation in the quality of the stamped pattern. This aliasing did occasionally occur during post processing, but was corrected through a combination of adjusted correlation thresholds or in extreme cases trimming of problem areas from the correlation analysis. The stamp pattern is designed to be semi-random with a nearly equal amount of area that is black or white (Fig. 4). The size of the pattern is such that the black and white features are each about 5 mm wide. This results in two to three edges being visible in any 15 mm length on the plates.

4 CALIBRATION

A two-step calibration procedure is used here: first for the cameras/lenses, and then second for the orientation of the cameras to one another. A reference dot pattern target is used to calibrate each combination of camera and lens. Since the target does not fill the field of view, multiple images are needed to interrogate the entire field of view and determine the necessary lens corrections for each camera (see number of images left and right in Table 3). A known length within an area of correlation is required to determine the spacing and orientation of the cameras to one another. A bar with two target panels attached at a known spacing between features (see Fig. 5b and Table 3) is used where each target has a pattern similar to the pattern painted on the plate. Image pairs of this bar at three tilts to the horizontal are used to calibrate and verify the camera spacing and orientation. The calibration is done with one of the image pairs of the bar in the horizontal position

(Fig. 5a), and then the images of the bar in other positions are checked using that calibration to verify the measured panel spacing is correct to within an acceptable error (see length errors shown in Table 3). The resulting camera positions based on the calibration are shown in Table 2.

Table 3: Number of images used to perform the DIC system calibration. Length of reference targets used for system calibration, and error in measured length with targets in angled positions.

Plate ID	Images Left	Images Right	Target Spacing (mm)	Length Error Tilt 1 (%)	Length Error Tilt 2 (%)
GP307-SS3	64	40	1262.130	<0.01	-0.02
GP307-LS3	45	45	1236.980	-0.01	-0.04
GP307-SL3	50	74	1237.107	0.06	-0.06
GP307-SL4	208	212	1160.145	<0.01	0.01
GP307-SS3-1	162	162	1160.209	-0.07	0.02
GP307-SS3-2	166	149	1160.145	0.03	0.02
GP307-SS3-3	171	159	1160.145	<0.01	0.01
GP307-SS3-4	195	203	1160.145	-0.04	0.02
GP307-SS3-4 after reassembly	188	188	1160.145	-0.01	-0.02
GP490-SS3	35	42	1237.107	0.02	<0.01
GP490-SS3-1	100	95	1083.945	0.06	<0.01
GP490-LS3-1	52	49	1236.980	0.03	0.06
GP490-LS3-2	68	67	1236.92	-0.02	-0.01

5 PROCEDURE AND ACQUISITION

Before the start of each test to failure, but after calibration of the DIC system, approximately three image pairs are acquired (while the connection is in an unloaded state). One of the pairs will be used as the reference state while the other two will be used to determine systematic uncertainties during post processing. For each test to failure, an equilibrium load ratio combination on the five members is selected (Table 4), and loads are applied as incremental steps of this load combination on four members (with the West Chord a fixed reaction member) through a feed back control loop. These values are targets, but during the testing actual values are measured. The applied load fraction (ALF) values given in this report are based on the current load for the dominant member divided by a reference load value (4448 kN or 1000 kips). During the load steps in the elastic range and for initial yield, the loading is held for extended periods (approximately 5 minutes) for other measurements to be made using the laser tracker system. At the start of these static holds, a set of DIC image pairs was acquired, and if any imaging problems occurred, then a second set was

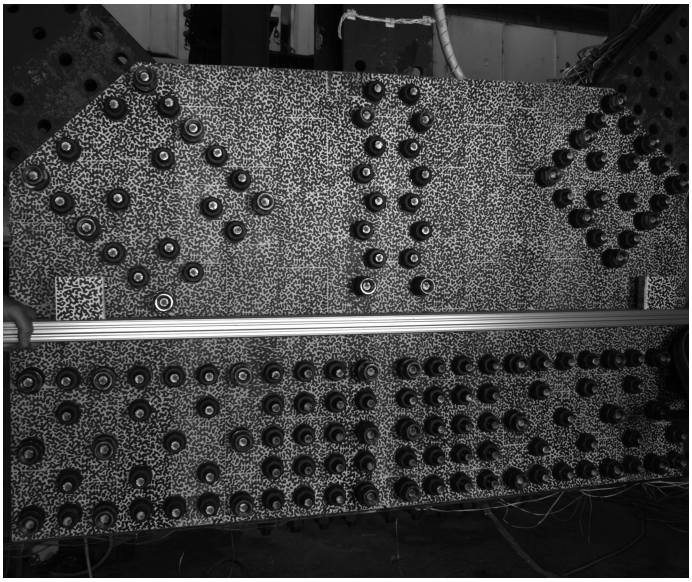

(a)

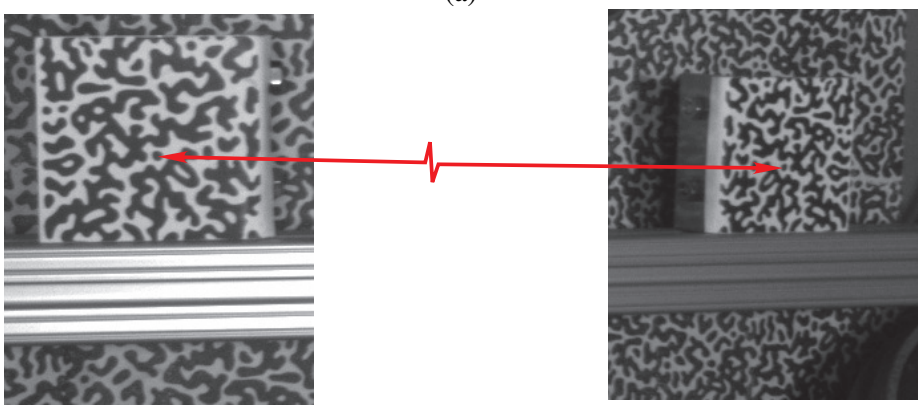

(b)

Figure 5: Left camera image of a horizontally positioned DIC calibration reference bar and targets (a), with cropped images showing targets (b) with two features at a known distance used for system calibration.

taken after the laser tracking measurements were complete. As the specimen approached failure these extended hold times were no longer needed (laser tracking measurements were suspended) and DIC images were acquired at regular time intervals. The frequency of image acquisition was increased as the specimen loading approached the predicted failure load. The maximum image acquisition rate used in the experiments was 0.1 Hz. Each image is acquired with an exposure time between 25 ms and 62 ms (Table 2), and typically three image pairs were taken at each static hold point in deformation. Along with the image file times, four analog signals (Tension Diagonal master hydraulic cylinder load, Tension Diagonal position, Compression Diagonal master hydraulic cylinder load, and Compression Diagonal position) were sampled simultaneous to each image pair to help synchronize the image acquisition with the other data systems.

Table 4: Approximate applied load ratio combinations for each gusset plate tested. Values have no units. To obtain the target applied load combination for a given plate, multiply the tabulated ratio by the current applied load fraction (ALF) times the reference load of 4448 kN (or 1000 kilo-pounds, kips). Tensile values are positive, and compressive values are negative.

Plate ID	East Chord	Tension Diagonal	Vertical	Compression Diagonal	West Chord (reaction)
GP307-SS3	-0.707	0.707	0.207	-1.000*	0.500
GP307-LS3	0.261	0.348	0.246	-0.697	1.000*
GP307-SL3	-0.707	1.000	0.000	-1.000*	0.707
GP307-SL4	-0.707	1.000	0.000	-1.000*	0.707
GP307-SS3-1	-0.707	0.707	0.207	-1.000*	0.500
GP307-SS3-2	-0.707	1.000*	-0.207	-0.707	0.500
GP307-SS3-3	-0.707	1.000*	-0.207	-0.707	0.500
GP307-SS3-4	-0.707	1.000*	-0.207	-0.707	0.500
GP490-SS3	-0.707	1.000	0.000	-1.000*	0.707
GP490-SS3-1	-0.600	1.000*	-0.282	-0.600	0.531
GP490-LS3-1	-0.600	1.000*	-0.282	-0.600	0.531
GP490-LS3-2	-0.600	0.600	0.282	-1.000*	0.531

* dominant member used for calculation of ALF values in this report

6 POST PROCESSING

The image pairs for each test to failure are analyzed using stereo digital image correlation techniques to measure the 3D displacement of the gusset plate surface. For any selected subset of pixels in one image of each pair, a correlation can be performed to the pixels in the other image of each pair using the measured system calibration. If both of these subsets view the same grey scale pattern the correlation errors will be minimized, and the 3D location of the subset will be

known based on the orientation of the system calibration, and this location is attributed to a point located at the center of the subset. Parameters are set in the algorithm to reject data points at subsets that exceed user-defined tolerances for the correlation errors. A series of subset correlations can be performed to cover the area of interest in the images (i.e., the gusset plate), thus reproducing the current shape of the plate indexed to the pattern being interrogated. These same subsets can be correlated to subsequent image pairs to determine the new 3D positions of each subset. The changes in 3D positions of each subset define the measured displacements of that subset. A coordinate transformation may be defined to rotate these data from the camera system coordinates to an arbitrary coordinate system (e.g., the plate surface system as shown in Fig. 1a).

An assessment of the errors associated with the system setup, pattern, and analysis parameters is performed using a series of image pairs taken with the specimen resting in the unloaded state. The first image pair acts as the reference shape and the subsequent image pairs as data with known displacements equal to zero. The measured displacements not equal to zero represent the error in the measured variables. For each plate before the test to failure, the system setup and pattern are adjusted to reduce the errors associated with the correlation. The analysis parameters, including the subset size and spacing, are optimized during the post processing of the test as described below.

The DIC analysis requires the user to define the region of analysis in one image of the pair, as well as the subset size for correlation and subset spacing. The subset size (S) defines the area over which each position and displacement measurement is averaged. The subset spacing (P) determines the amount of overlap between the subsets, where a spacing size equal to the subset size results in each subset being an independent measurement (i.e., no overlap). Overlapping subsets results in some smoothing of the data, but this is only an issue when there are sharp gradients in shape or displacement. Since the results here are for a contiguous specimen, this is not a concern. The smallest possible subset spacing is one, but this requires substantially more processing for limited added data for a specimen with a smoothly varying shape. A typical subset size is shown as a red square in Fig. 6b. For all of the results shown here, the region of analysis was selected in the left image to be the edge of the plate or plates (Fig. 6a), which included the bolt heads that obscure the pattern and have no pattern and thus do not correlate. This results in many areas that have no pattern to correlate (Fig. 7a), but was determined to be less time consuming than manually removing the correlation region around each bolt end. The required subset size also limits how close to the plate edges or other features the data can be measured (Fig. 7a and b). Consequently, there is useful DIC data only in the field areas of the plate and between some of the bolts where both cameras could view enough of the surface pattern. Initially it also resulted in some areas of poor correlation that included the edges of the washer, nuts, and bolt ends (in Fig. 7a subset shown below the bolt end). Tolerances on the correlation were adjusted for each test to remove the correlation areas that included the bolt ends and washers. In extreme cases, some of the region of interest was trimmed to remove the problem areas. When aliasing occurred due to pattern repetition, it was typically located at points that were visible only in one image such as the area just to the left or right of a bolt end (Fig. 7a). These were easily corrected by trimming this area from the region of analysis.

The DIC measured positions and displacements are rotated to a user defined orthogonal coordi-

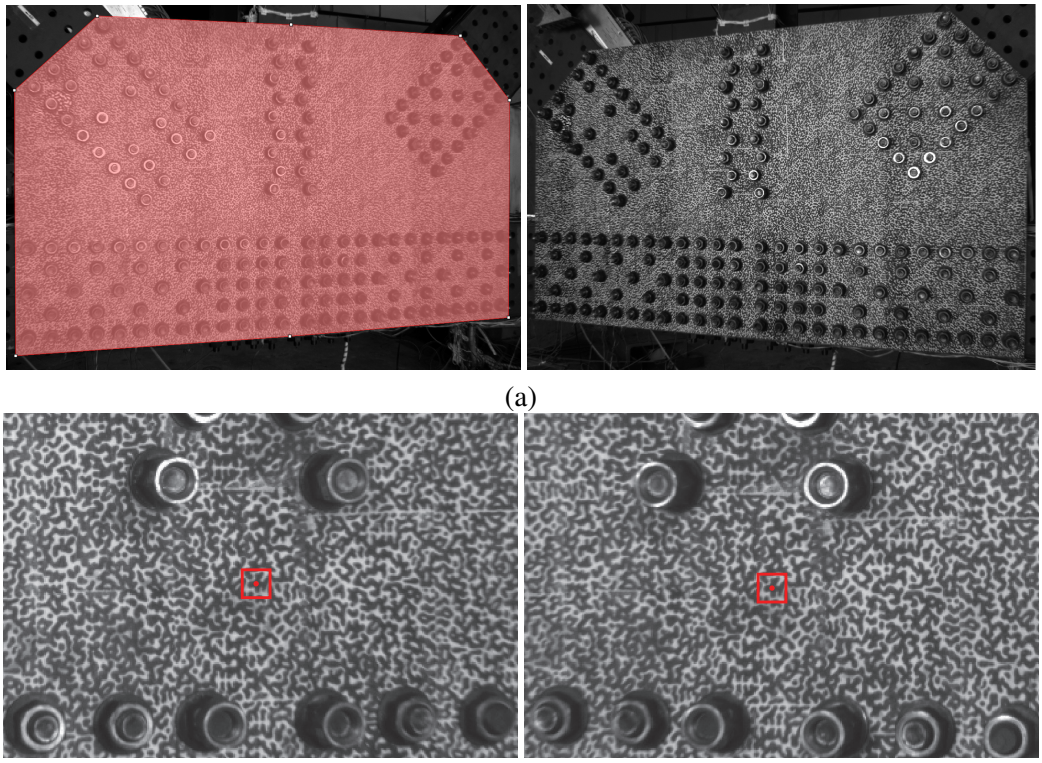

(a)

(b)

Figure 6: Images of GP307-LS3 (a) DIC region of analysis (semitransparent red area) selected in left image of the image pair shown. (b) Close up images with approximate DIC subset (red square with red center spot) in left and right images.

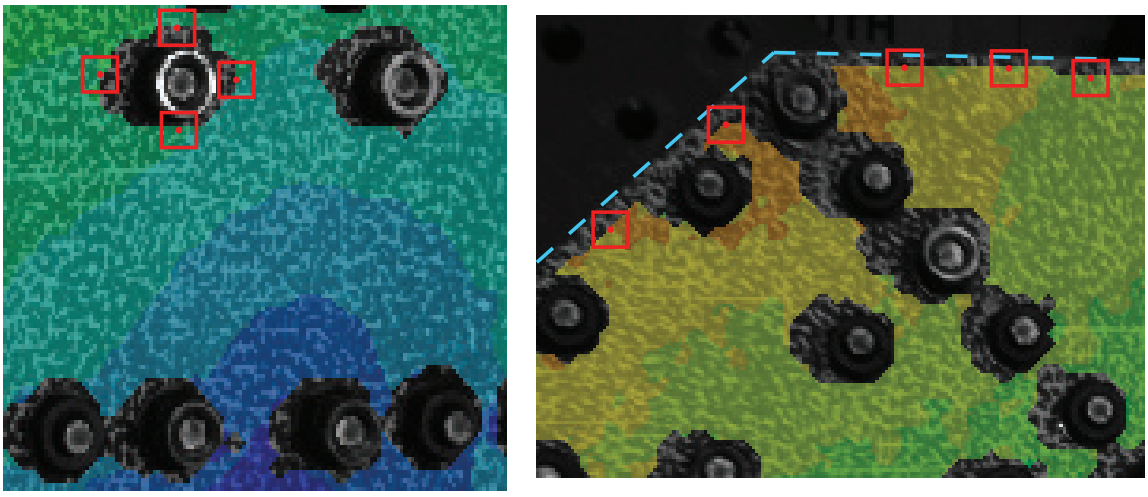

(a) (b)

Figure 7: DIC subsets (red square with red center spot) near edges of the correlation region (a) around bolt ends and (b) near plate edges (dashed lines).

nate system, which is based on reference marks offset from the bottom edge of the plate that were made during painting of the plate. The X-axis origin is the lower East corner of the North plate (Fig. 1a). The Y-axis projection on to the XZ-plane is normal to the X-axis and approximately follows the East vertical edge of the plate. The Z origin is based on three points in the field of the plate: one below the Tension Diagonal, one below the Compression Diagonal, and one between the top bolts of the Vertical. Figure 8 shows the approximate location of these three points for one plate as viewed in the left image. The initial Z shape shows the zero-contour intersects these three points. A color map with a transition from brown (negative values) to blue (positive values) is typically used in this report for plots of Z-shape, since it is the deviation from perfectly flat that is of primary interest. The measured displacements in the X, Y, and Z directions are defined as U, V, and W respectively.

Strains are derived from the measured displacement fields. The Lagrangian formulation of strain was used for all the measurements, since it is typically used for finite element modeling. The axial strains in the X-direction (ε_{XX}), Y-direction (ε_{YY}), and shear strain in the XY-plane (ε_{XY}) are calculated from the measured displacements,

$$\varepsilon_{XX} = \frac{\partial U}{\partial X} + \frac{1}{2}\left[\left(\frac{\partial U}{\partial X}\right)^2 + \left(\frac{\partial V}{\partial X}\right)^2 + \left(\frac{\partial W}{\partial X}\right)^2\right] \tag{1}$$

$$\varepsilon_{YY} = \frac{\partial V}{\partial Y} + \frac{1}{2}\left[\left(\frac{\partial U}{\partial Y}\right)^2 + \left(\frac{\partial V}{\partial Y}\right)^2 + \left(\frac{\partial W}{\partial Y}\right)^2\right] \tag{2}$$

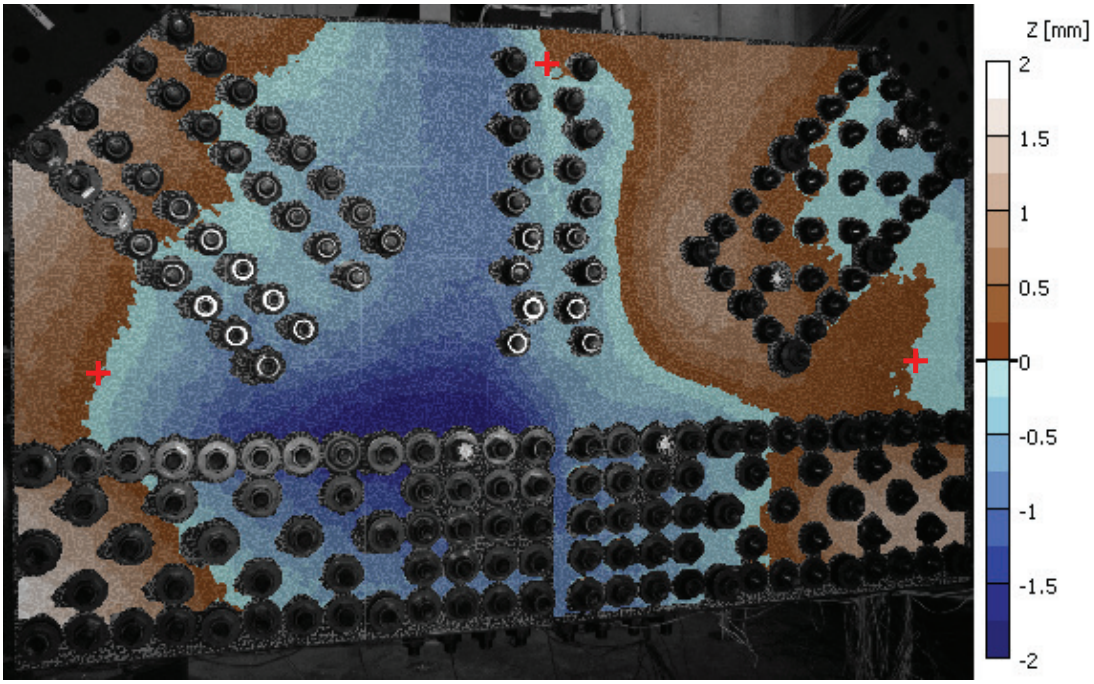

Figure 8: Out-of-plane shape (Z positive outward from the plate) after coordinate rotation to specimen GP307-SL3. Three points shown as red crosses locate the Z = 0 mm plane.

$$\varepsilon_{XY} = \frac{1}{2}\left(\frac{\partial U}{\partial Y}\frac{\partial V}{\partial X}\right) + \frac{1}{2}\left(\frac{\partial U}{\partial X}\frac{\partial U}{\partial Y}\right)^2 + \left(\frac{\partial V}{\partial X}\frac{\partial V}{\partial Y}\right)^2 + \left(\frac{\partial W}{\partial X}\frac{\partial W}{\partial Y}\right)^2. \quad (3)$$

Note: the higher order (large strain) terms are used in the calculation. The calculation is performed for the each analysis point using the nearest neighboring points. The calculations are performed individually on a triangle formed by the point of interest and two of neighboring points, and then these values are averaged for all of the neighboring points. This results in strains that are calculated near the edge of the analysis region using only one to three of these triangles, where as points in the center of the analysis region use four triangles. The resulting strains are smoothed with other data points within a two subset radius of the point of interest using a Gaussian weighted (10 % at the highest radius) filter. This results in slightly larger strain uncertainty near any edge of the region of analysis (i.e., plate edge or near a bolt end) since less triangles are averaged. In the figures presented here, the nomenclature for the strains (and the associated units) is slightly revised to not require Greek lettering (Table 1). The maximum in-plane shear strains $(\varepsilon_{XY})_{\max}$ (or "Tresca Strain" as described in the software) are also calculated. Note that the Tresca strains are based on the tensor definition,

$$(\varepsilon_{XY})_{\max} = \sqrt{\left(\frac{\varepsilon_{XX} - \varepsilon_{YY}}{2}\right)^2 + (\varepsilon_{XY})^2}, \quad (4)$$

that is $(\varepsilon_{XY})_{\max} = \frac{1}{2}(\gamma_{XY})_{\max}$ (i.e., the Tresca strains are the radius of Mohr's circle of in-plane strain as opposed to the typical definition of $(\gamma_{XY})_{\max}$ which is the diameter of Mohr's circle). All of the strains are determined for the outer surface of the plate. The variation of strain through the thickness of the plate, due to bending, is not considered or discussed here.

Assessments of the noise level in the calculated maximum shear strains for two images taken in the unloaded reference state were used to determine an optimal square interrogation subset size (S) and a subset spacing (P) for each experiment, which balanced the reduction of the noise error while keeping the subset as small as possible. These settings and the resulting uncertainties are shown in Table 5. The uncertainties for the Tresca strain, W, ε_{XX} and ε_{YY} are based on plus/minus one standard deviation from the expected zero value for all of the plate data. These are somewhat conservative values since they include edges of the correlation areas (i.e., plate edges and near bolt ends). If only the areas between the members that do not have an edge of the correlation area are considered the uncertainties reduce to about half the values shown in Table 5. Kujawinska et al. (2011) and Smith et al. (2011) both report uncertainties for W of ± 0.030 mm which is of a similar value as those calculated here. Unfortunately they do not report uncertainties for any other of the variables of interest here.

7 RESULTS

A total of 12 tests to failure are presented in this report. For each test, between 100 and 800 image pairs were acquired and processed. In this section, a small, but representative, portion of these results are presented. This section is broken down into three main subsections. The Example Case Section 7.1 includes a sample of the results for one test to failure (GP307-SL3) at just two

Table 5: Parameters describing the DIC analysis and resulting uncertainties.

	S		P		Uncertainty			
Plate ID	**actual (pixels)**	**average (mm)**	**actual (pixels)**	**average (mm)**	**Tresca (μm/m)**	**W (mm)**	ε_{XX} **(μm/m)**	ε_{YY} **(μm/m)**
GP307-SS3	19	18.2	7	6.7	246	0.040	337	346
GP307-LS3	19	20.7	7	7.6	85	0.030	105	134
GP307-SL3	23	16.3	7	5	142	0.023	181	177
GP307-SL4	23	16.3	7	5	195	0.021	147	380
GP307-SS3-1	23	14.6	7	4.5	251	0.019	151	490
GP307-SS3-2	23	14.5	7	4.4	144	0.028	142	243
GP307-SS3-3	23	14.5	7	4.4	124	0.016	146	168
GP307-SS3-4 gusset	23	14.7	7	4.5	226	0.018	269	318
GP307-SS3-4 shingle	23	14.7	7	4.5	126	0.015	161	167
GP307-SS3-4 shingle after reassembly	23	14.7	7	4.5	169	0.024	203	265
GP490-SS3	19	17.3	6	5.4	180	0.031	167	251
GP490-SS3-1	23	13.4	7	4.1	140	0.018	160	229
GP490-LS3-1	23	14.2	7	4.3	254	0.029	256	430
GP490-LS3-2	23	14.4	7	4.4	188	0.025	325	325

load steps and includes the different positions, displacements, and strains measured for each image pair. The Example section is intended to inform the reader of the type of data that is available for further analysis. The Key Points Section 7.2 includes the results of a few notable variables for all twelve tests to failure at four key points during the loading of each plate. This is intended to show how the deformations evolved during the tests to failure. The Comparison Section 7.3 presents the failure results for all twelve tests together for one strain variable on a common scale to permit cross comparison of the tests.

All of the results are presented as contour plots with varying color maps and scales that overlay the left image at the current stage of loading. This means the chord members are in the lower part of the plot, and the Vertical and Diagonal members are in the upper part of the plots. The left side of the image is to the East and the right is toward the West (see Fig. 1). The Tension Diagonal member is in the upper left of the image and the Compression Diagonal member is on the upper right. When applicable, the current load level is described as the applied load fraction (ALF), which is the ratio of the current load on the dominant member (for a given load ratio combination on all five members, see Table 4) divided by a 4448 kN (1000 kip) reference load on that same member. Recall that for each test to failure a particular equilibrium load combination (Table 4) on the five members (with the reference load on a specific member) is selected prior to the start of the test. During loading, the ratio of the loads on the members is approximately matched at every step to the selected load combination, thus the ALF along with knowledge of the selected load combination generally describes the current load condition.

7.1 Example Case

A sample of the results for the test of GP307-SL3 to failure is presented in Fig. 9–12. The positions X, Y, and Z are in reference to the selected coordinate system described in the Section 6 above (approximately shown in Fig. 1). Figure 9 plots the initial (ALF = 0) plate shape in the X-Y-Z system where each legend uses the same color map, but different value ranges. The initial out-of-plane plate shape (Z positive toward the camera system, see Fig. 1a), shown in Fig. 9c, was qualitatively verified using a straight edge to check the locations of the high and low points. For some of the tests, this shape was spot checked more quantitatively through comparison to the measurements of the laser tracker system. In some tests, patterned covers were attached to selected bolt ends to see if the motion of the bolt ends could be tracked (see four red areas on the bolt ends in Fig. 9c, two on the Chord members and two on the Compression Diagonal). Although the measurements of these covers are shown in the plots the details of the measurements are not discussed here.

Figure 10 plots the displacements (U, V, and W) from the initial shape (Fig. 9) at the point of maximum load (ALF = 0.95). The X-direction displacement (U) shows that the entire plate has shifted to the East (left), with the upper half of the plate shifting by about 8 mm more than the lower half. This is consistent with the Tension and Compression Diagonals having a force resultant in the negative X-direction, while the Chord members are loaded from the East (left) in the positive X-direction. The Y-direction displacement (V, Fig. 10b) shows that the East (left) half of the plate has shifted up pulled by the Tension Diagonal, while the West (right) half of the plate

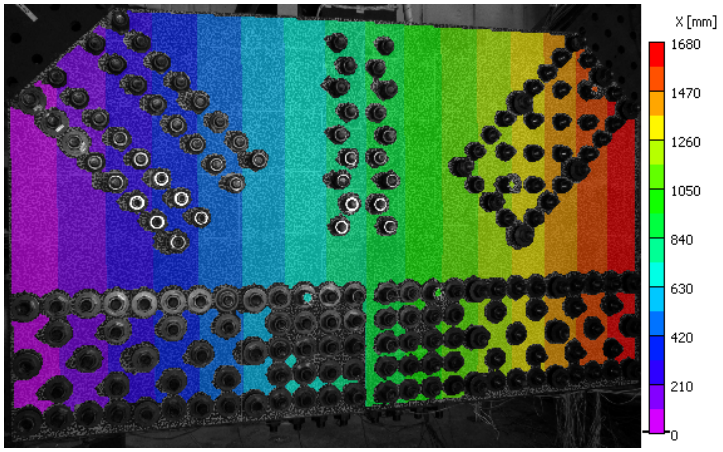

(a)

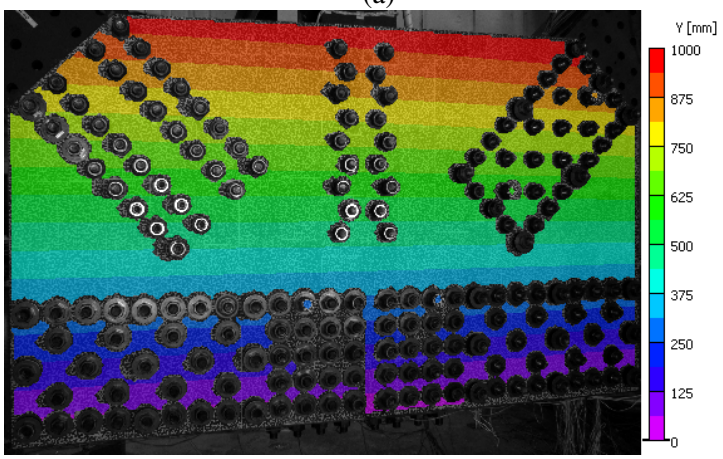

(b)

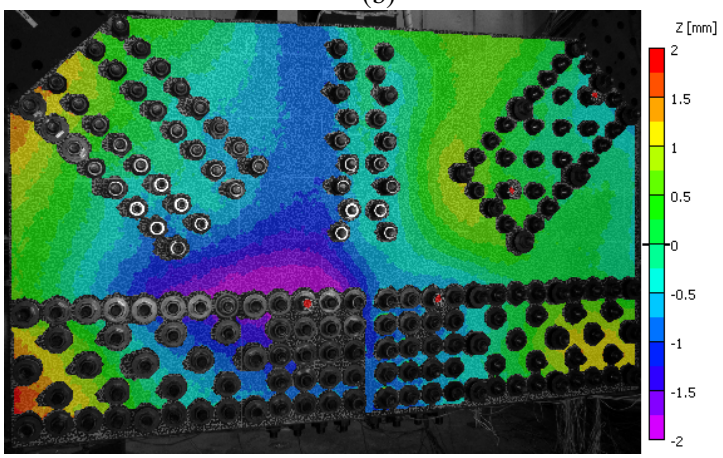

(c)

Figure 9: Initial positions (a) X, (b) Y, and (c) Z at zero load (ALF = 0) for specimen GP307-SL3.

has shifted down pushed by the Compression Diagonal. The out of plane displacement (W) shows that on average the plate shifted away from the camera (toward the South), but that the plate at the Compression Diagonal swayed out to the North, with buckling along the free edges between both the Compression Diagonal and the Vertical, or Compression Diagonal and the West Chord.

The Lagrangian strains are calculated from the displacement fields, as described above. The results are the axial strains ε_{XX} and ε_{YY}, in the X and Y-directions respectively, as well as the in-plane shear strains ε_{XY}, for each measurement point referenced to the selected coordinate system. These results are shown as contour plots of strain, Fig. 11. The most prominent strains are the ε_{XY} (Fig. 11c), which shows shear strain bands that extend between the bolt lines of the various members. With knowledge of the in-plane components the principal in-plane strains can be calculated at each analysis point. Note that the orientation of the direction of the principal strains in the XY-plane can vary with location on the plate. Fig. 12a and b plot the first and second principal in-plane strains, respectively, with the second plotted with reverse color map (red being the minimum strain value). If $\varepsilon_1 = -\varepsilon_2$ then that point has an orientation that is in a state of pure shear. Deviations from this equality result for areas that deviate from pure shear.

The combined strain measure described in Section 6, and shown here, is the Tresca strain ($(\varepsilon_{XY})_{\max}$), which combines all of the in-plane strain components into one strain measure. Tresca strains are plotted in Fig. 12c, where the color map now includes a grey portion at the lowest strain level. The upper limit of the grey bar is set at the static yield strain (1040 μm/m) for this strain measure based on material property tests for this particular plate. This allows the reader to delineate the area that is elastically loaded (grey) from the area that is plastically deforming (spectrum of colors). A similar color map will be used in the next two sections for cases when the maximum plastic strains are quite large (i.e., five or more times yield). This Tresca yield strain value for each plate is calculated from the uniaxial data from coupon tests of the same plate material through,

$$[(\varepsilon_{\mathrm{XY}})_{\max}]_{\mathrm{Y}} = \frac{1}{2}\frac{1+\nu}{E}\sigma_{\mathrm{Y}}, \tag{5}$$

where ν is the Poisson's ratio (value of 0.3 assumed), E is the elastic modulus (value of 29 000 ksi = 200 GPa assumed), and σ_Y is the static yield stress as measured from the coupon test data for each plate.

7.2 Key Points

In this section, the evolution of each specimen from the initial state through four steps to failure are described for each specimen. Based on a general assessment of the data, three variables were selected for more detailed presentation here. The first is the initial shape of the plate in terms of Z, which could be a factor when considering the effect initial imperfections can have on imperfection sensitive testing. The second is the out-of-plane displacement (W) as it evolves with loading, which may be used to determine if and when buckling occurs. The third is the Tresca strain (maximum in-plane shear strain), which is useful in determining localized strain mechanisms (such as shear banding). For each plate tested, the results for out-of-plane displacement and Tresca strain are presented at four representative load levels (in terms of ALF, see Table 4), in addition to the initial shape at the zero load level (ALF = 0). A brief discussion of the results for each plate follows.

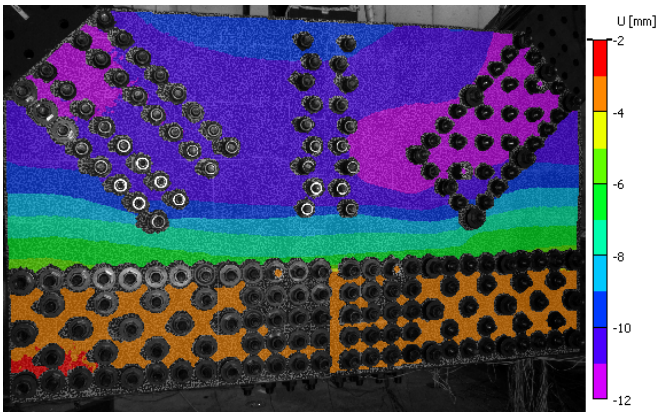

(a)

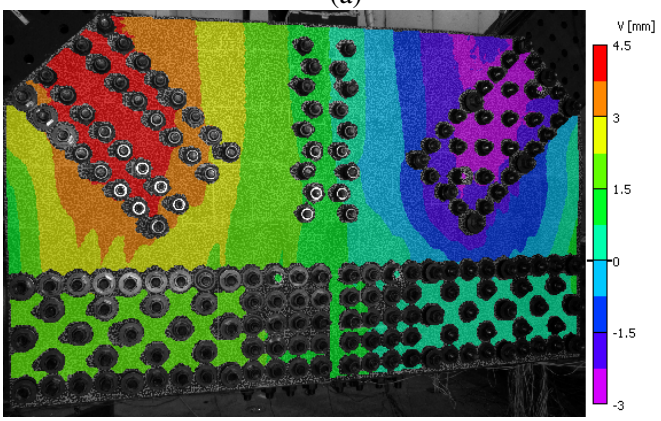

(b)

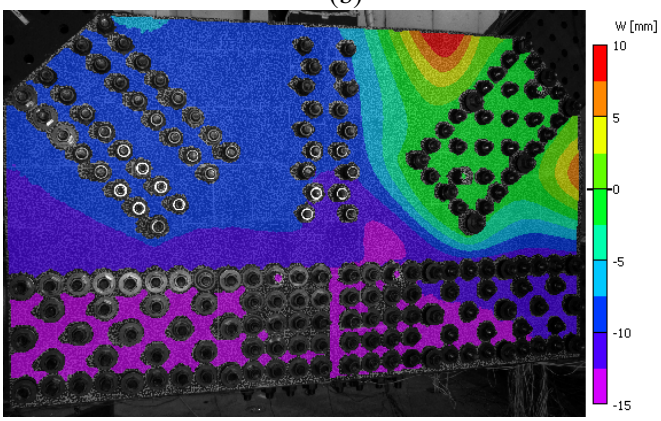

(c)

Figure 10: Displacements (a) U, (b) V, and (c) W measured for GP307-SL3 at failure (maximum load, ALF = 0.95).

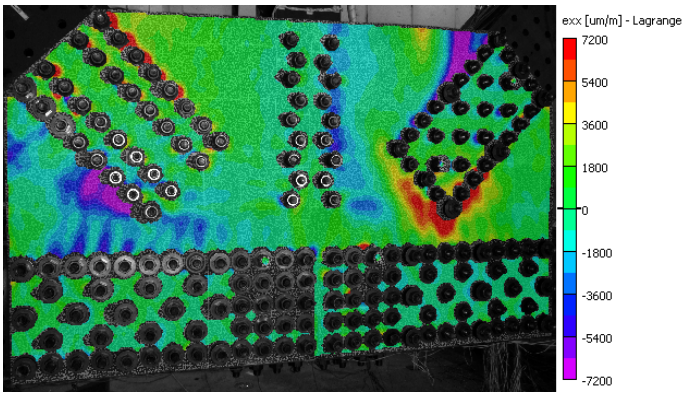

(a)

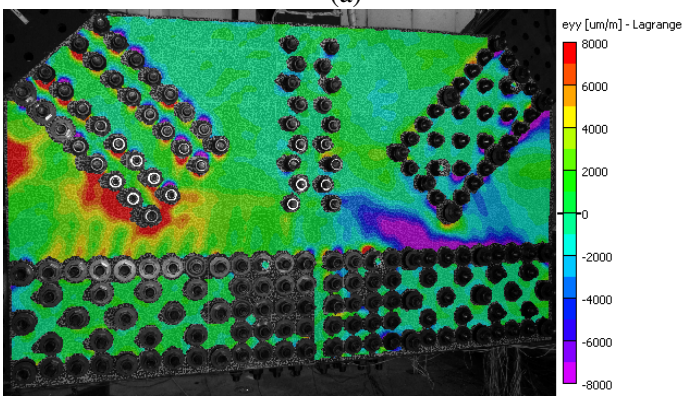

(b)

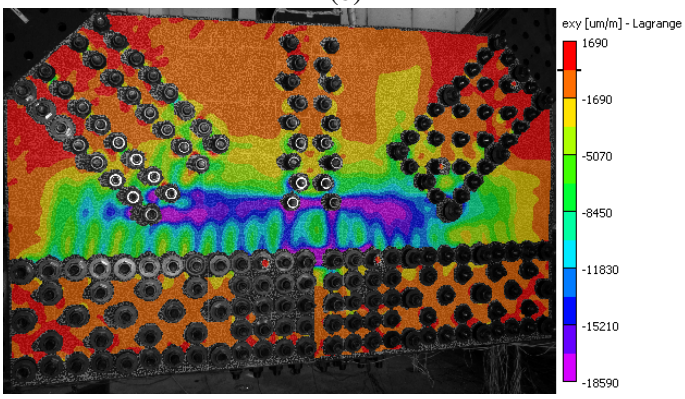

(c)

Figure 11: Strains (a) ε_{XX}, (b) ε_{YY}, and (c) ε_{XY} for GP307-SL3 measured at failure (maximum load, ALF = 0.95).

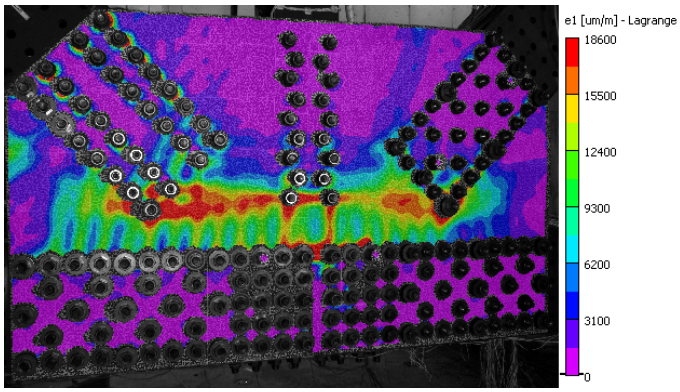

(a)

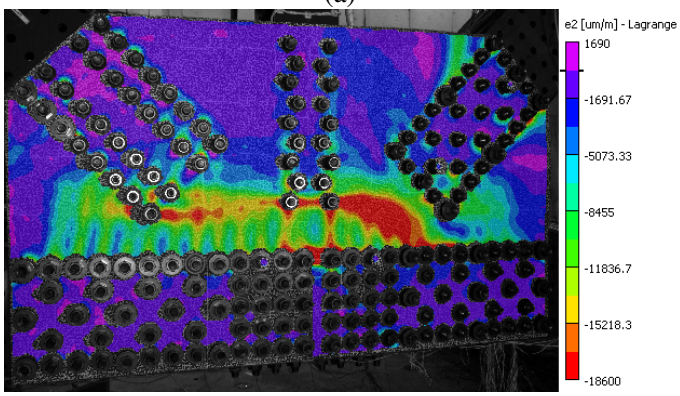

(b)

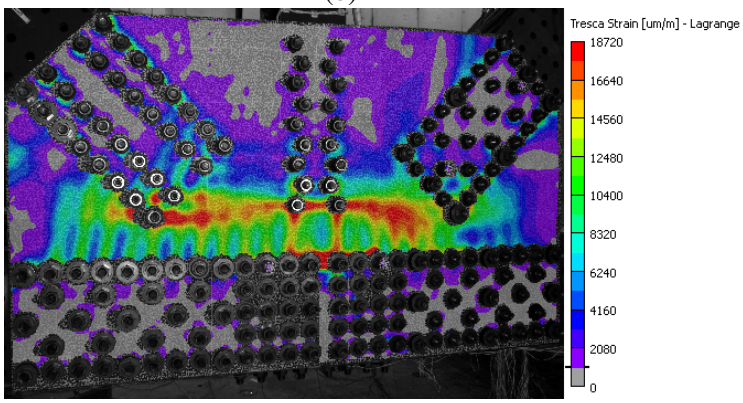

(c)

Figure 12: First principal strain (a) ε_1, second principal strain (b) ε_2, and (c) Tresca strain measured for GP307-SL3 at failure (maximum load, ALF = 0.95).

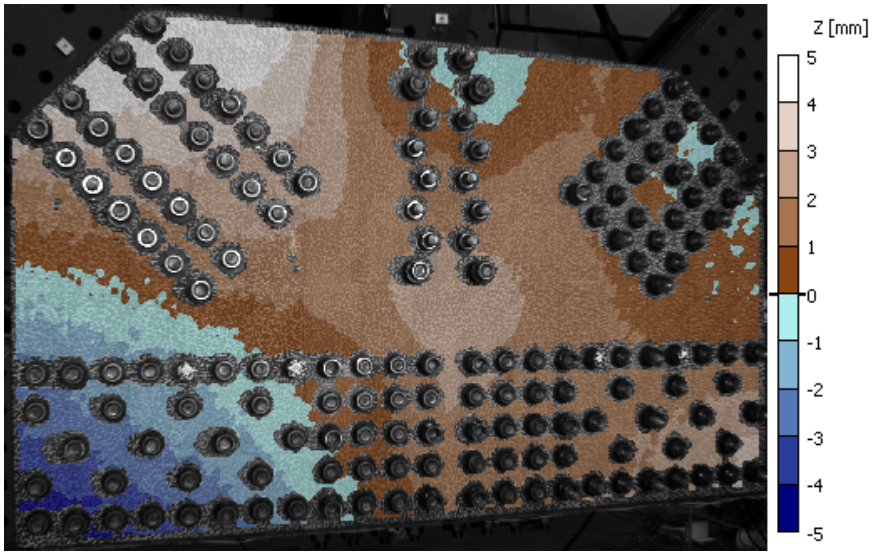

Figure 13: Out-of-plane shape of specimen GP307-SS3 at zero load (ALF = 0).

7.2.1 GP307-SS3

Figure 13 shows the initial shape of GP307-SS3 at the start of the failure test under no load. The location of Z = 0 mm was set using three points as described above. After the rotation, the plate is slightly convex about the end of the Vertical member, and has an overall twist with the Tension Diagonal toward the positive Z and the East Chord in the negative Z-direction. Figure 14 shows the evolution of W (Z-direction displacement) from the initial shape in Fig. 13. The ALF values are in reference to the Compression Diagonal load (see Table 4). During the test, the entire plate shifted toward the negative Z-direction from an early stage, with final buckling of the Compression diagonal in that direction (Fig. 14d). Figure 15 plots the maximum in-plane shear strains at the same four ALF levels shown in Fig. 14. The yield strain in terms of Tresca strain is approximately 820 μm/m, based on standard material testing of the same material. Figures 15a–c have strain ranges predominately in the elastic range, and use a pseudorandom color map. Figure 15d has a strain range predominately in the plastic strain range (spectrum color map) with grey being used for areas of the plate that have not yet reached the yield strain. The results show that the Tresca strains were concentrated between the ends of the Compression and Tension Diagonals from the early stages of loading, with the largest strains occurring at the end of the Compression Diagonal and along the Chord bolt lines. The strain field is more uniform in the early stages of loading, but the later two stages show more strain localizations, which extend between the various bolt lines by the point of failure (ALF = 0.71).

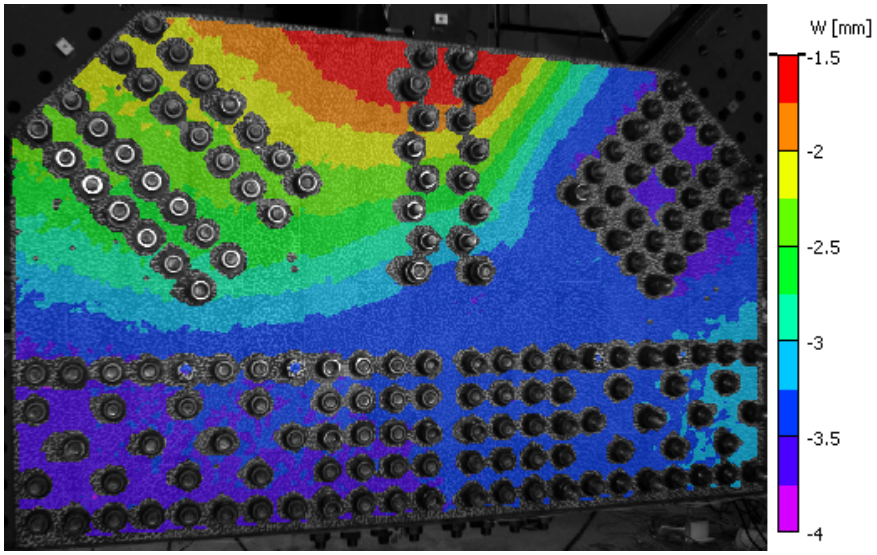

(a)

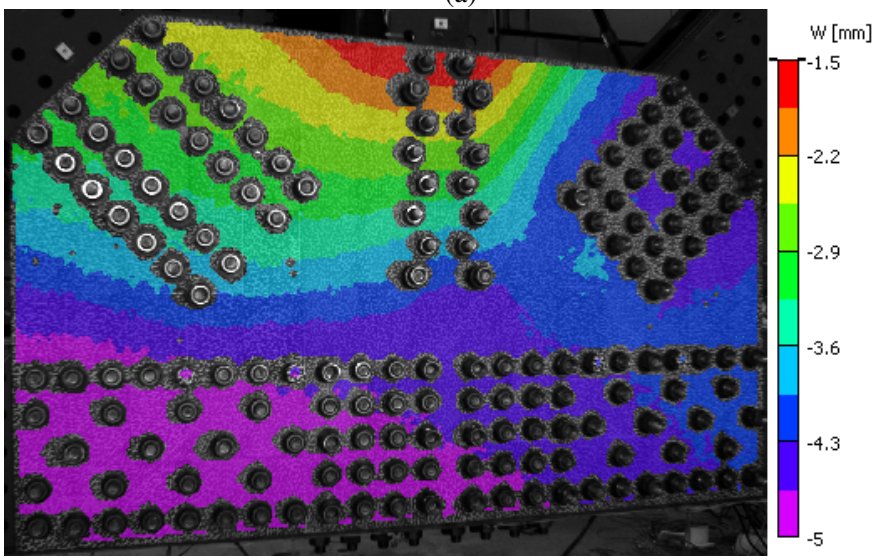

(b)

Figure 14: Out-of plane displacement (W) fields from the reference state to current plate shape for GP307-SS3 at ALF of (a) 0.30, (b) 0.40, (c) 0.57, and (d) 0.71 (failure).

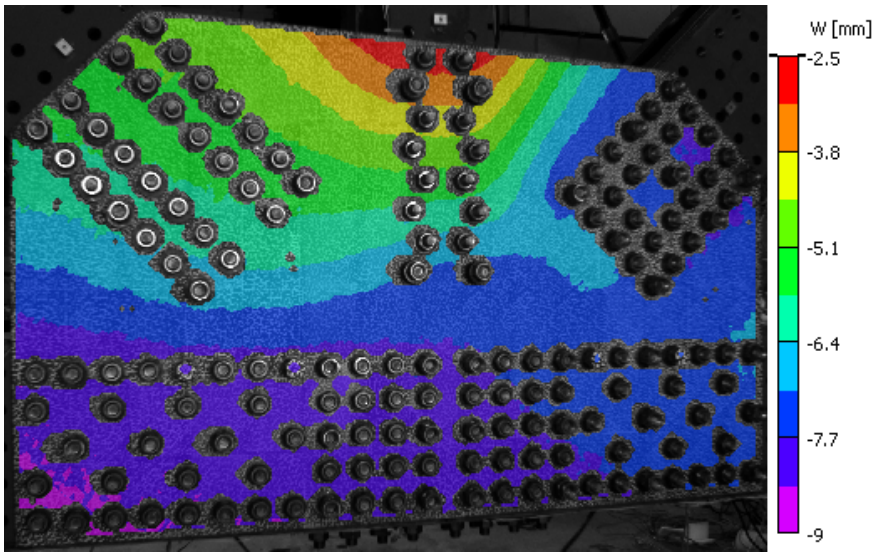

(c)

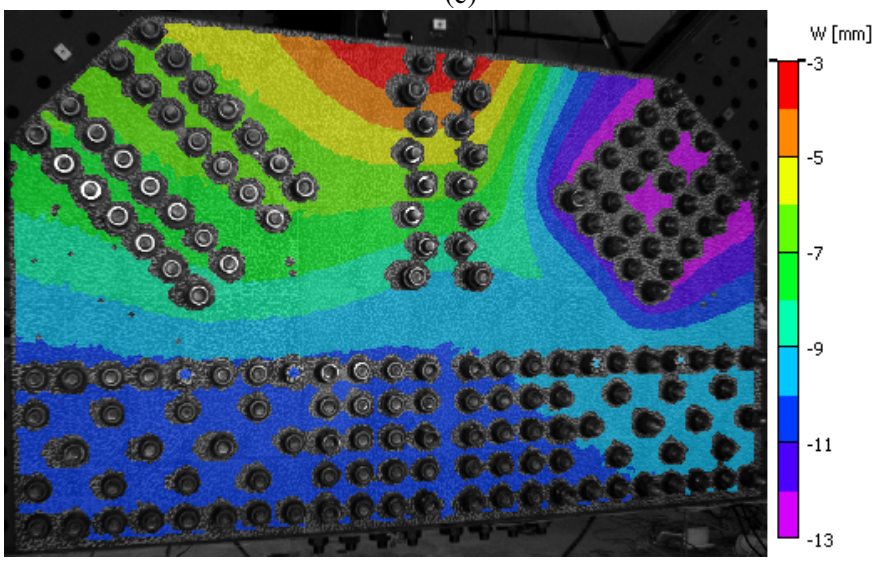

(d)

Figure 14 (continued)

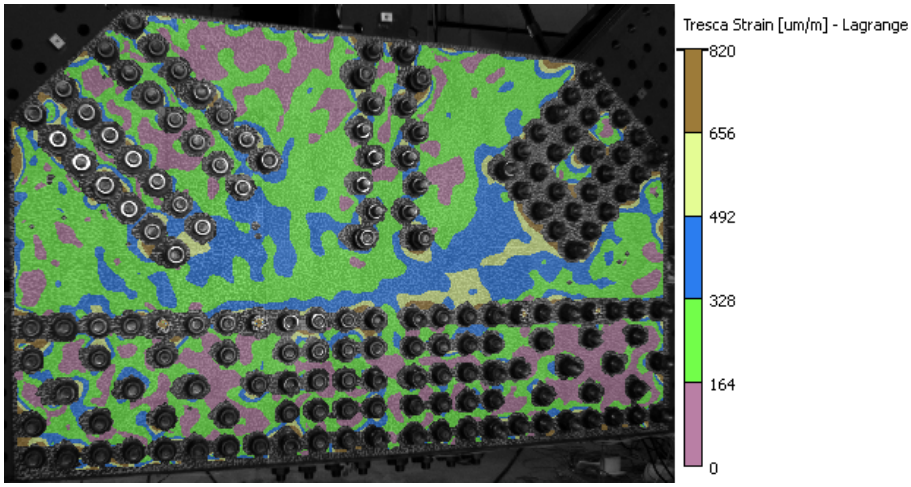

(a)

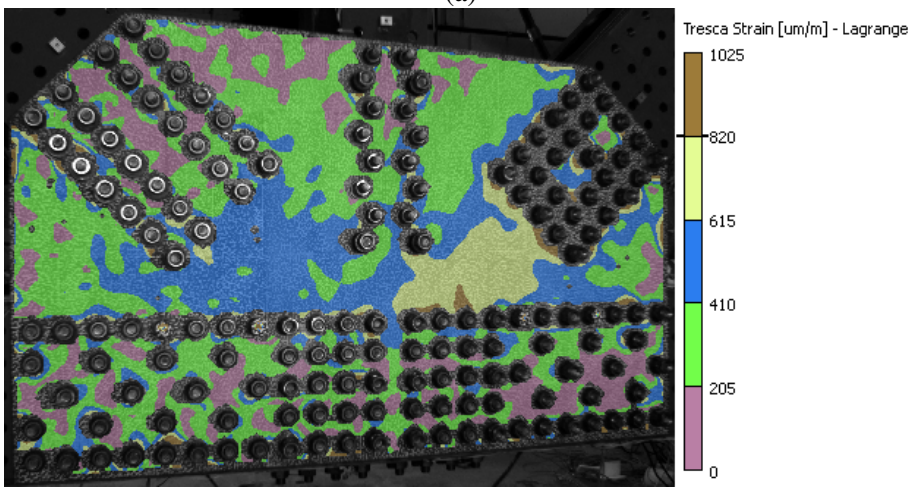

(b)

Figure 15: Maximum in-plane shear strain for GP307-SS3 at ALF of (a) 0.30, (b) 0.40, (c) 0.57, and (d) 0.71 (failure), with initial yield at 820 μm/m.

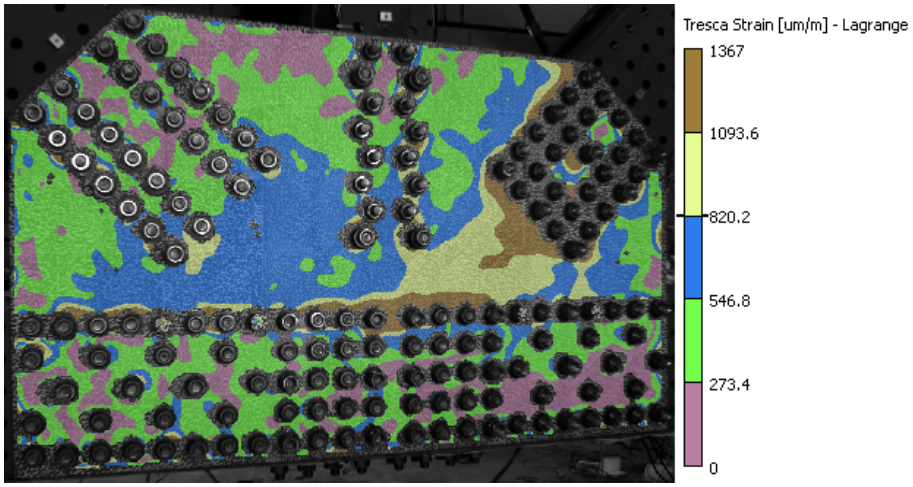

(c)

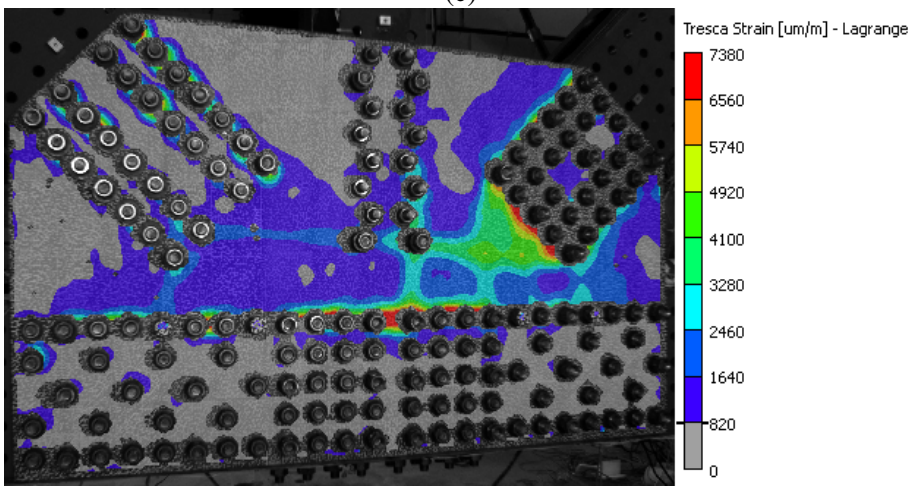

(d)

Figure 15 (continued)

7.2.2 GP307-LS3

Figure 16 shows the initial shape of GP307-LS3 at the start of the failure test under no load. This is the only plate tested with the East Chord in the tension configuration, which required moving of the hydraulic jacks (shown on Fig. 1a) to the outside of the East Abutment. The location of Z = 0 mm again was set using three points as described above. After the rotation, the plate has a saddle shape with the Tension Diagonal and West Chord in the positive Z-direction and the Compression Diagonal and East Chord in the negative Z-direction. The general shape is consistent with the measurements from the 3D laser point tracker, but the magnitude of the shape is four times larger as measured by DIC. The reason for this inconsistency could not be determined, but the laser system, which is designed to be very accurate in this range of measurement, is more likely correct. The uncertainties in W shown in Table 5 for GP307-LS3 are consistent with those seen by other researchers (Kujawinska et al., 2011; Smith et al., 2011), but Iadicola et al. (2012) showed a 0.6 mm maximum difference between the DIC and laser measured Z coordinates. Further analysis is needed to determine the reason for the large difference seen here, but none of the other variables (i.e., displacements or strains) show a similar distribution across the plate. Therefore these other values seem to not be affected, but should be checked against the other measurement methods (i.e., strain gauges or laser tracker) for verification similar to Iadicola et al. (2012).

Figure 17 shows the evolution of the Z-direction displacement from the initial shape in Fig. 16. The ALF values are in regards to the West Chord load (Table 4). During the test, the entire plate initially shifted toward the positive Z-direction (Fig. 17a and b), with the largest positive motion at the Tension diagonal. At higher load levels, the West half of the plate shifts in the negative Z-direction, with final buckling of the Compression Diagonal in that direction (Fig. 17d). Figure 18 plots the maximum in-plane shear strains at the same four ALF levels shown in Fig. 17. The yield strain in terms of Tresca strain is approximately 1080 μm/m, based on standard material testing of the same material. All the plots (Figures 18a–d) have strain ranges predominately in the elastic range and use a pseudorandom color map. The results show that the Tresca strains were concentrated between the ends of the Compression Diagonal and the West Chord from the early stages of loading, with the largest strains occurring at the end of the Compression Diagonal and along the Chord bolt lines. The strain field is more uniform in the early stages of loading, but the later two stages show more strain localization, which started to extend between the various bolt lines by the point of failure (ALF = 1.14).

7.2.3 GP307-SL3

Figure 19 shows the initial shape of GP307-SL3 at the start of the failure test under no load, after the plate was rotated to the selected coordinate system. After that rotation, the plate is relatively flat with a slight depression near the East Chord bolt line. Figure 20 shows the evolution of the Z-direction displacement from the initial shape in Fig. 19. The ALF values are in regards to the Compression Diagonal load (Table 4). During the test, the entire plate shifted toward the negative Z-direction from an early stage, until the final buckling of the Compression Diagonal in the positive Z-direction (Fig. 20d). Figure 21 plots the maximum in-plane shear strains at the same four ALF levels shown in Fig. 20. The yield strain in terms of Tresca strain is approximately

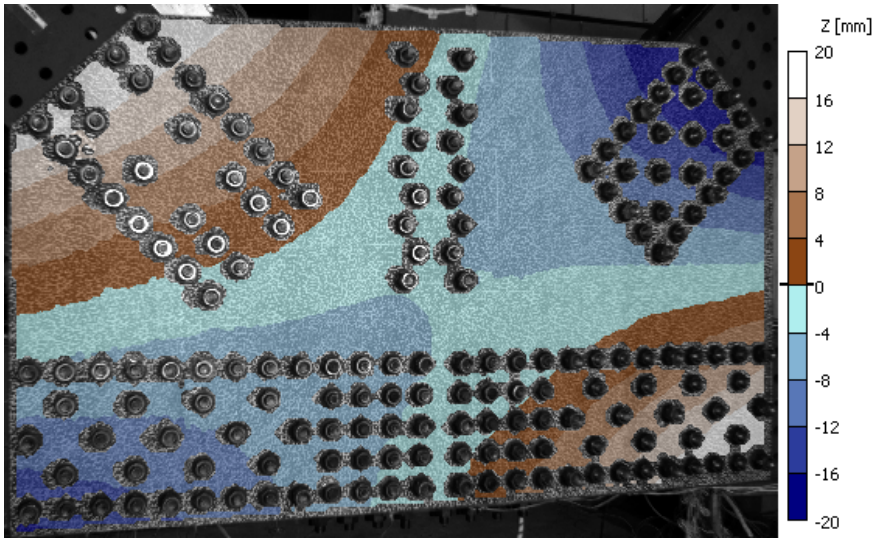

Figure 16: Out-of-plane shape of specimen GP307-LS3 at zero load (ALF = 0).

1040 μm/m, based on standard material testing of the same material. Figures 21a–c have strain ranges predominately in the elastic range and use a pseudorandom color map. Figure 21d has a strain range predominately in the plastic strain range (spectrum color map) with grey being used for areas of the plate that have not yet reached the yield strain. The results show that the Tresca strains were concentrated between the ends of the Compression and Tension Diagonals during the early stages of loading (Fig. 21a and b), with the largest strains occurring at the end of the Compression Diagonal and along the Chord bolt lines. The strain field is more uniform in the early stages of loading (Fig. 21a and b), but the later two stages (Fig. 21c and d) show more strain localizations, which extend across the plate between the diagonal bolt lines through the end of the Vertical bolts. Additional strain localizations of lower magnitude extend from this bands down to the Chord bolt lines.

7.2.4 GP307-SL4

Figure 22 shows the initial shape of GP307-SL4 at the start of the failure test under no load. The location of Z = 0 mm was set using three points as described above. After rotation, the plate has a slight saddle shape with the Tension Diagonal and West Chord in the positive Z-direction, and the Compression Diagonal and East Chord in the negative Z-direction. Figure 23 shows the evolution of the Z-direction displacement from the initial shape in Fig. 22. The ALF values are in regards to the Compression Diagonal load (Table 4). During the test, the plate shifted continuously toward the negative Z-direction. The Compression Diagonal, which started in the negative Z-direction (Fig. 22), shifted further in that direction through the buckling of the plate (Fig. 23a–d). Figure 24 plots the maximum in-plane shear strains at the same four ALF levels shown in Fig. 23. The yield strain in terms of Tresca strain is approximately 740 μm/m, based on standard material testing of

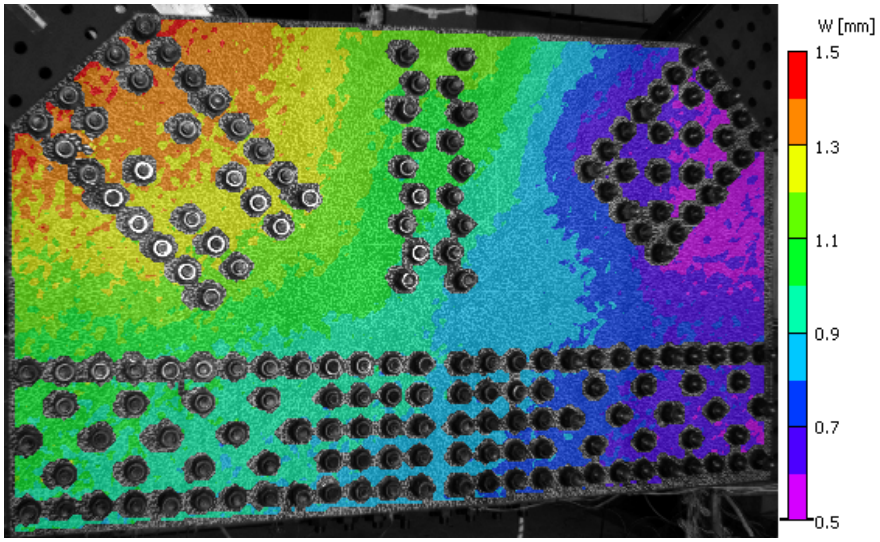

(a)

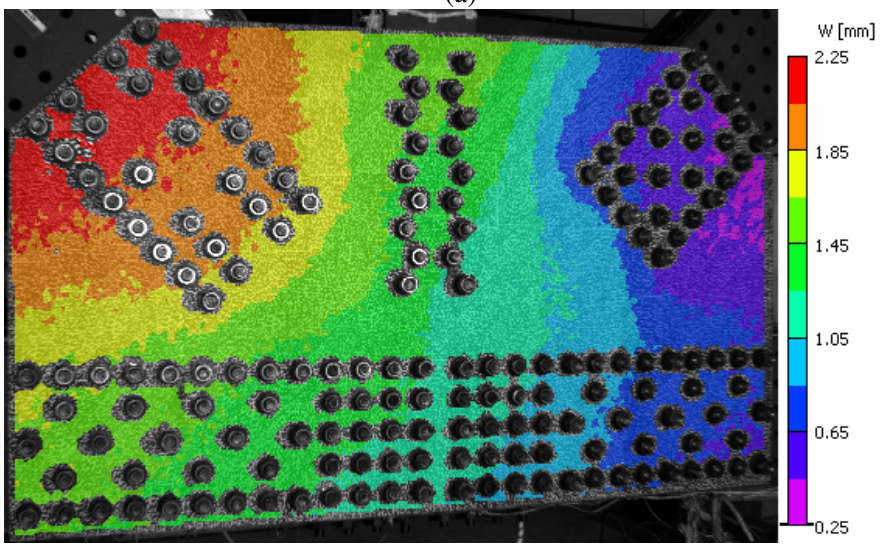

(b)

Figure 17: Out-of plane displacement (W) fields from the reference state to current plate shape for GP307-LS3 at ALF of (a) 0.21, (b) 0.40, (c) 0.98, and (d) 1.14 (failure).

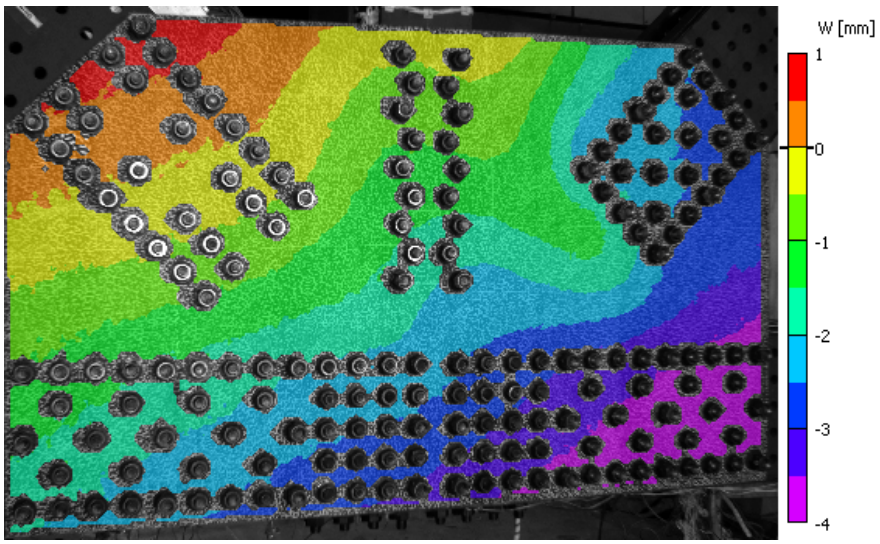

(c)

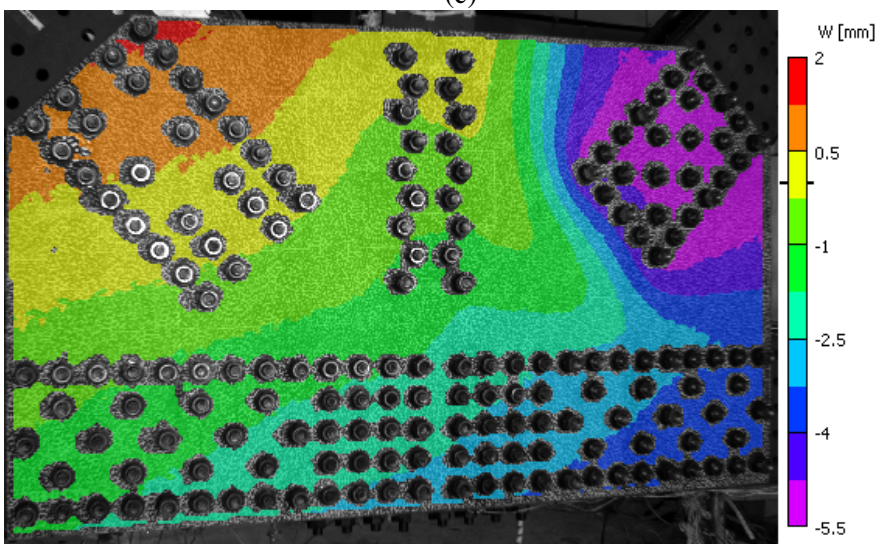

(d)

Figure 17 (continued)

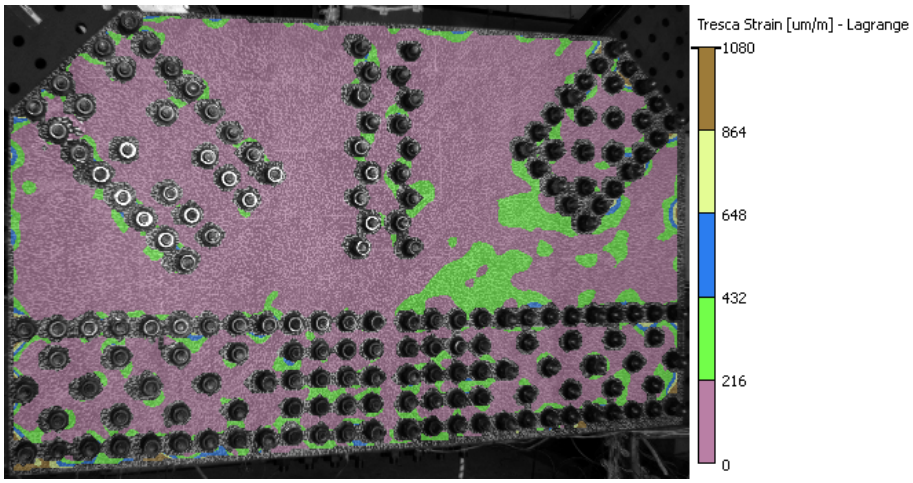

(a)

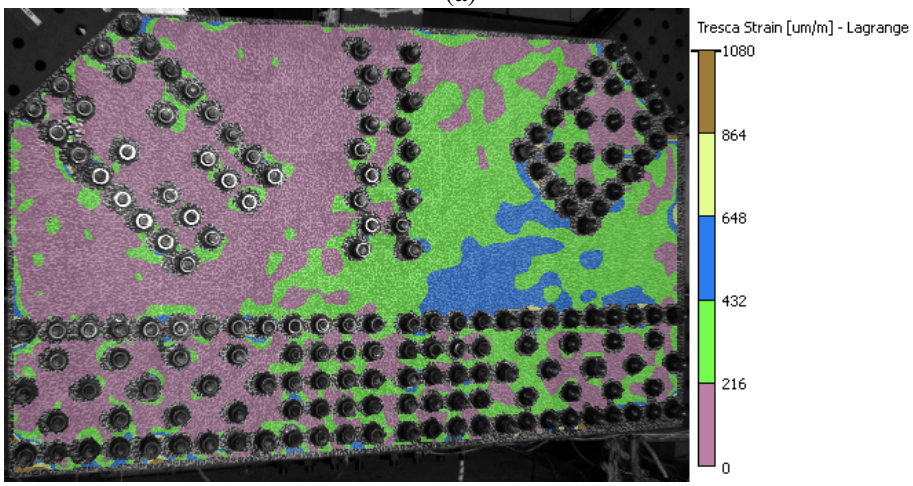

(b)

Figure 18: Maximum in-plane shear strain for GP307-LS3 at ALF of (a) 0.21, (b) 0.40, (c) 0.98, and (d) 1.14 (failure), with initial yield at 1080 μm/m.

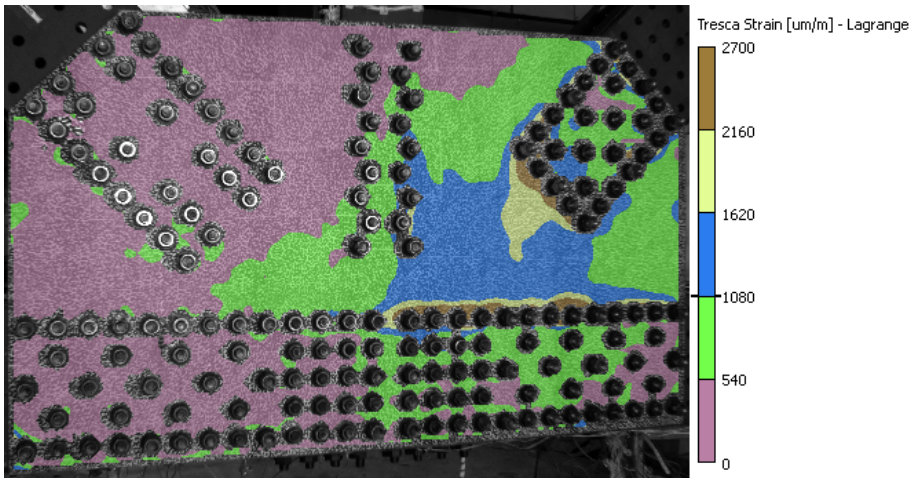

(c)

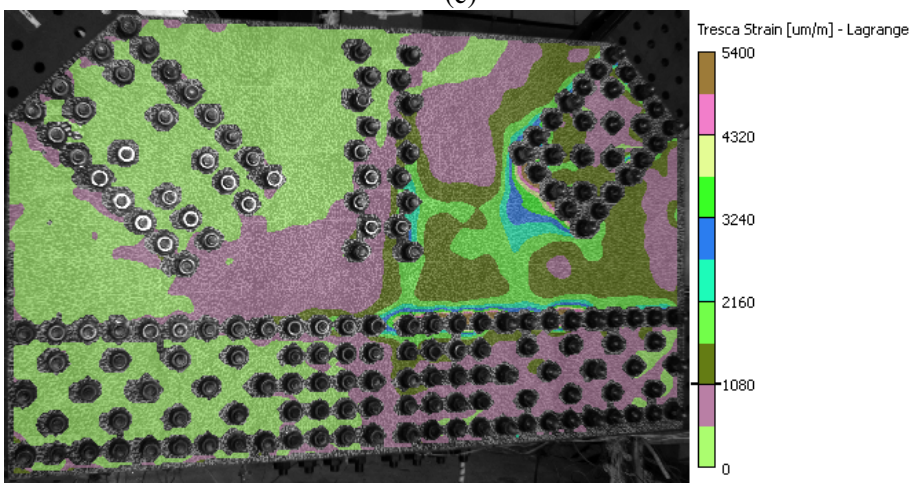

(d)

Figure 18 (continued)

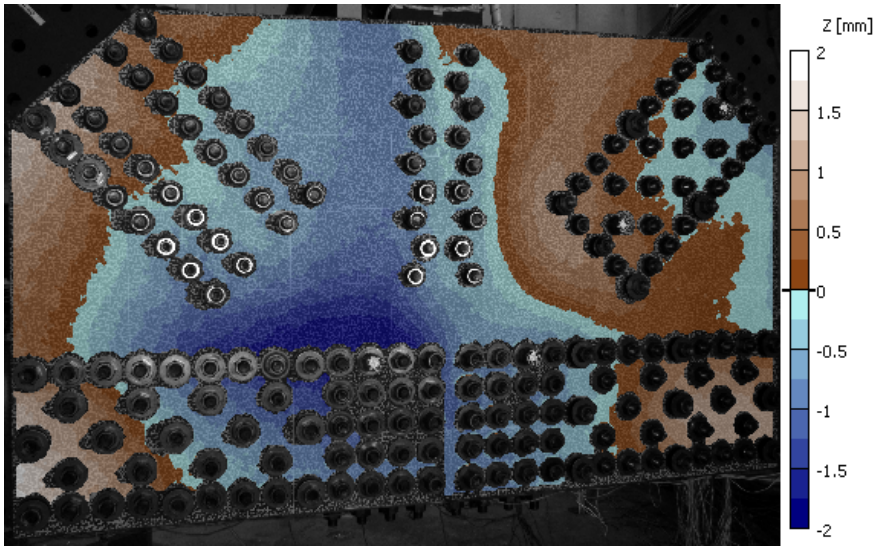

Figure 19: Out-of-plane shape of specimen GP307-SL3 at zero load (ALF = 0).

the same material. Figures 24a and b have strain ranges predominately in the elastic range and use a pseudorandom color map. Figure 24c and d have strain ranges predominately in the plastic strain range (spectrum color map) with grey being used for areas of the plate that have not yet reached yield. The results show that the Tresca strains were concentrated between the ends of the Compression and Tension Diagonals from the early stages of loading, with the largest strains occurring at the ends of the diagonal bolt lines and along the Chord bolt lines (Fig. 24b). The strain field is more diffuse in the early stages of loading (Fig. 24a and b). In the later stages (Fig. 24c and d) more strain localizations are present, starting in Fig. 24c and extend between the Tension and Compression Diagonal bolt lines though the end of the Vertical bolt line with various extensions down to the Chord bolt lines. The highest strains were seen along the Chord bolt line starting as early as ALF = 0.52 (Fig 24b).

7.2.5 GP307-SS3-1

Figure 25 shows the initial shape of GP307-SS3-1 at the start of the failure test under no load, after rotation to the selected coordinate system. Note that GP307-SS3-1 is one of the plates that has a reduced thickness as an analog for section loss due to corrosion (Fig. 2). The thinner section is on the Compression Diagonal half of the plate. After the rotation, the plate has a slight saddle shape with the Tension Diagonal and West Chord in the positive Z-direction, and the Compression Diagonal and East Chord in the negative Z-direction. Figure 26 shows the evolution of the Z-direction displacement from the initial shape in Fig. 25. The ALF values are in regards to the Compression Diagonal load (Table 4). During the test, the majority of the plate shifted toward the negative Z-direction with the exception of the Tension Diagonal that moved in the positive Z-direction. The Compression Diagonal, which started in the negative Z-direction, shifted further in that direction through the buckling of the plate always with a convex bulge of the plate under the Compression Diagonal (Fig. 26a–d). Figure 27 plots the maximum in-plane shear strains at the same four ALF levels shown in Fig. 26. The yield strain in terms of Tresca strain is approximately 1060 μm/m, based on standard material testing of the same material. Figures 27a–c have strain ranges predominately in the elastic range and use a pseudorandom color map. Figure 27d has a strain range predominately in the plastic strain range (spectrum color map) again with grey being used for areas of the plate that have not yet reached yield. The results show that the Tresca strains were concentrated between the end of the Compression Diagonal and the West Chord from the early stages of loading, with the largest strains occurring at the end of the Compression Diagonal (Fig. 27c and d). This is the area of the plate with the thinnest cross-section, and this thinned down area is somewhat visible in the strain field (compare Fig. 27c to Fig. 2 for GP307-SS3-1). Unlike many of the other tests to failure, the strain field did not localize into bands extending from the bolt lines, but instead showed highest strain at the Compression Diagonal bolt line nearest to the buckling (Fig. 27d).

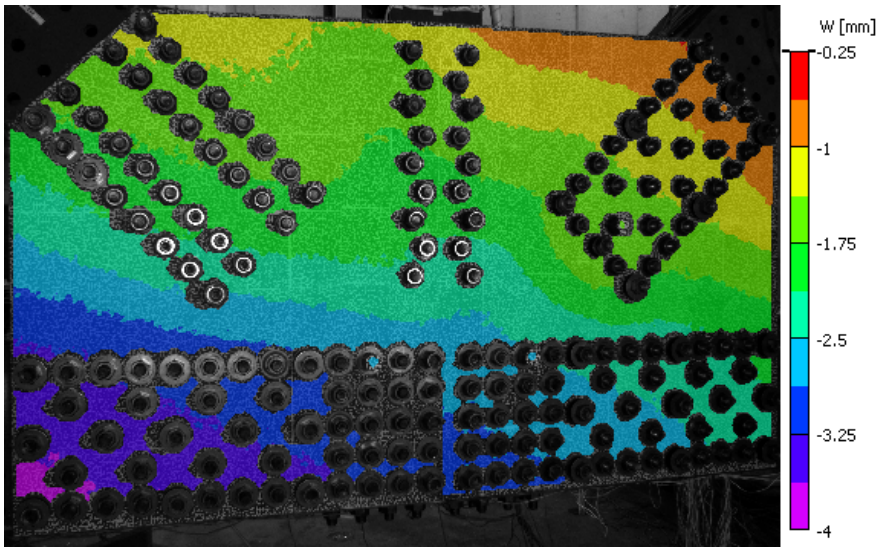

(a)

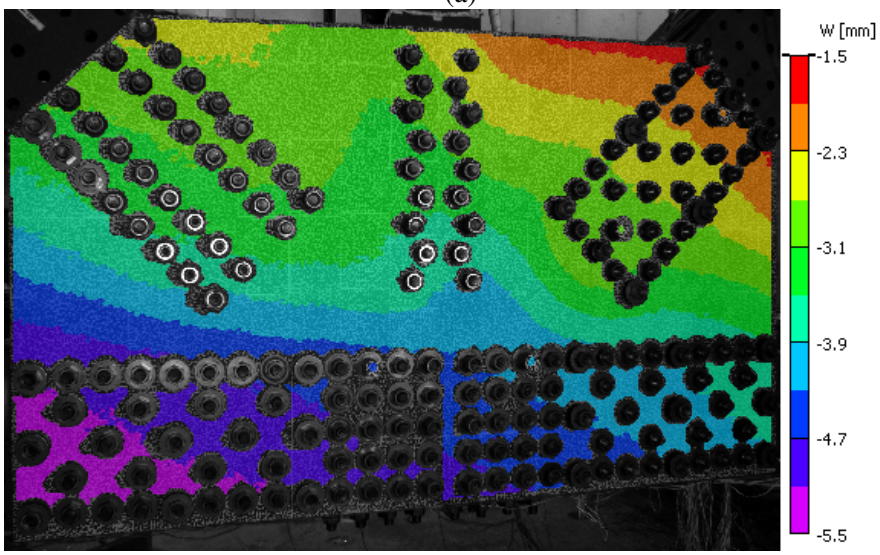

(b)

Figure 20: Out-of plane displacement (W) fields from the reference state to current plate shape for GP307-SL3 at ALF of (a) 0.33, (b) 0.52, (c) 0.68, and (d) 0.95 (failure).

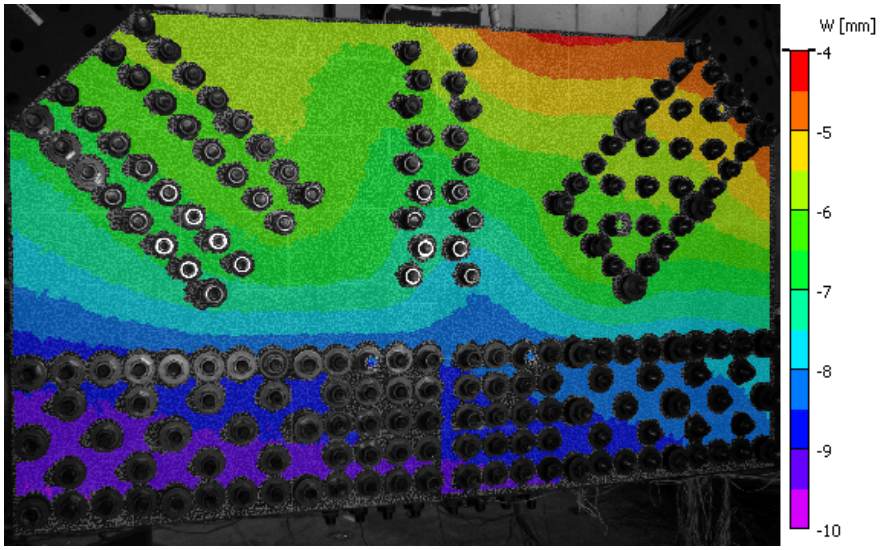

(c)

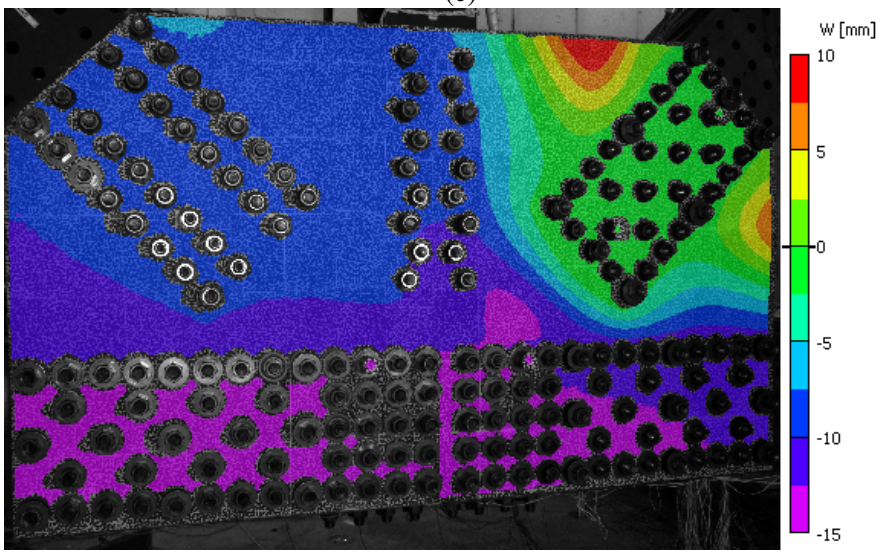

(d)

Figure 20 (continued)

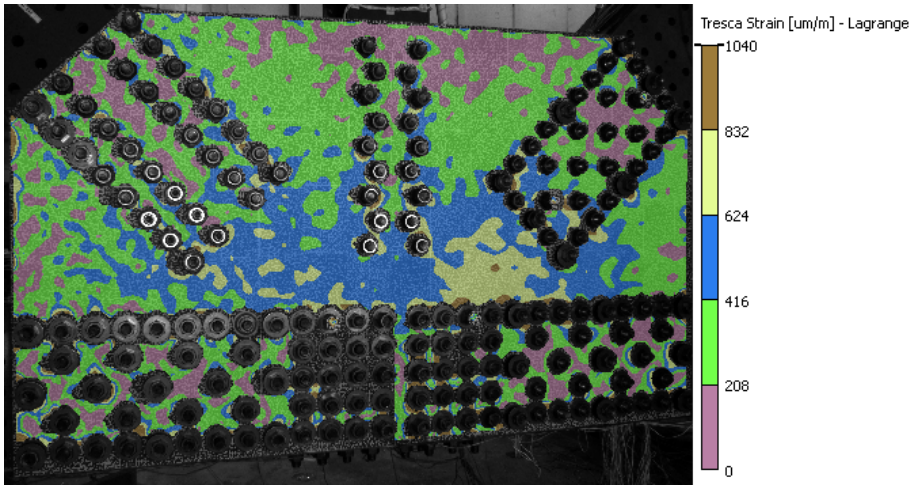

(a)

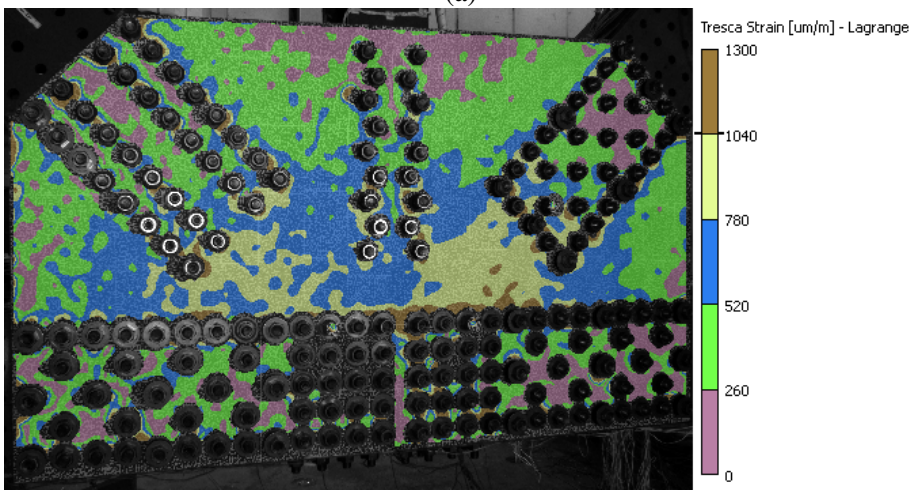

(b)

Figure 21: Maximum in-plane shear strain for GP307-SL3 at ALF of (a) 0.33, (b) 0.52, (c) 0.68, and (d) 0.95 (failure), with initial yield at 1040 μm/m.

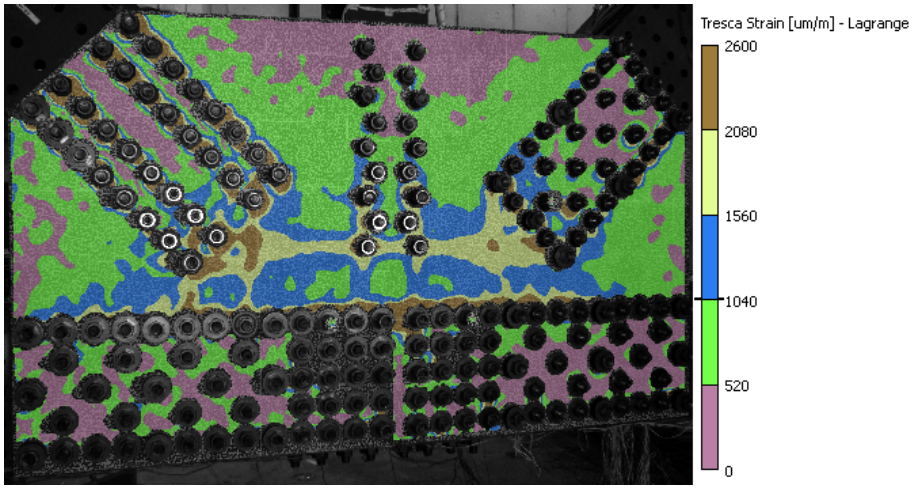

(c)

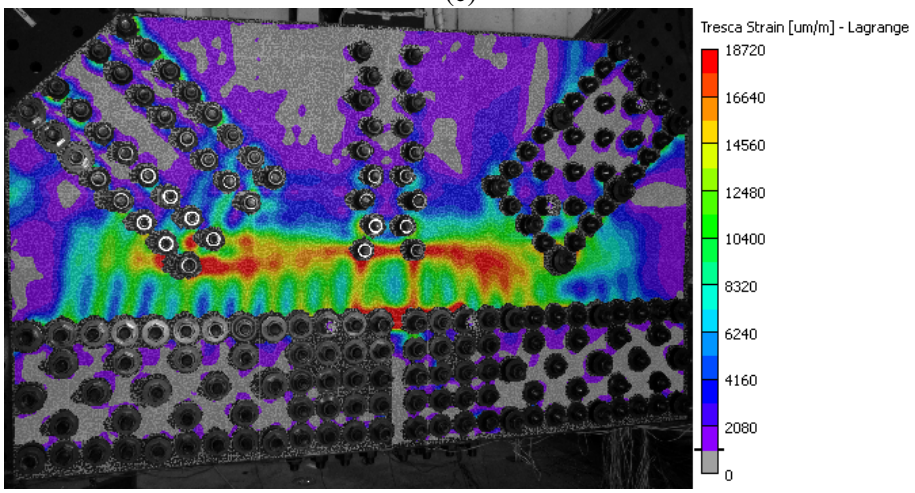

(d)

Figure 21 (continued)

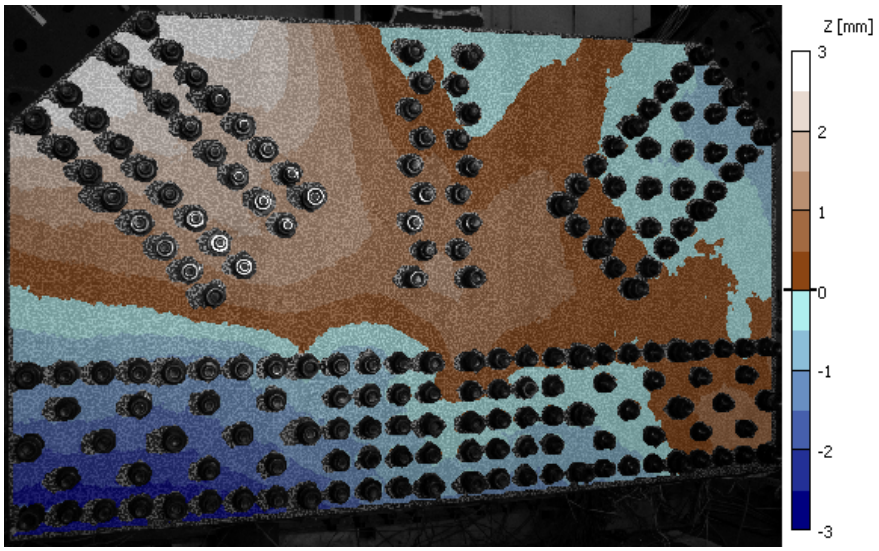

Figure 22: Out-of-plane shape of specimen GP307-SL4 at zero load (ALF = 0).

7.2.6 GP307-SS3-2

Specimen GP307-SS3-2 also is one of the samples that had a section machined to represent section loss due to corrosion, with the area near the Tension Diagonal being the thinnest cross-section (Fig. 2). Figure 28 shows the initial shape of GP307-SS3-2 at the start of the failure test under no load, after the location of Z = 0 mm was set using three points as described above. After the rotation, the plate has a slight overall tilt from positive Z at the bottom of the chords to negative Z at the upper edge of the plate, with the Compression Diagonal being farthest in the negative Z-direction. Figure 29 shows the evolution of the Z-direction displacement from the initial shape in Fig. 28. The ALF values are in regards to the Tension Diagonal load (Table 4). During the test, the plate shifted toward the negative Z-direction through the final buckling of the plate at the Compression Diagonal (Fig. 29a–d). The plate at maximum load (Fig. 29d) shows three convex bulges. Two exist from the early stages of the test in areas that have reduced thickness: one between the Compression Diagonal and West Chord, and one between the Tension Diagonal, Vertical, and East Chord. The last convex bulge occurred under the Tension Diagonal starting sometime after ALF = 0.36. Figure 30 plots the maximum in-plane shear strains at the same four ALF levels shown in Fig. 29. The yield strain in terms of Tresca strain is approximately 1070 μm/m, based on standard material testing of the same material. Figures 30a and b have strain ranges predominately in the elastic range and use a pseudorandom color map. Figure 30c and d have strain ranges predominately in the plastic strain range (spectrum color map) with grey being used for areas of the plate that have not yet reached yield. The results show that the Tresca strains were concentrated from an early stage in the field areas of the plate, between the end of the diagonals and the chord, with the largest strains occurring at the end of the Tension Diagonal in the thinnest portion of the machined section. Unlike many of the other tests to failure, the strain field did not localize into bands extending from the bolt lines, but instead showed the strain concentrated in the thinned sections of the plate or near the limits of the thinned sections (see Fig. 2 GP307-SS3-2, Fig. 30c and d).

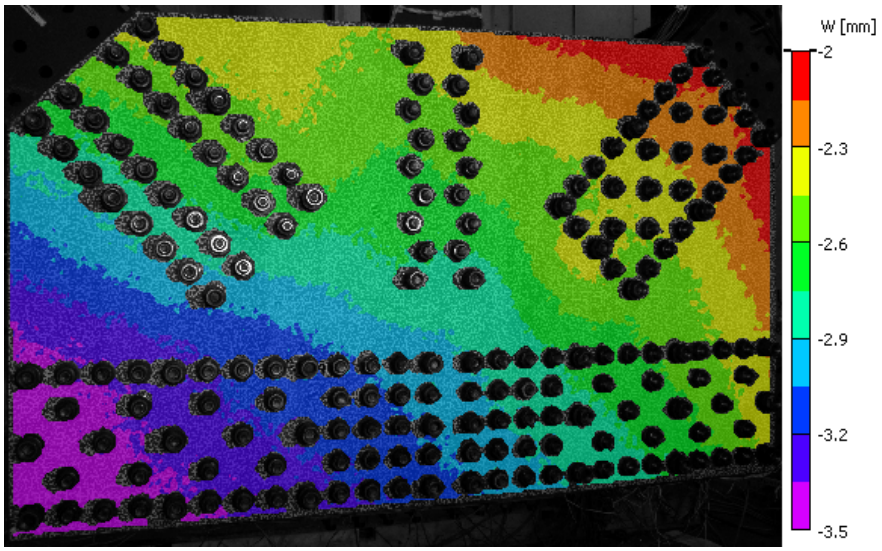

(a)

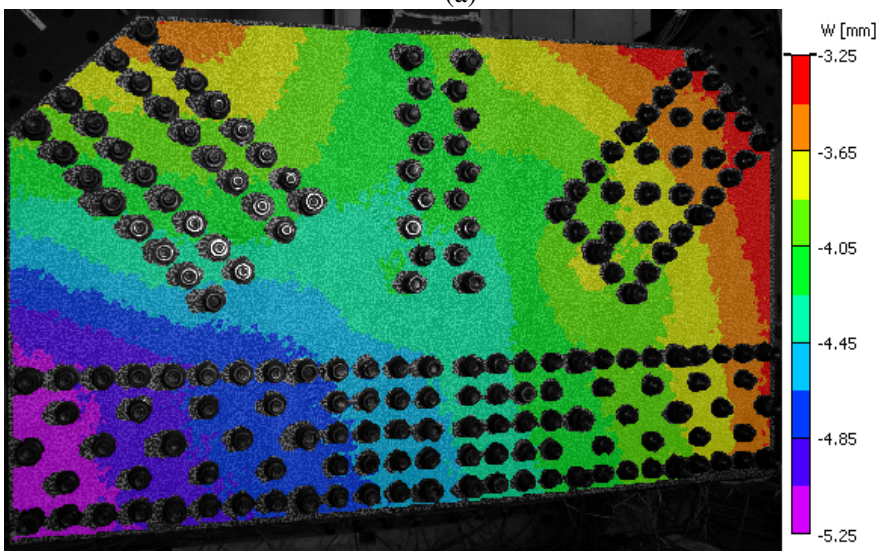

(b)

Figure 23: Out-of plane displacement (W) fields from the reference state to current plate shape for GP307-SL4 at ALF of (a) 0.36, (b) 0.52, (c) 0.80, and (d) 1.07 (failure).

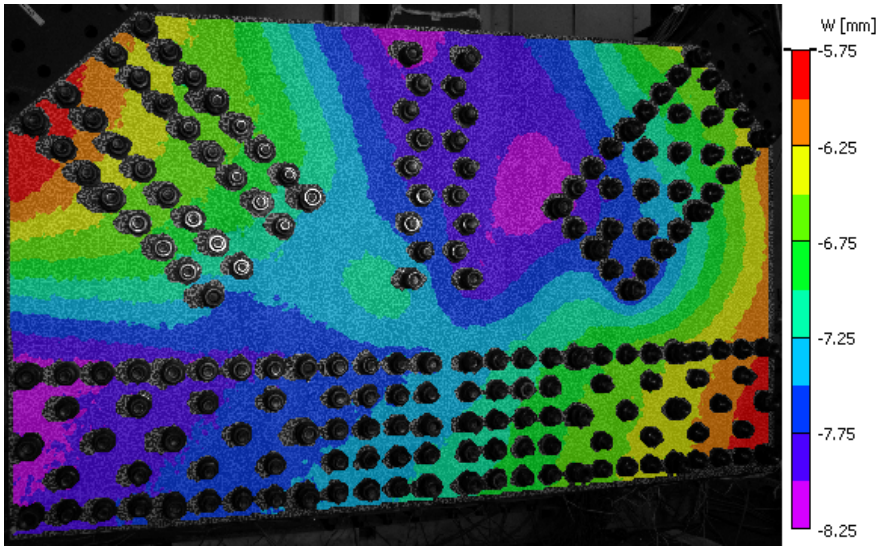

(c)

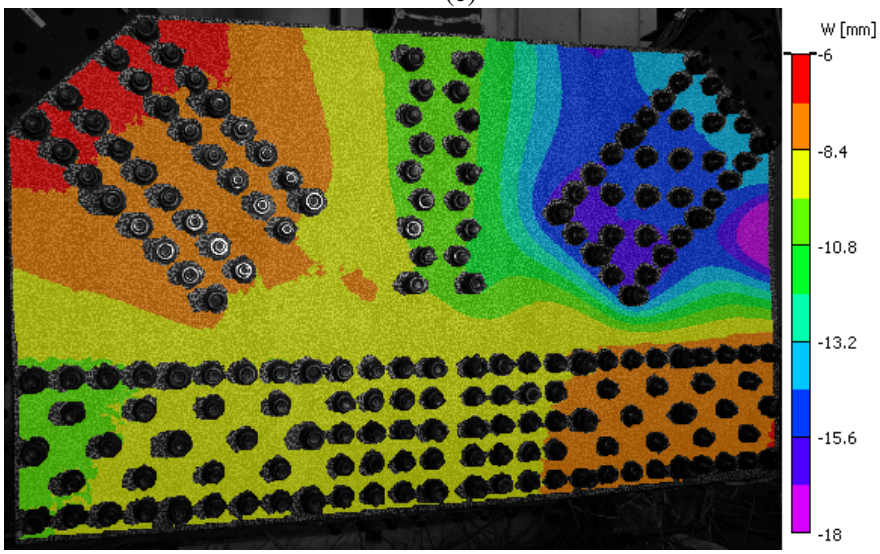

(d)

Figure 23 (continued)

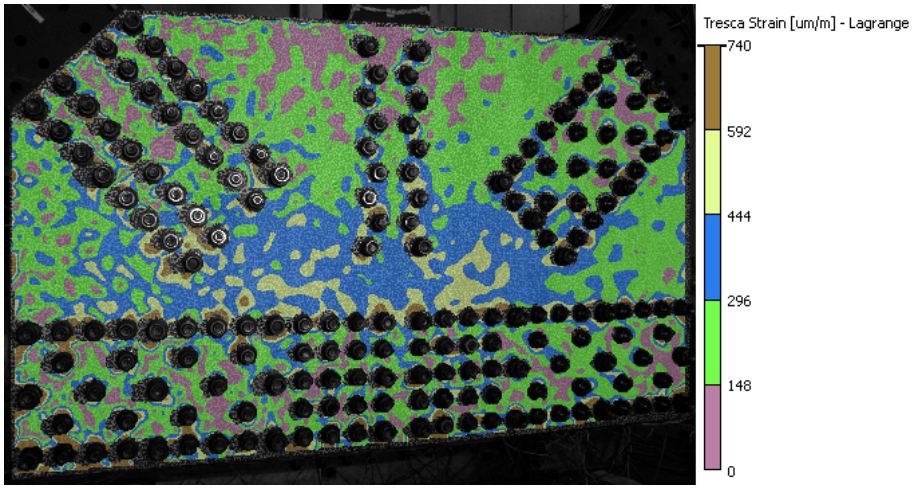

(a)

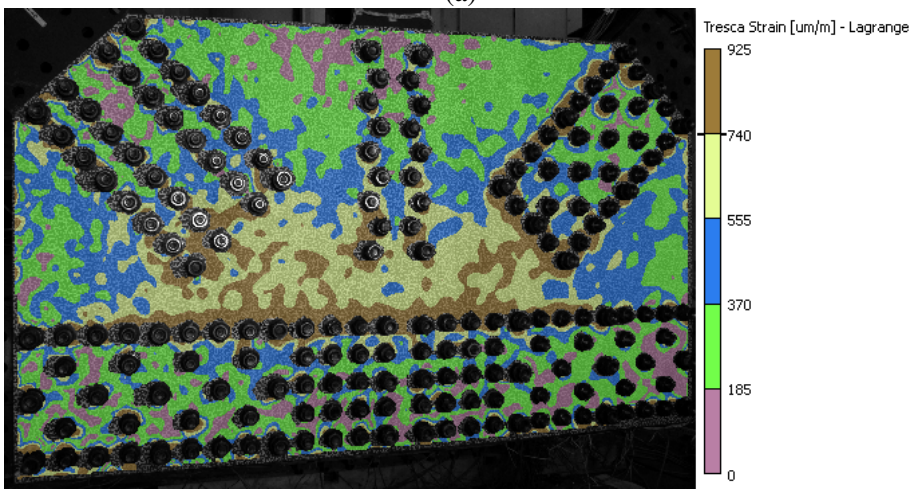

(b)

Figure 24: Maximum in-plane shear strain for GP307-SL4 at ALF of (a) 0.36, (b) 0.52, (c) 0.80, and (d) 1.07 (failure), with initial yield at 740 μm/m.

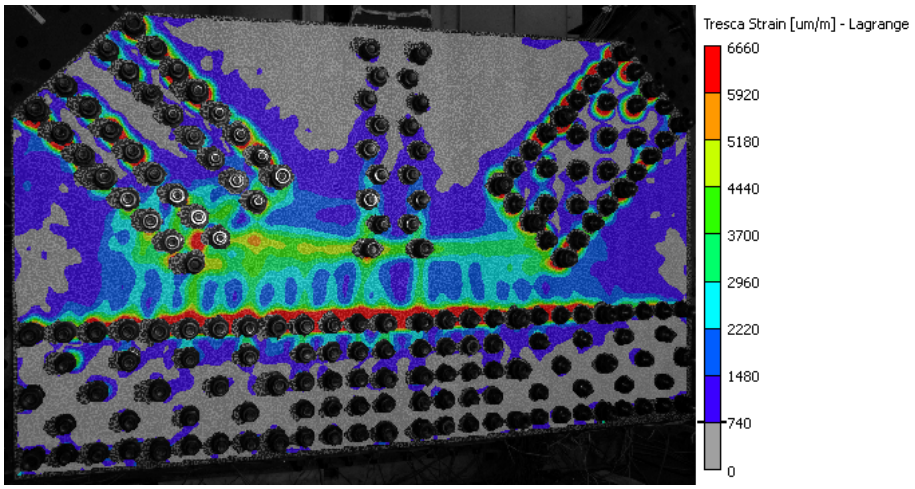

(c)

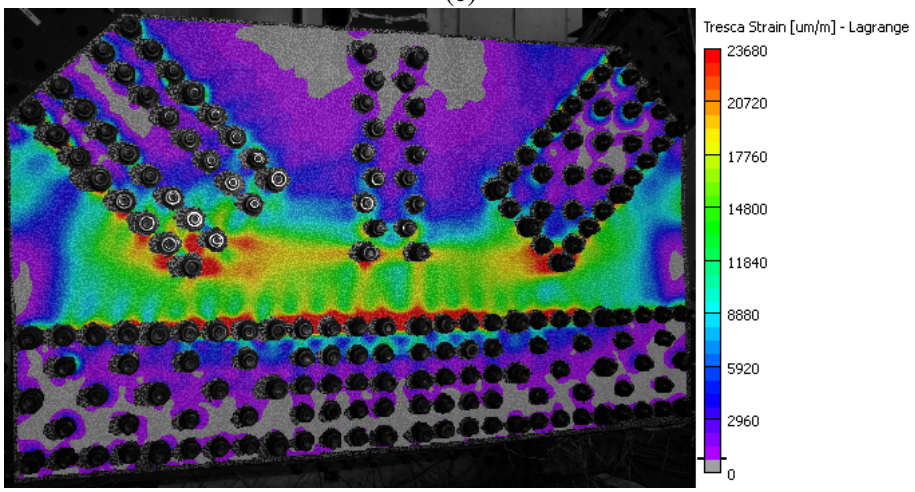

(d)

Figure 24 (continued)

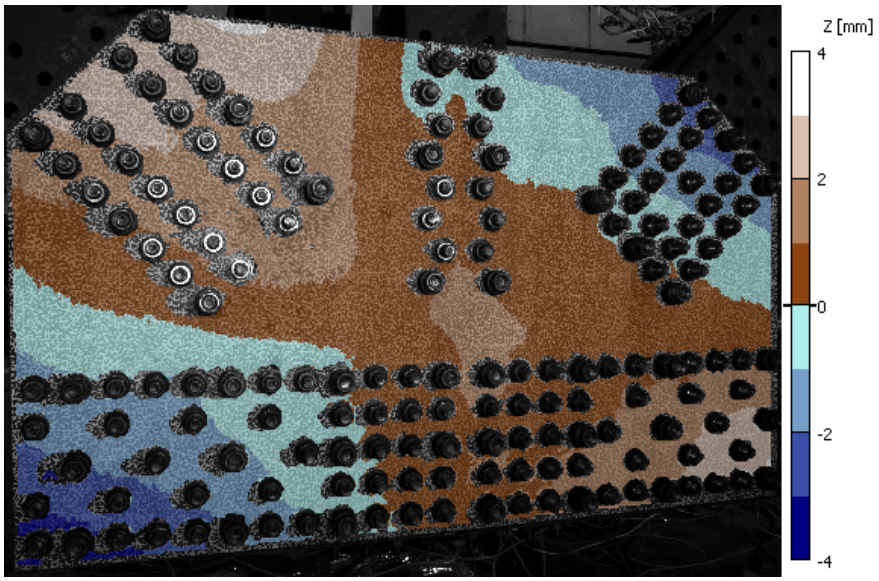

Figure 25: Out-of-plane shape of specimen GP307-SS3-1 at zero load (ALF = 0).

7.2.7 GP307-SS3-3

Specimen GP307-SS3-3 is one of the samples that had a long thin section machined above the Chord bolt line to represent section loss due to corrosion (Fig. 2). Figure 31 shows the initial shape of GP307-SS3-3 at the start of the failure test under no load, after rotation to the selected coordinate system. After that rotation, the plate has a slight saddle shape with the Tension Diagonal and West Chord in the positive Z-direction, and the Compression Diagonal and East Chord in the negative Z-direction. Figure 32 shows the evolution of the Z-direction displacement from the initial shape in Fig. 31. The ALF values are in regards to the Tension Diagonal load (Table 4). During the test, the plate shifted continuously toward the negative Z-direction. The Compression Diagonal, which started in the negative Z-direction, shifted further in that direction through the final buckling of the plate (Fig. 32b and c), and always with a slight convex bulge of the plate near the West Chord bolt line under the Compression Diagonal (Fig. 32b–d). Figure 33 plots the maximum in-plane shear strains at the same four ALF levels shown in Fig. 32. The yield strain in terms of Tresca strain is approximately 850 μm/m, based on standard material testing of the same material. Figures 33a and b have strain ranges predominately in the elastic range and use a pseudorandom color map. Figure 33c and d have strain ranges predominately in the plastic strain range (spectrum color map) with grey being used for areas of the plate that have not yet reached yield. The results show that the Tresca strains were concentrated from an early stage in the section of the plate with reduced thickness, just above the Chord bolt lines. Unlike many of the other tests without reduced sections, the strain field did not localize into bands extending from the bolt lines, but instead showed the strain concentrated in the thinned section of the plate from the early stages of plastic deformation (Fig. 33a–d). Some strain localization is seen along the Vertical bolt line and extending from the Tension Diagonal, but the magnitude is much less then the thinned section (Fig. 33c and d).

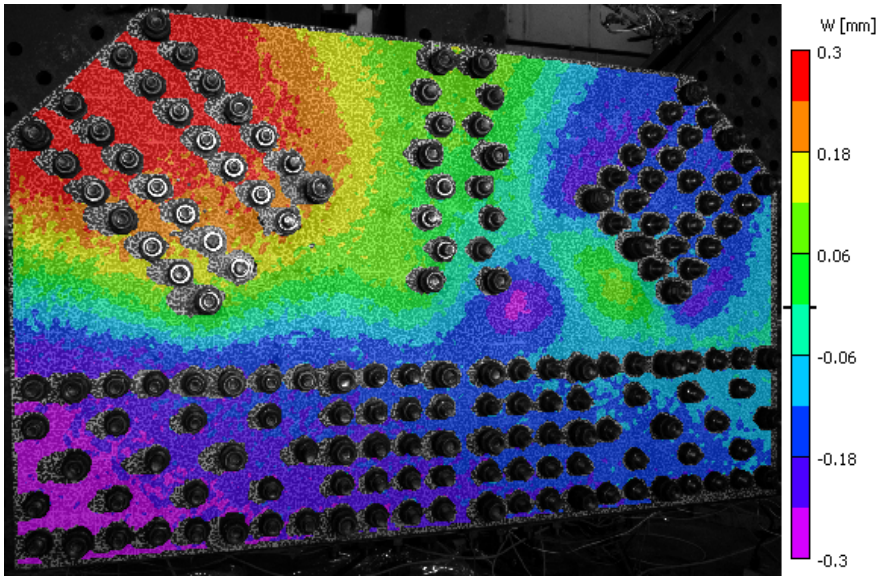

(a)

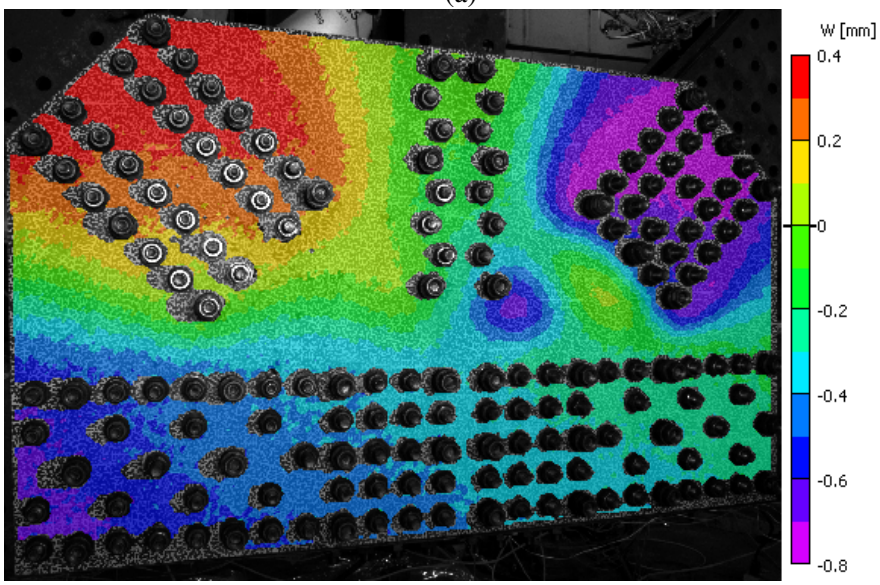

(b)

Figure 26: Out-of plane displacement (W) fields from the reference state to current plate shape for GP307-SS3-1 at ALF of (a) 0.12, (b) 0.26, (c) 0.35, and (d) 0.45 (failure).

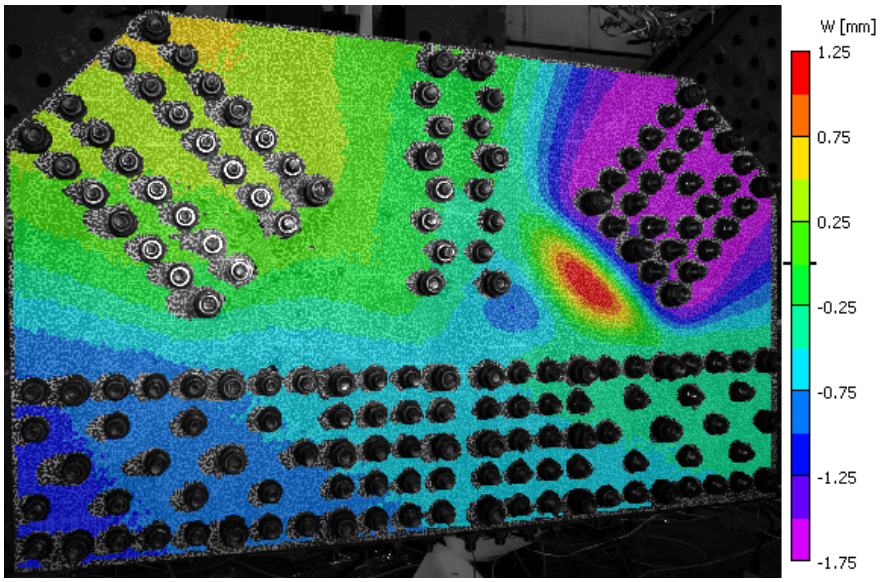

(c)

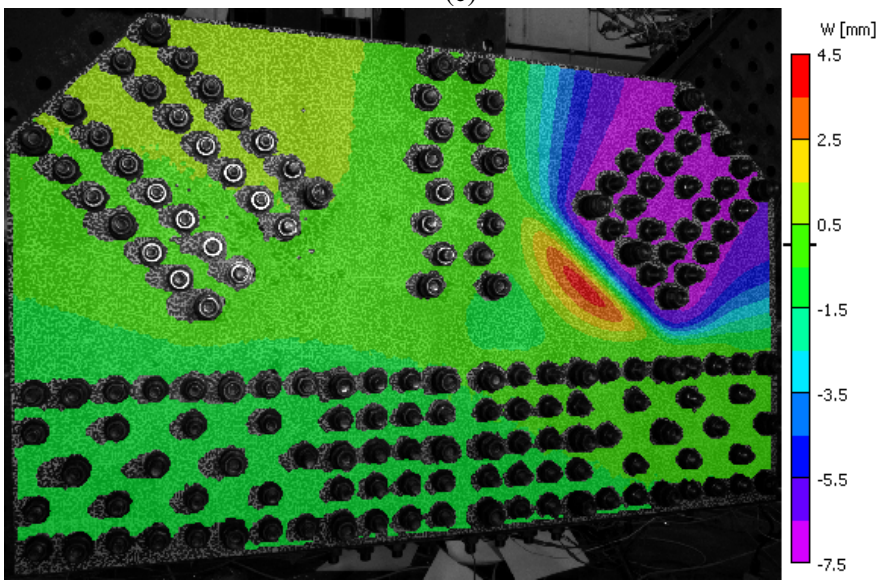

(d)

Figure 26 (continued)

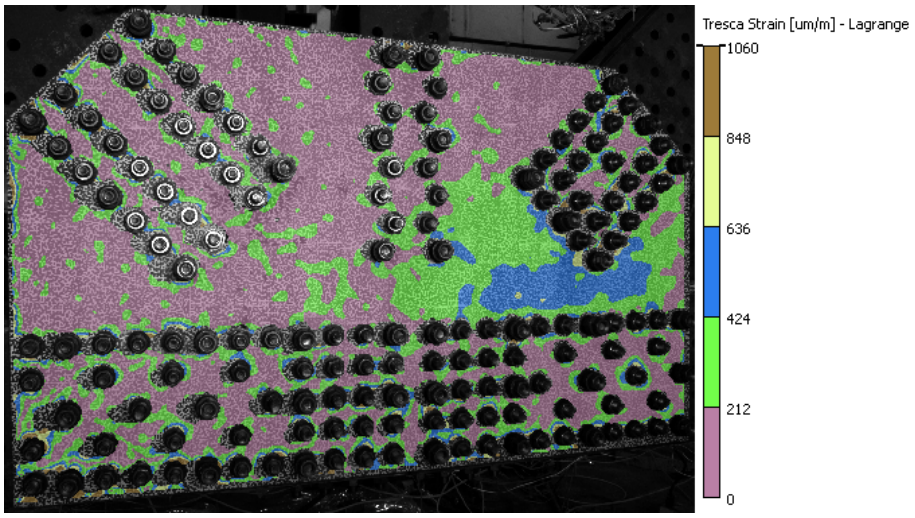

(a)

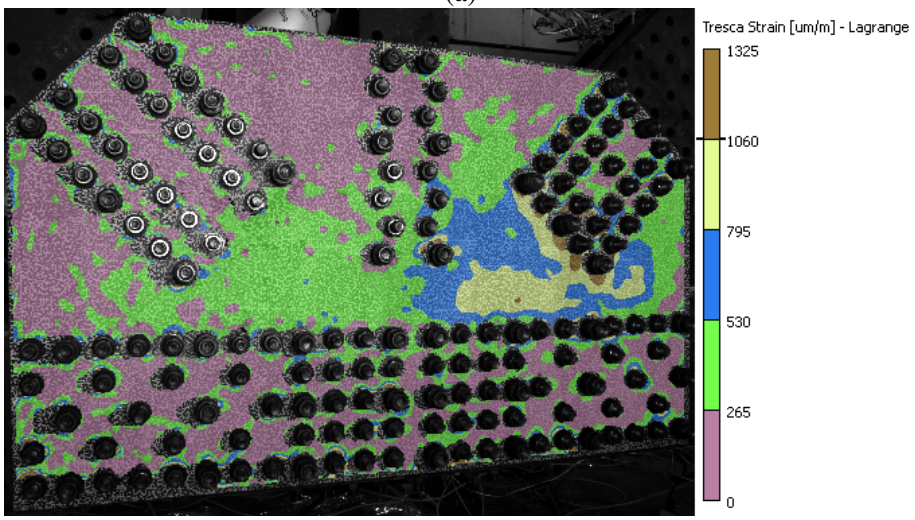

(b)

Figure 27: Maximum in-plane shear strain for GP307-SS3-1 at ALF of (a) 0.12, (b) 0.26, (c) 0.35, and (d) 0.45 (failure), with initial yield at 1060 μm/m.

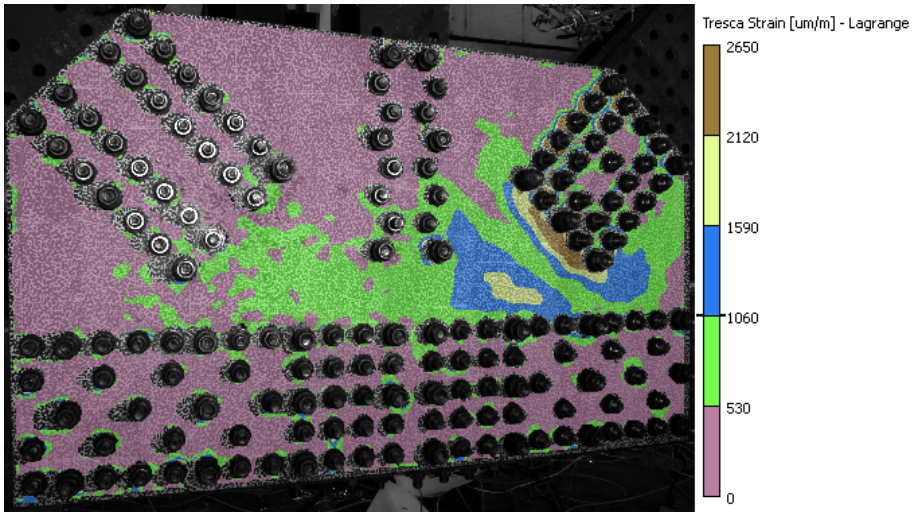

(c)

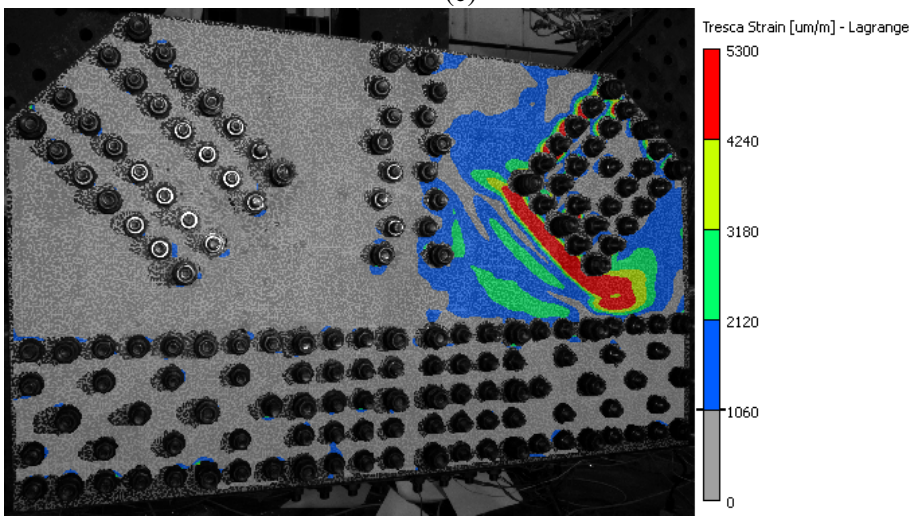

(d)

Figure 27 (continued)

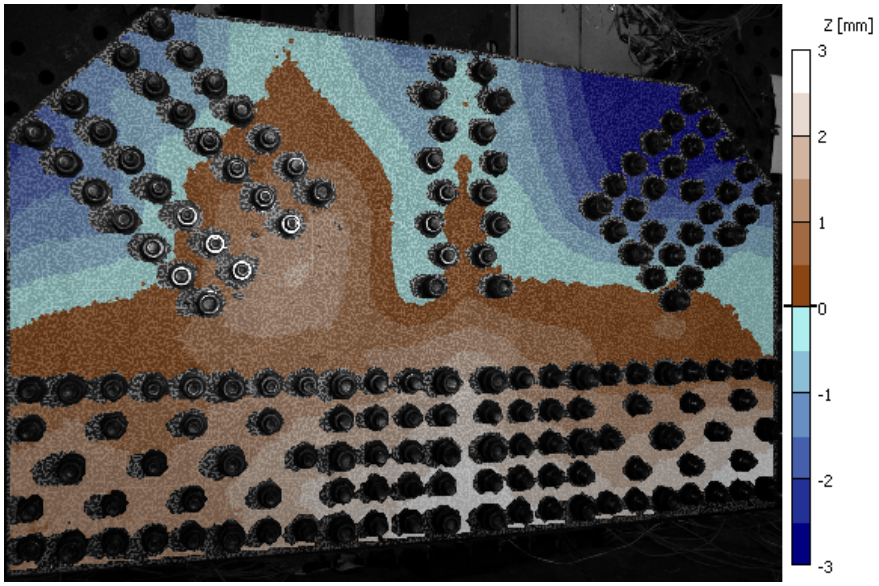

Figure 28: Out-of-plane shape of specimen GP307-SS3-2 at zero load (ALF = 0).

7.2.8 GP307-SS3-4

Specimen GP307-SS3-4 was tested with the addition of a shingle plate (GP307-SS3-shingle) on the North face of the connection. GP307-SS3-4 has a long thin section of the plate with reduced thickness just above the Chord bolt line (Fig. 2) as an analog to a corroded gusset plate. The shingle plate covers most, but not all, of this thinner section. This test is also unique in that there was a premature failure of the Tension bolts prior to failure of either plate. After this premature failure, some bolt holes in the plate along the Tension Diagonal had to be enlarged to permit reassembly of the connection. This substantially damaged the DIC pattern on the shingle plate, but did only minor damage to the pattern on the visible portion of the gusset plate. For the gusset plate, the damaged pattern still permitted correlation of the gusset plate from the start of testing through the bolt failures and to failure (after reassembly), but this is not the case for the shingle plate. For the shingle plate, the extent of the pattern damage near the Tension Diagonal made it impossible to correlate from the reassembled state to the original condition of the plate. Therefore the results presented are split into two sets: one set for for the visible portion of GP307-SS3-4 that covers the entire test to failure (using the calibration for GP307-SS3-4 in Tables 2 and 3), and one set GP307-SS3-shingle that references the original shape up to the bolt failure (using the calibration for GP307-SS3-4 in Tables 2 and 3) and references the after reassembly shape for the final failure (using the calibration for GP307-SS3-4 after reassembly in Tables 2 and 3). A simple addition of the results is not possible, since the exact locations of the correlation points do not match for the two correlations performed for GP307-SS3-shingle.

Figure 34a and b show the initial shape of GP307-SS3-4 and GP307-SS3-shingle, respectively, at the start of the failure test under no load. Figure 34c shows the out-of-plane shape of GP307-SS3-shingle after reassembly at zero load. The location of Z = 0 mm was set using three points on the gusset plate similarly to that described above. After the rotation, GP307-SS3-4 and GP307-SS3-shingle have a slight saddle shape (Fig. 34a and b) with the Tension Diagonal and West Chord in the positive Z-direction and the Compression Diagonal shifted in the negative Z-direction. After reassembly, the shingle plate is at rest in a slightly different position and the overall shape is somewhat concave. Note that the ranges of the Z-position for the shingle plate in Fig. 34b and c are centered about the approximate thickness of the plate (9.53 mm or 3/8 inch). Figure 35 shows the evolution of the Z-direction displacement for GP307-SS3-4 from the initial shape in Fig. 34a. The ALF values are in regards to the Tension Diagonal load (Table 4). During the test, GP307-SS3-4 shifted toward the negative Z-direction from an early stage, with the exception of the Tension Diagonal which generally did not move out-of-plane (Fig. 35a–c). Figures 35a–c are from before the premature bolt failure, and only Fig. 35d is from after the reassembly. The displacements plotted in Fig. 35d are still in regards to the original shape shown in Fig. 34a, but after reassembly the connection was sitting in a position that was in the negative Z-direction from its original position (between W = -15 mm to -9 mm). Figure 35d shows that the plate finally buckled at the Compression Diagonal in the negative Z-direction. During the test, GP307-SS3-shingle also shifted toward the negative Z-direction from an early stage (Fig. 36a–c), until the premature bolt failure (Fig. 36d, when the plate unloaded and settled in the positive Z-direction). Figures 36a–c are from before

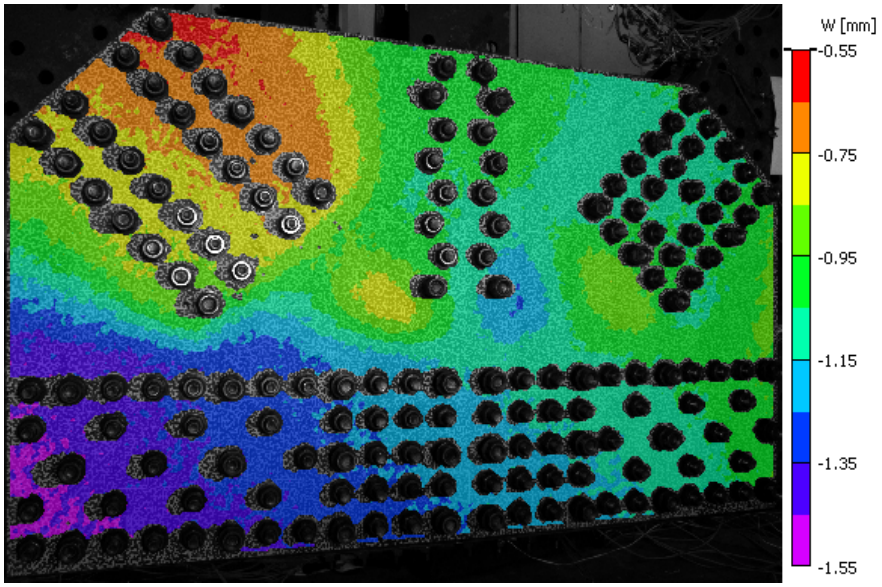

(a)

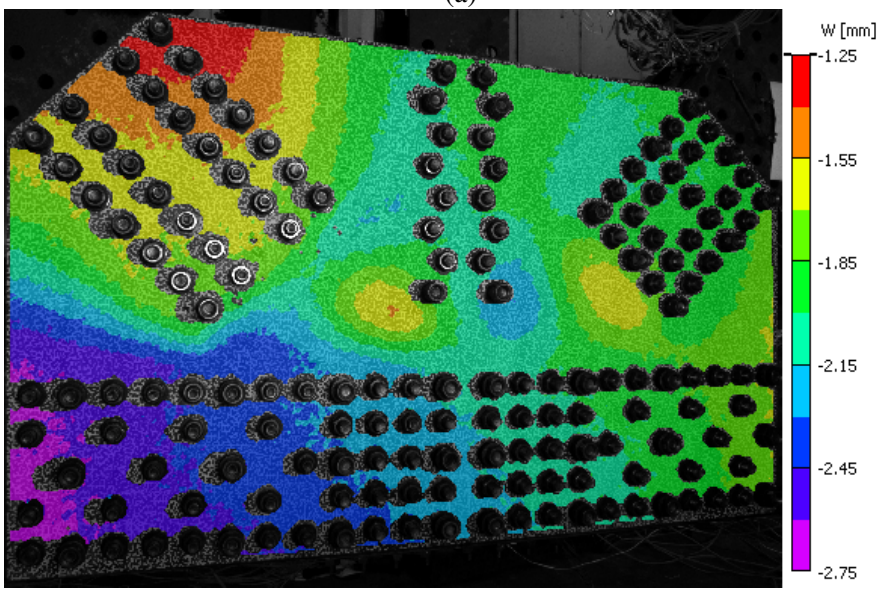

(b)

Figure 29: Out-of plane displacement (W) fields from the reference state to current plate shape for GP307-SS3-2 at ALF of (a) 0.23, (b) 0.36, (c) 0.57, and (d) 0.67 (failure).

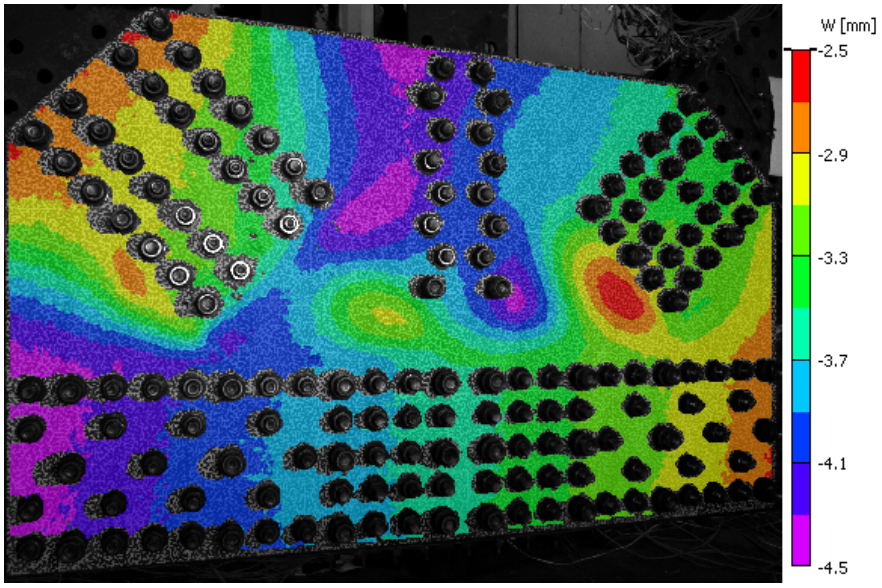

(c)

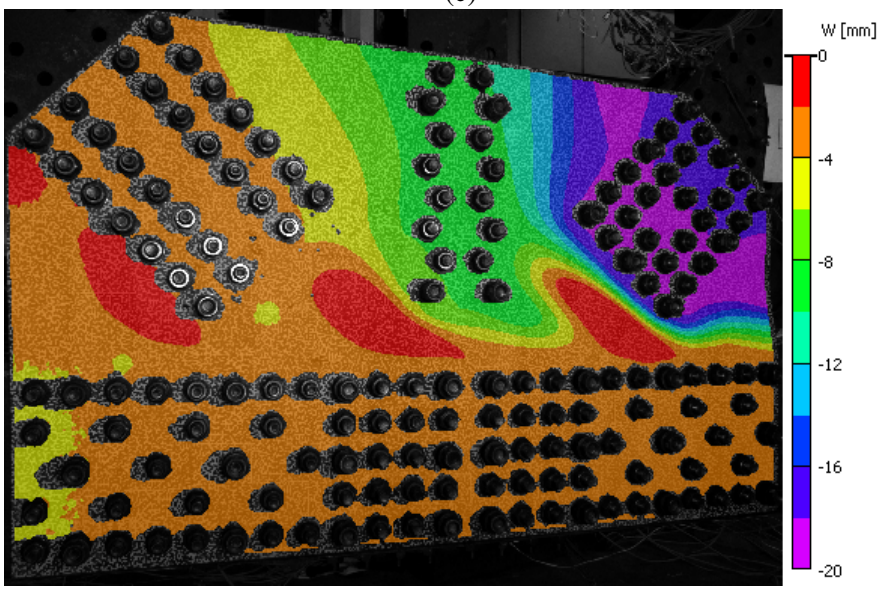

(d)

Figure 29 (continued)

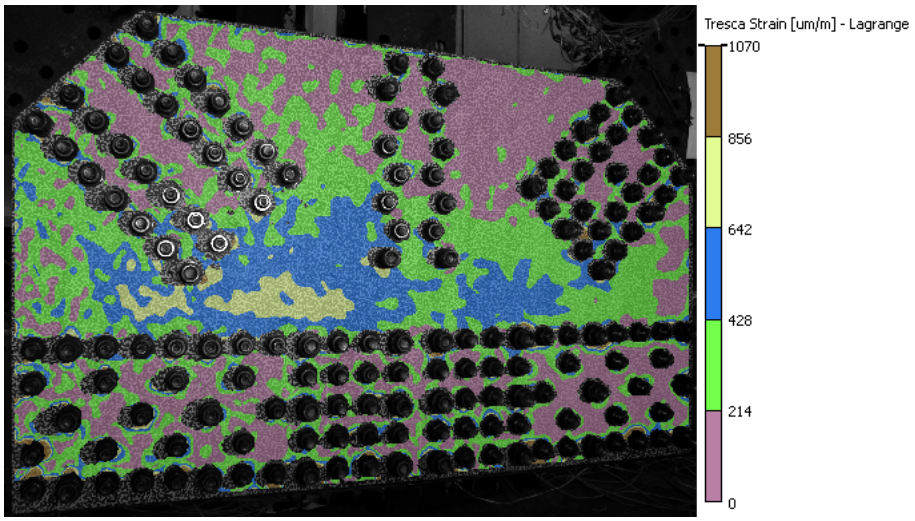

(a)

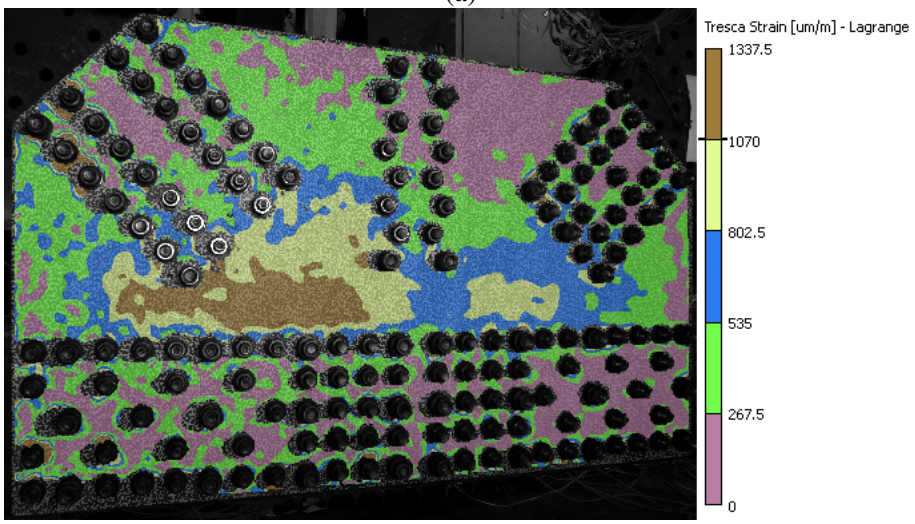

(b)

Figure 30: Maximum in-plane shear strain for GP307-SS3-2 at ALF of (a) 0.23, (b) 0.36, (c) 0.57, and (d) 0.67 (failure), with initial yield at 1070 μm/m.

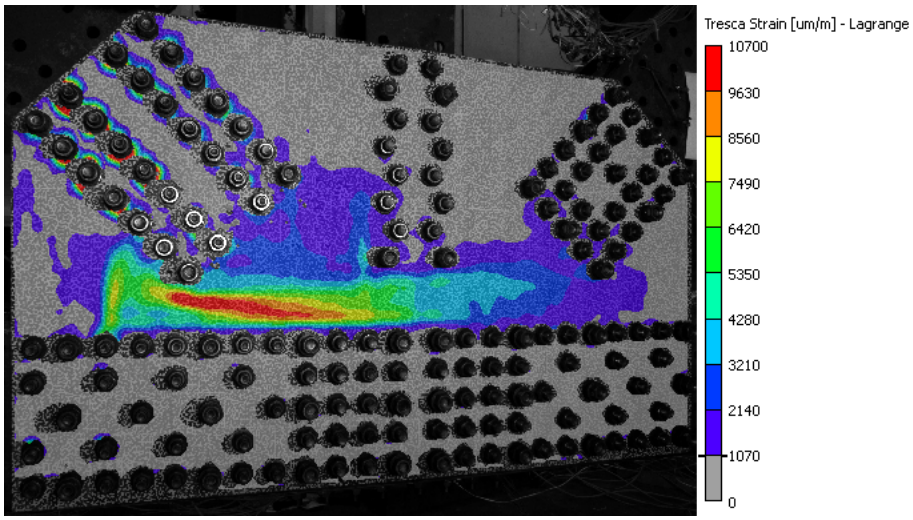

(c)

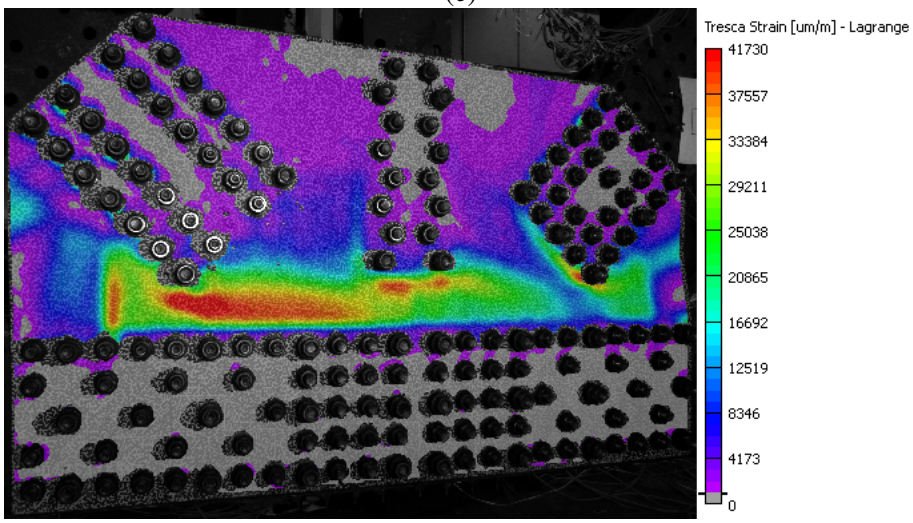

(d)

Figure 30 (continued)

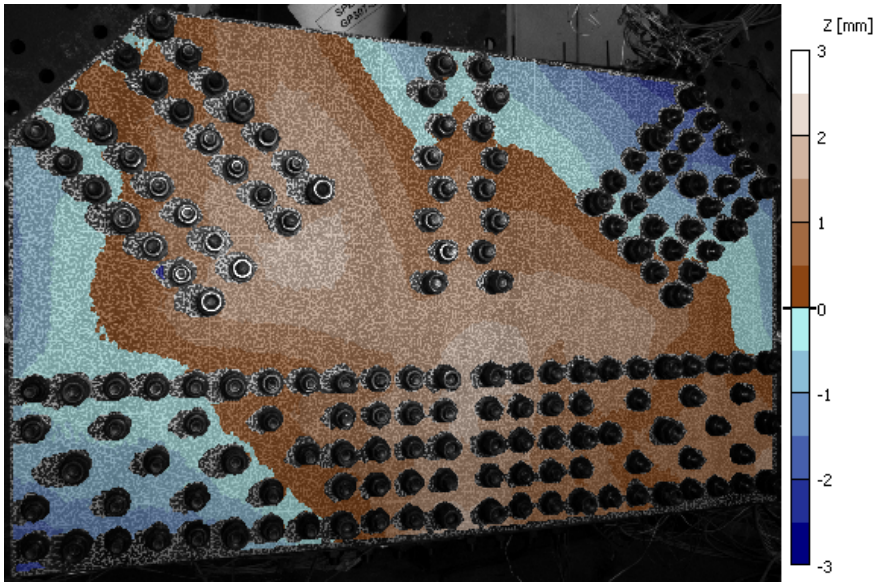

Figure 31: Out-of-plane shape of specimen GP307-SS3-3 at zero load (ALF = 0).

the premature bolt failure. Figure 36d is from just after the premature failure, after unloading, and only Fig. 36e is from after the reassembly. The displacements shown in Fig. 36a–d are in reference to the original shape shown in Fig. 34b, but the displacements shown in Fig. 36e are in reference to unloaded state after reassembly shown in Fig. 34c. Figure 36e also shows that the Compression Diagonal buckled in the negative Z-direction similar to Fig. 35d.

Figure 37 plots the maximum in-plane shear strains for the visible portion of GP307-SS3-4 at the same four ALF levels shown in Fig. 35. The yield strain in terms of Tresca strain is approximately 850 μm/m, based on standard material testing of the same GP307-SS3-4 material. Figures 37a and b have strain ranges predominately in the elastic range and use a pseudorandom color map. Figure 37c and d have strain ranges predominately in the plastic strain range (spectrum color map) with grey being used for areas of the plate that have not yet reached the yield strain. The results for GP307-SS3-4 show that the Tresca strains were concentrated near the thinned section (above the Chord bolt line) and along the Tension bolt lines prior to the premature bolt failure (Fig. 37a–c). After reassembly and at maximum load (ALF = 0.99), the strains along the Tension bolt lines are reduced as compared to the strains near the thinned section (Fig. 37d).

Figure 38 plots the maximum in-plane shear strains for GP307-SS3-shingle at the same four ALF levels shown in Fig. 36. The initial yield strain in terms of Tresca strain is approximately 1040 μm/m, based on standard material testing of the same GP307-SS3-shingle material. Figures 38a and b have strain ranges predominately in the elastic range and use a pseudorandom color map. Figure 38c–e have strain ranges predominately in the plastic strain range (spectrum color map) with grey being used for areas of the plate below the yield strain of 1040 μm/m. The results

for GP307-SS3-shingle show that the Tresca strains were concentrated near the bolts prior to, and just after, the premature bolt failure (Fig. 38a–d). The strains shown in Fig. 38e are in reference to the reassembled connection, thus the area in grey does not delineate areas of strain below yield, but does describe areas that have not exceeded 1040 μm/m since reassembly. The total strain would be the addition of these strains to the unloaded state just after the premature bolt failure (Fig. 38d). The strains at failure (Fig. 38e) show similar strain localization to earlier gusset plates, with the highest strains along the Chord bolt lines and between the Tension and Compression Diagonal bolt lines (through the end of the Vertical bolt line). Also similar to the earlier gusset plate tests, these two bands of highest strain are connected by many lower magnitude strain bands.

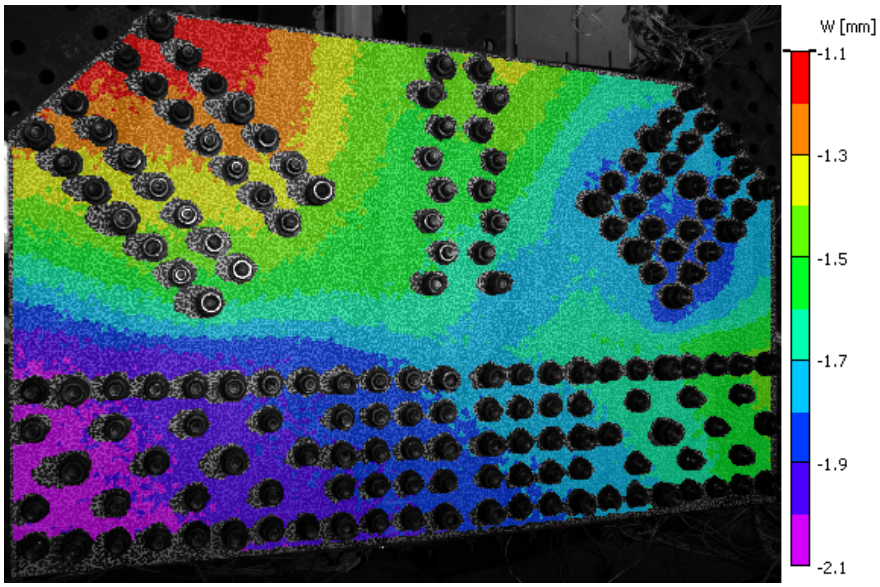

(a)

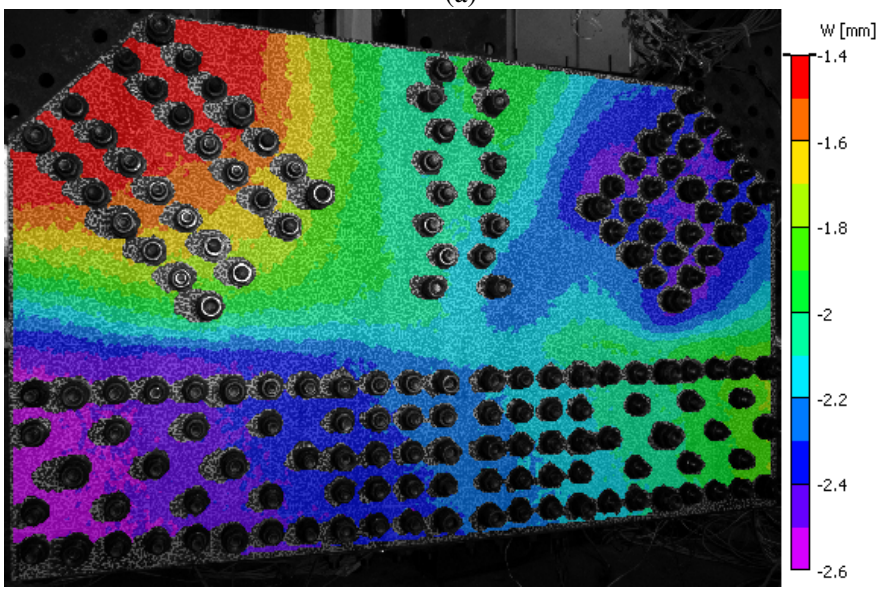

(b)

Figure 32: Out-of plane displacement (W) fields from the reference state to current plate shape for GP307-SS3-3 at ALF of (a) 0.24, (b) 0.30, (c) 0.63, and (d) 0.74 (failure).

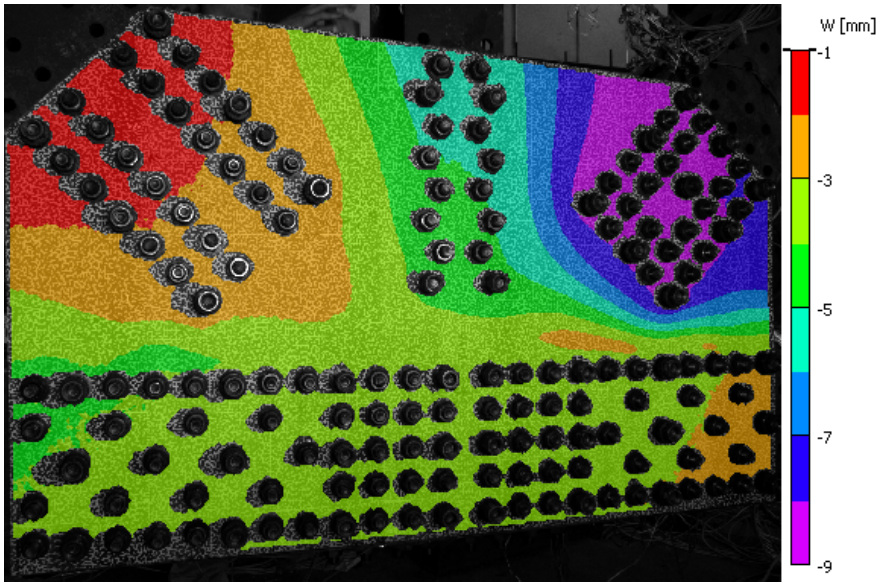

(c)

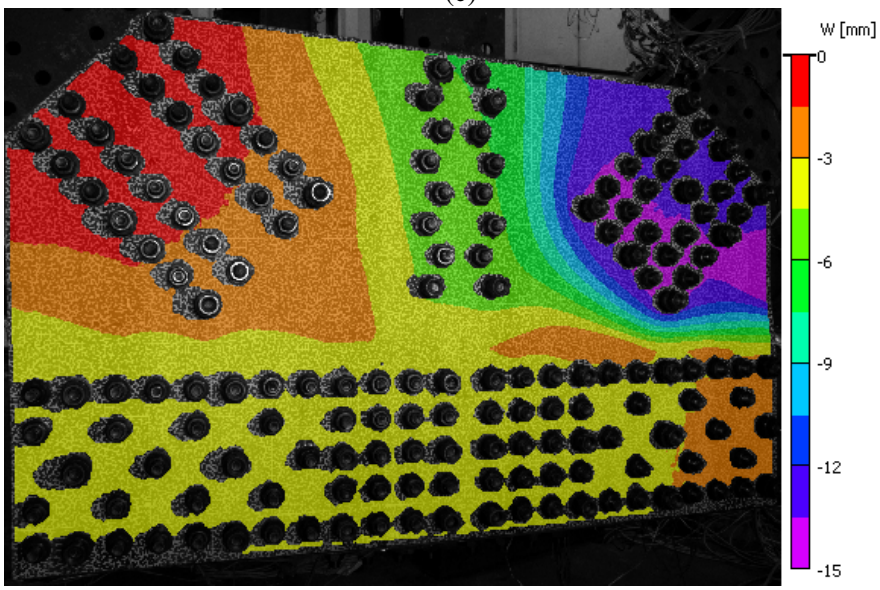

(d)

Figure 32 (continued)

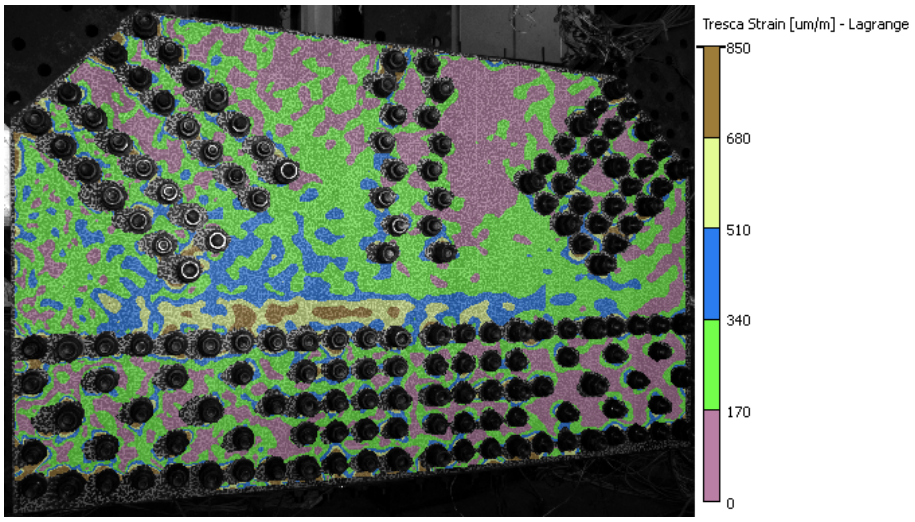

(a)

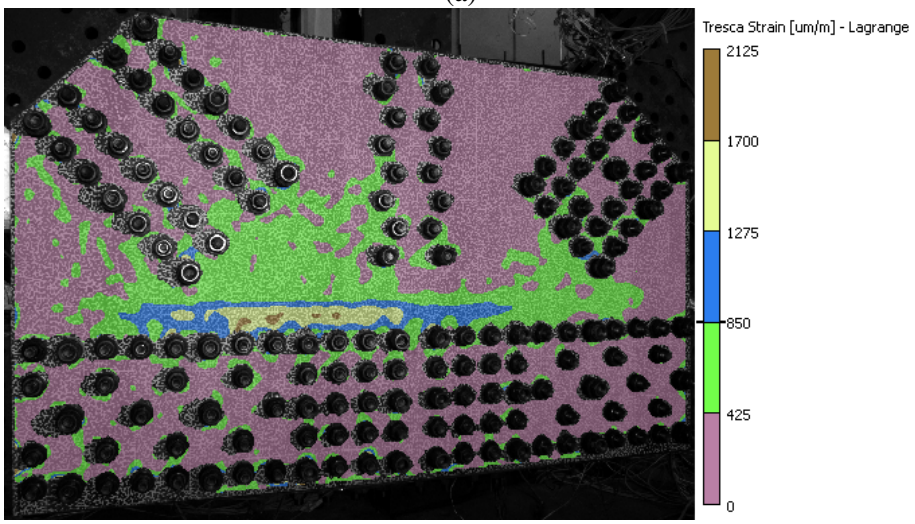

(b)

Figure 33: Maximum in-plane shear strain for GP307-SS3-3 at ALF of (a) 0.24, (b) 0.30, (c) 0.63, and (d) 0.74 (failure), with initial yield at 850 μm/m.

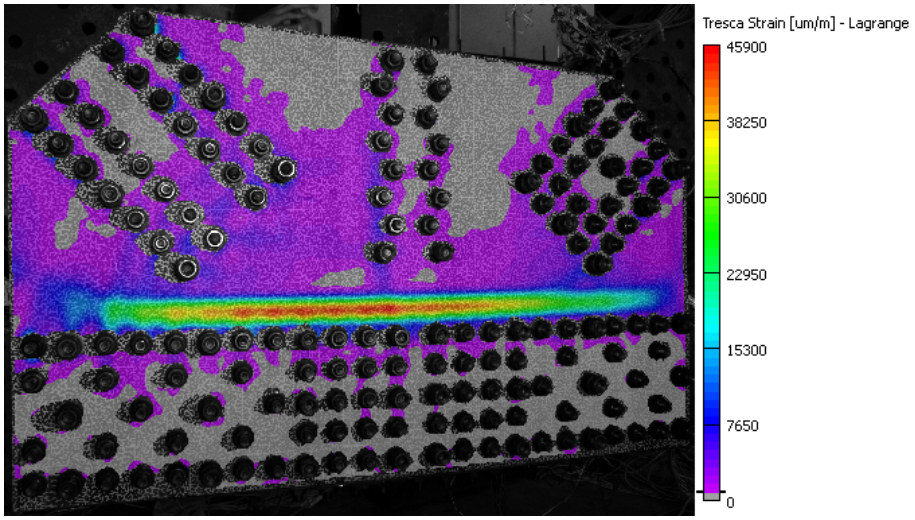

(c)

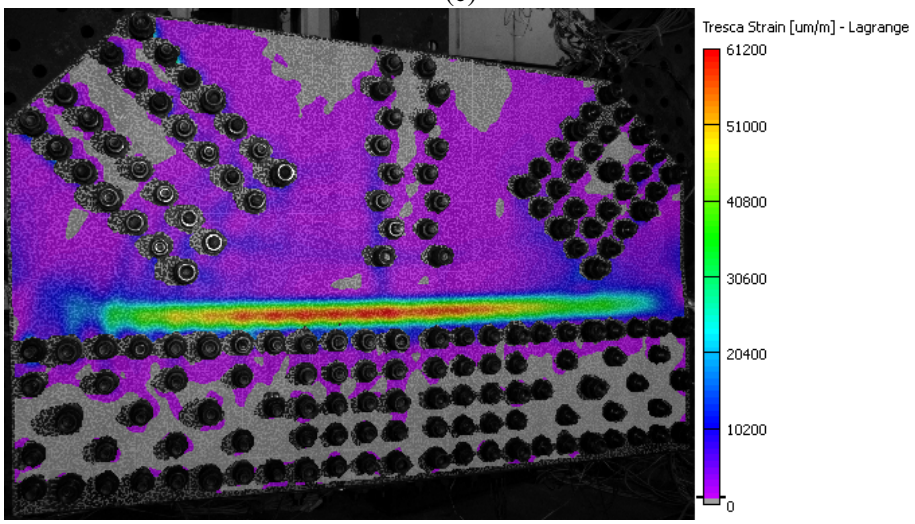

(d)

Figure 33 (continued)

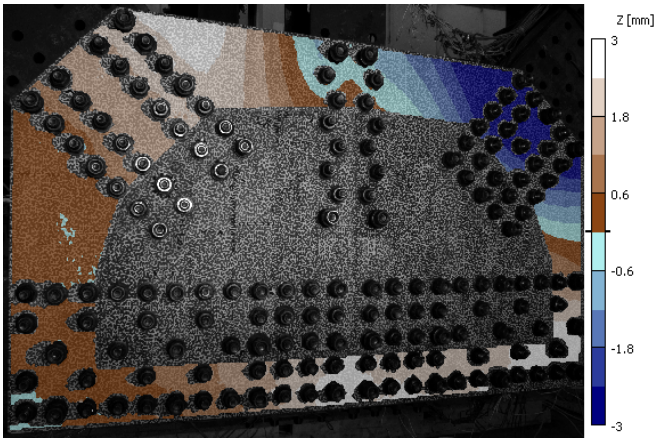

(a)

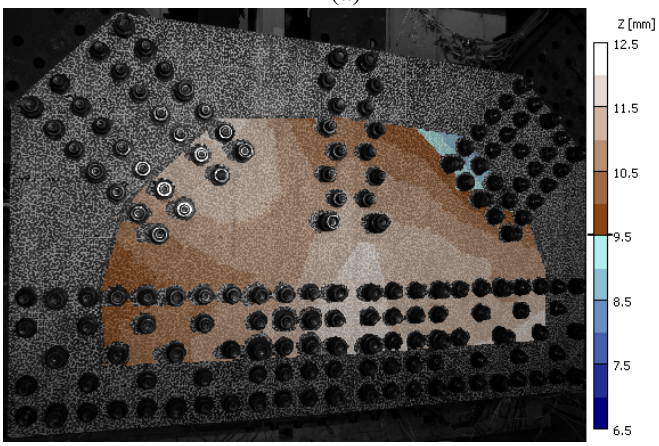

(b)

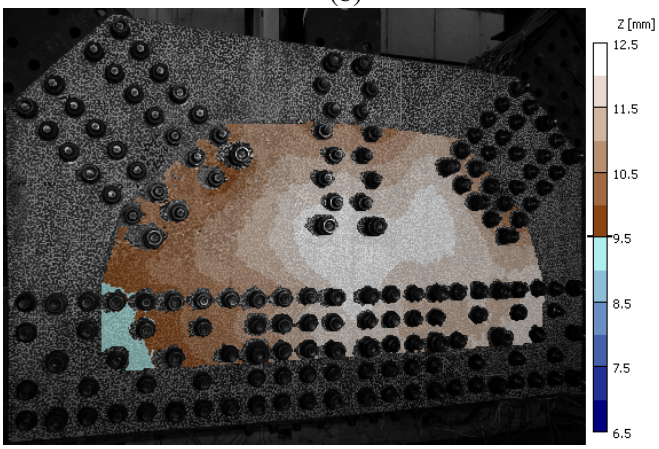

(c)

Figure 34: Out-of-plane shape at zero load of specimen (a) GP307-SS3-4 before the start of testing, (b) GP307-SS3-shingle plate before the start of testing, and (c) GP307-SS3-shingle plate after premature bolt failure and reassembly.

7.2.9 GP490-SS3

Figure 39 shows the initial shape of GP490-SS3 at the start of the failure test under no load. The location of Z = 0 mm was set using three points as described above. After the rotation, the plate is slightly concave about the ends of the two chord members. Figure 40 shows the evolution of the Z-direction displacement from the initial shape in Fig. 39. The ALF values are in regards to the Compression Diagonal load (Table 4). During the test, the entire plate shifted toward the negative Z-direction from an early stage, with final buckling of the Compression diagonal in that direction (Fig. 40d). Figure 41 plots the maximum in-plane shear strains at the same four ALF levels shown in Fig. 40. The yield strain in terms of Tresca strain is approximately 1040 μm/m, based on standard material testing of the same material. Figures 41a–c have strain ranges predominately in the elastic range and use a pseudorandom color map. Figure 41d has a strain range predominately in the plastic strain range (spectrum color map) with grey being used for areas of the plate that have not yet reached the yield strain. The results show that the Tresca strains were concentrated between the ends of the Compression and Tension Diagonals from the early stages of loading, with slightly larger strains occurring at the end of the Compression Diagonal and along the Chord bolt lines. The strain field is more uniform in the early stages of loading, but the last stage (ALF = 0.73) shows substantial strain localization, along the Chord bolt lines. Additional strain localizations of lower magnitude extends from the Compression bolt line to the Tension bolt line with small extensions to the Chord bolt lines and the Vertical bolts.

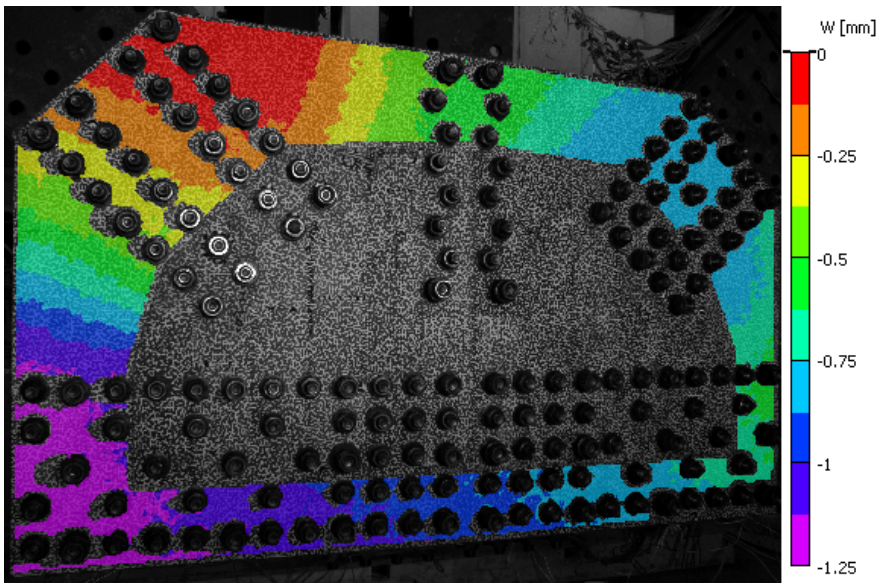

(a)

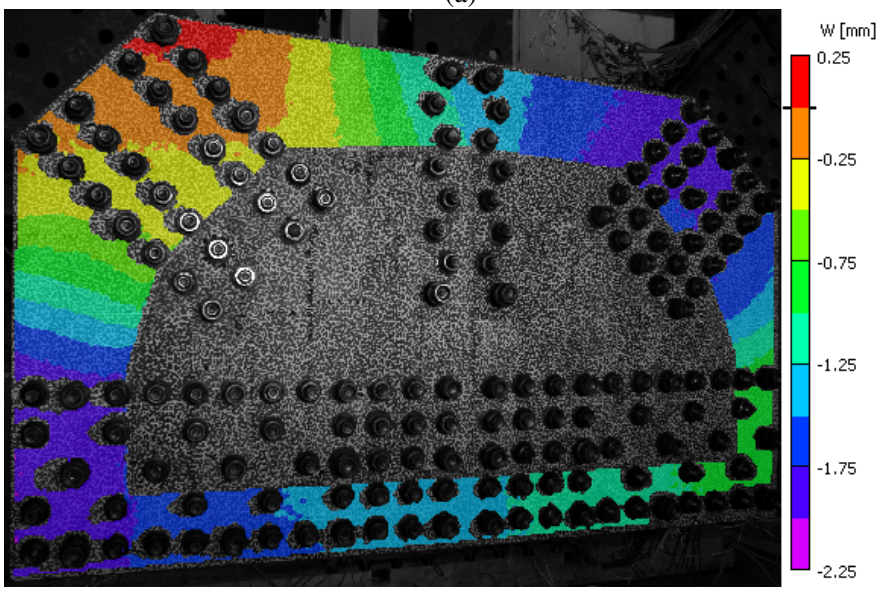

(b)

Figure 35: Out-of plane displacement (W) fields from the reference state to current plate shape for GP307-SS3-4 at ALF of (a) 0.27, (b) 0.54, (c) 0.89, and (d) 0.99 (after premature bolt failure and reassembly).

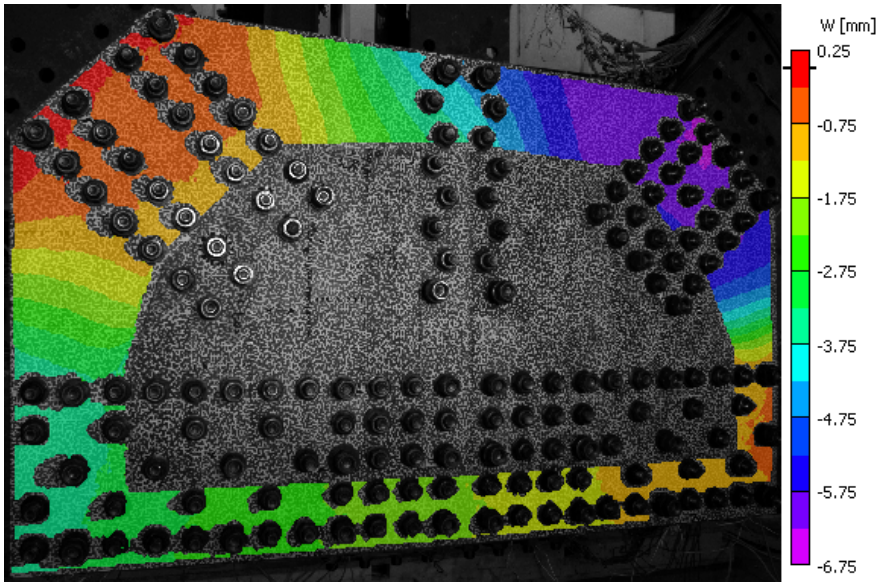

(c)

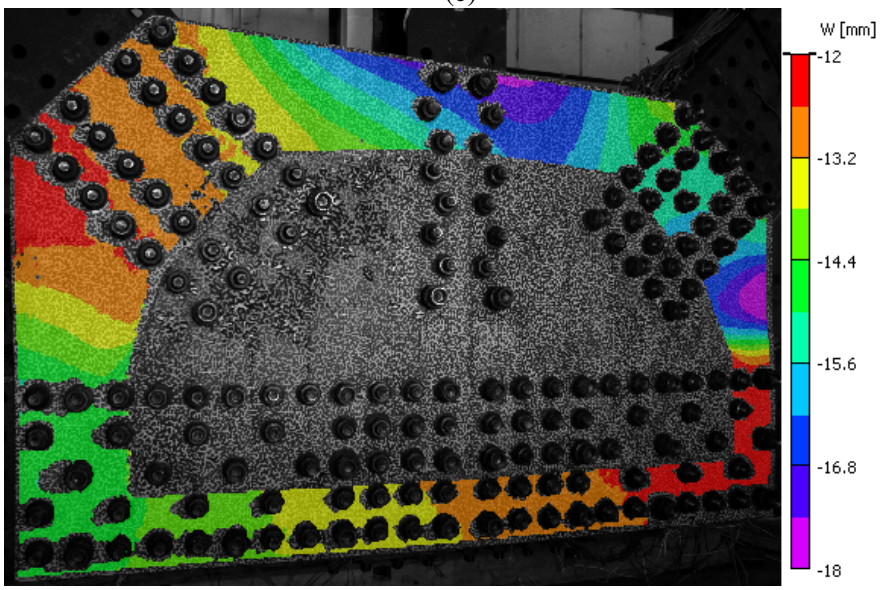

(d)

Figure 35 (continued)

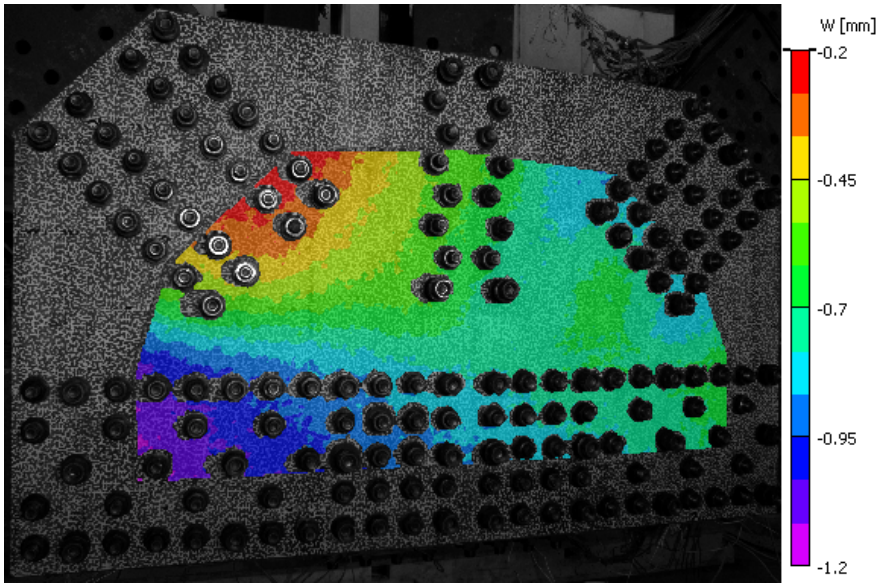

(a)

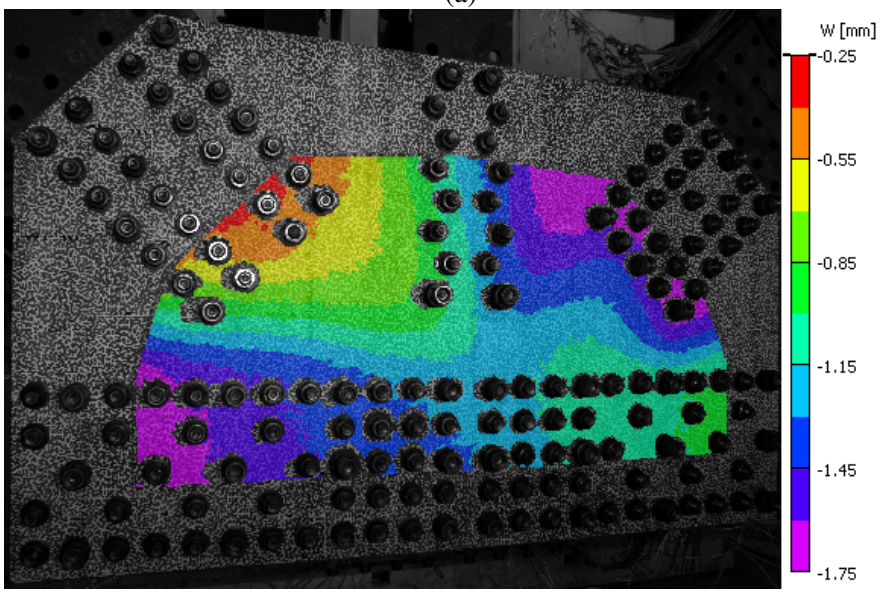

(b)

Figure 36: Out-of plane displacement (W) fields from the reference to current plate shape for GP307-SS3-shingle at ALF of (a) 0.27, (b) 0.54, (c) 0.89, (d) after unload from ALF = 0.89, and (e) 0.99 with W referenced to the unloaded position after reassembly (Fig. 134c).

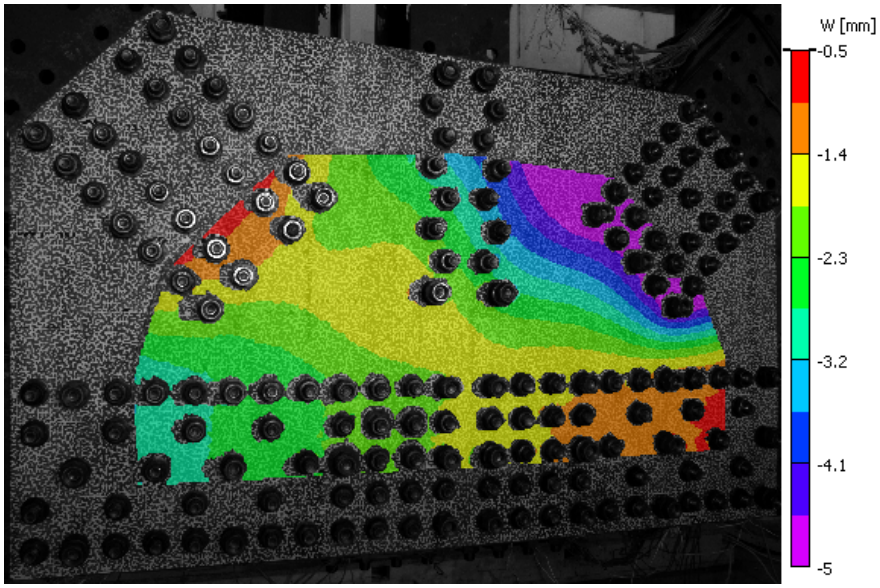

(c)

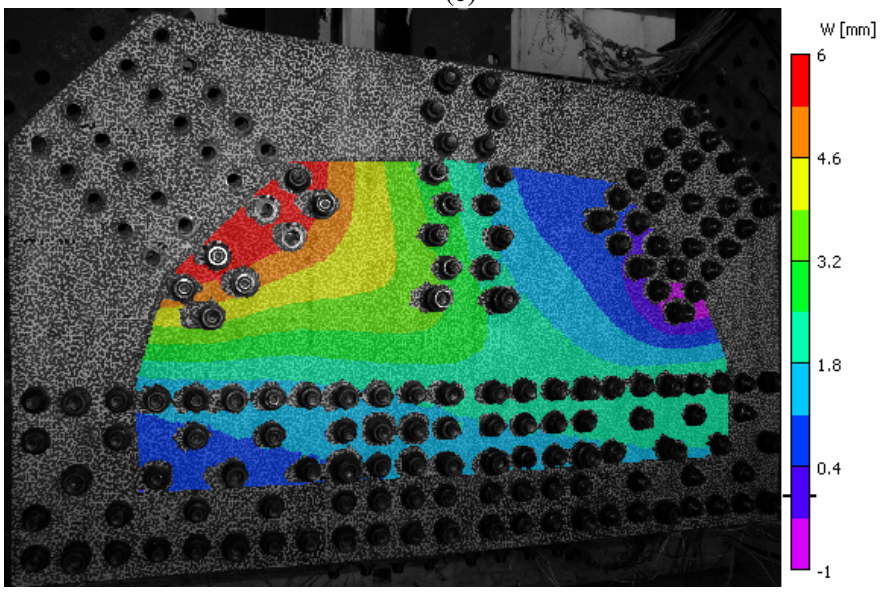

(d)

Figure 36 (continued)

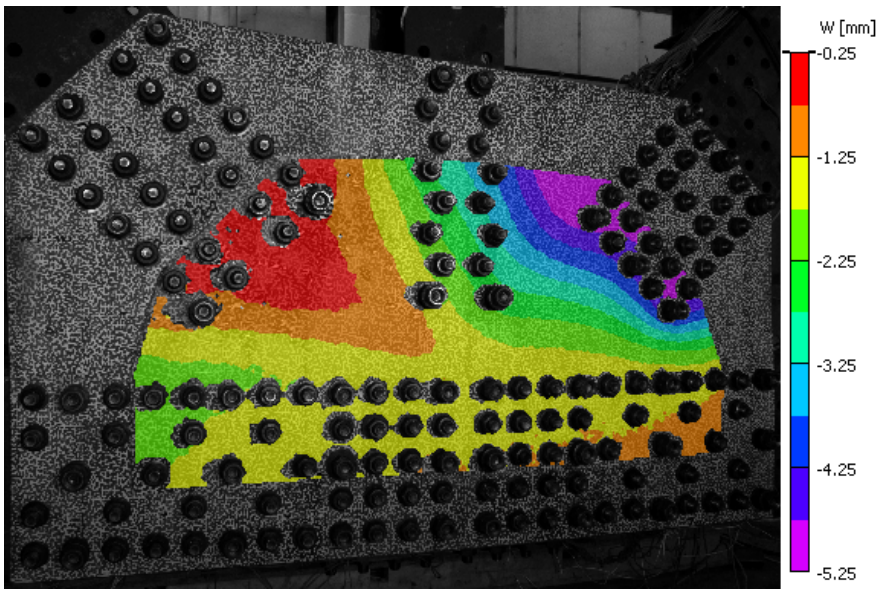

(e)

Figure 36 (continued)

7.2.10 GP490-SS3-1

Figure 42 shows the initial shape of GP490-SS3-1 at the start of the failure test under no load, after rotating to the selected coordinate system. After that rotation, the plate is relatively flat with a slight depression near the East Chord bolt line, and a slight twist along the West edge of the plate. Figure 43 shows the evolution of the Z-direction displacement from the initial shape in Fig. 42. The ALF values are in regards to the Tension Diagonal load (Table 4). During the test, the entire plate shifted toward the negative Z-direction from an early stage, through the final buckling of the Compression Diagonal in the negative Z-direction with a convex bulge of the plate under the Compression Diagonal (Fig. 43d). Figure 44 plots the maximum in-plane shear strains at the same four ALF levels shown in Fig. 43. The yield strain in terms of Tresca strain is approximately 1030 μm/m, based on standard material testing of the same material. Figures 44a–c have strain ranges predominately in the elastic range and use a pseudorandom color map. Figure 44d has a strain range predominately in the plastic strain range (spectrum color map) with grey being used for areas of the plate that have not yet reached yield. The results show that the Tresca strains were concentrated between the ends of the Compression and Tension Diagonals from the early stages of loading, with the largest strains occurring at the end of the Tension Diagonal and along the Chord bolt lines. The strain field is more diffuse in the early stages of loading (Fig. 44a and b), then the later two stages (Fig. 44c and d) which show more strain localizations. These long localized bands extend along the Chord bolt line and from the bolt lines of the diagonals to one another, with added bands of high strain reaching from the chord band to the other long band between the diagonals. This is similar to Figure 41d for GP490-SS3, but the magnitude of strain is much higher in Fig. 44d and more weighted to the Tension Diagonal half of the plate.

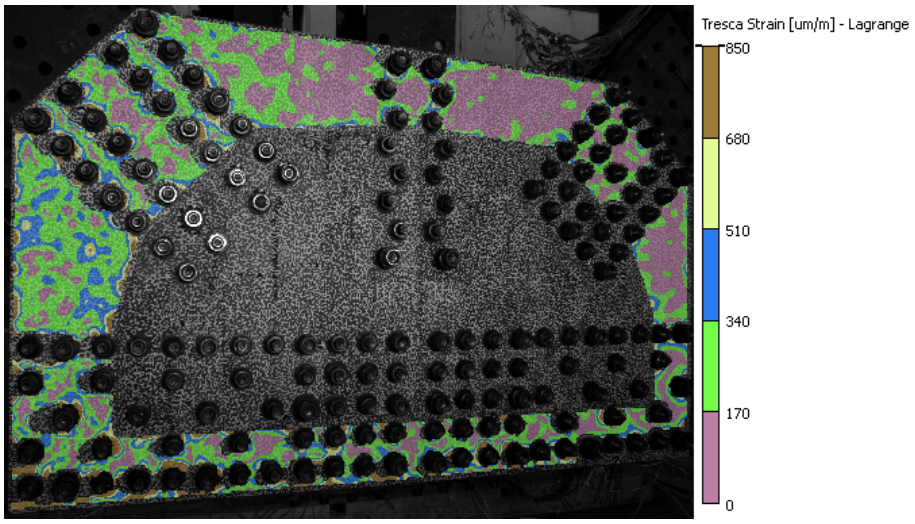

(a)

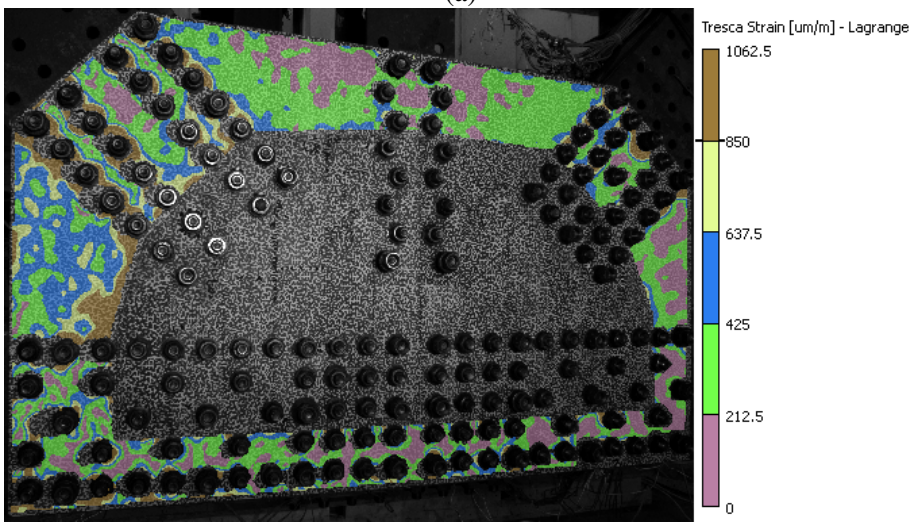

(b)

Figure 37: Maximum in-plane shear strain for GP307-SS3-4 at ALF of (a) 0.27, (b) 0.54, (c) 0.89, and (d) 0.99 (failure), with initial yield at 850 μm/m.

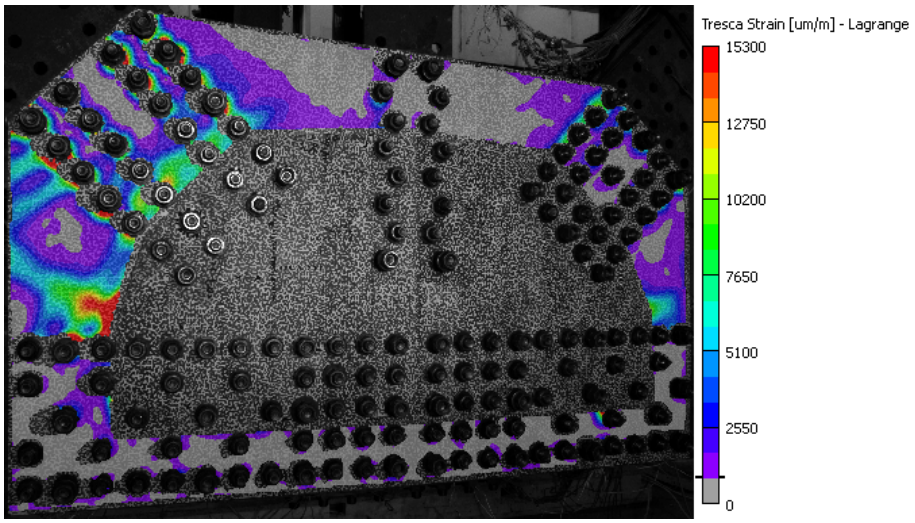

(c)

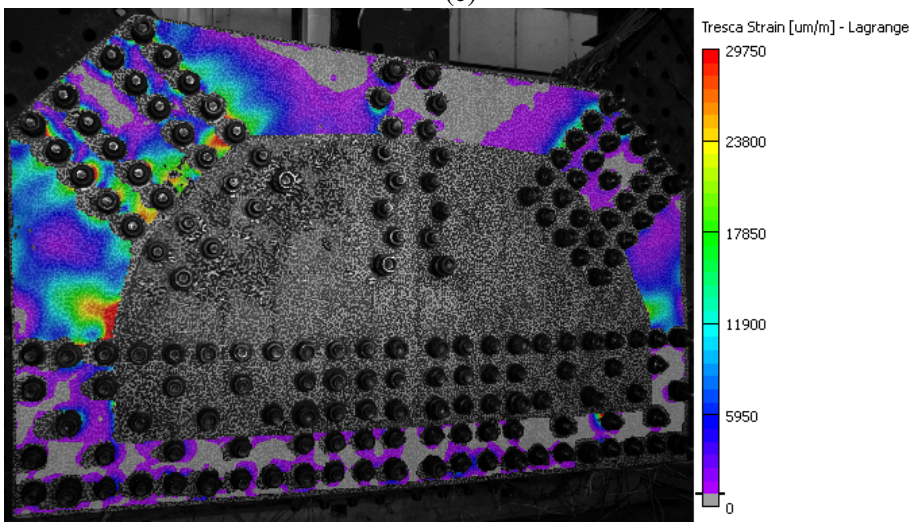

(d)

Figure 37 (continued)

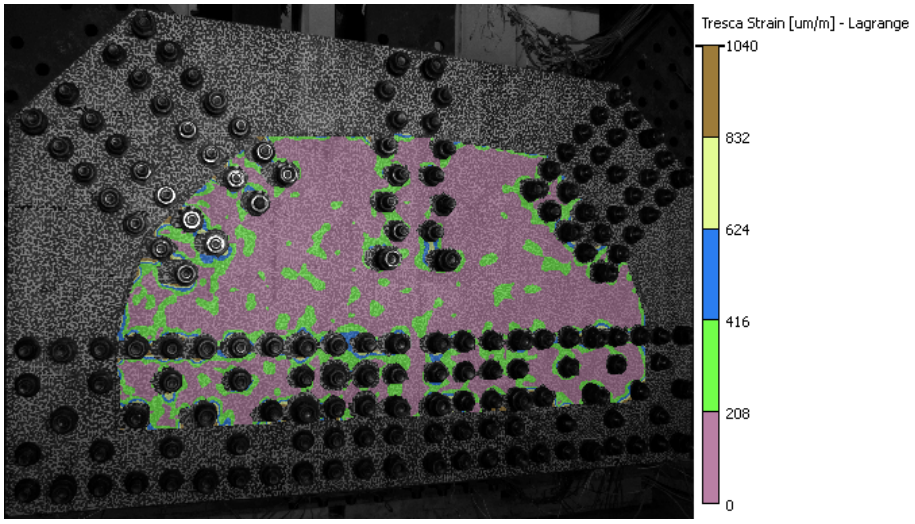

(a)

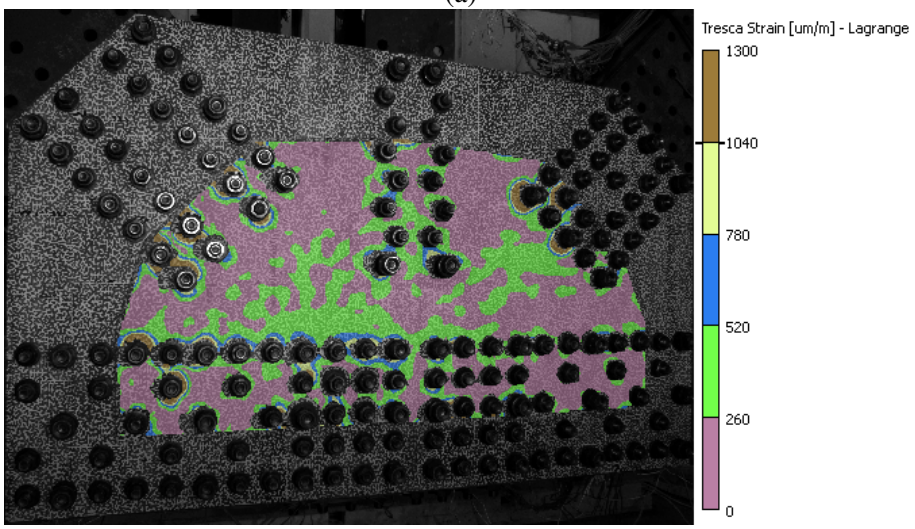

(b)

Figure 38: Maximum in-plane shear strain for GP307-SS3-shingle at ALF of (a) 0.27, (b) 0.54, (c) 0.89, (d) after unload from ALF = 0.89, and (e) at ALF = 0.99 after reassembly where Tresca strain values are in addition to the strains shown in (d). Initial material yield strain is at 1040 μm/m.

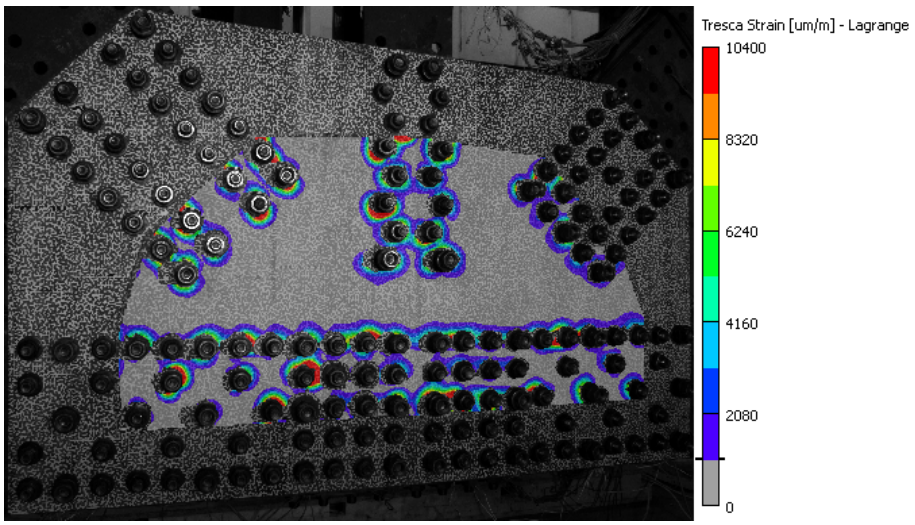

(c)

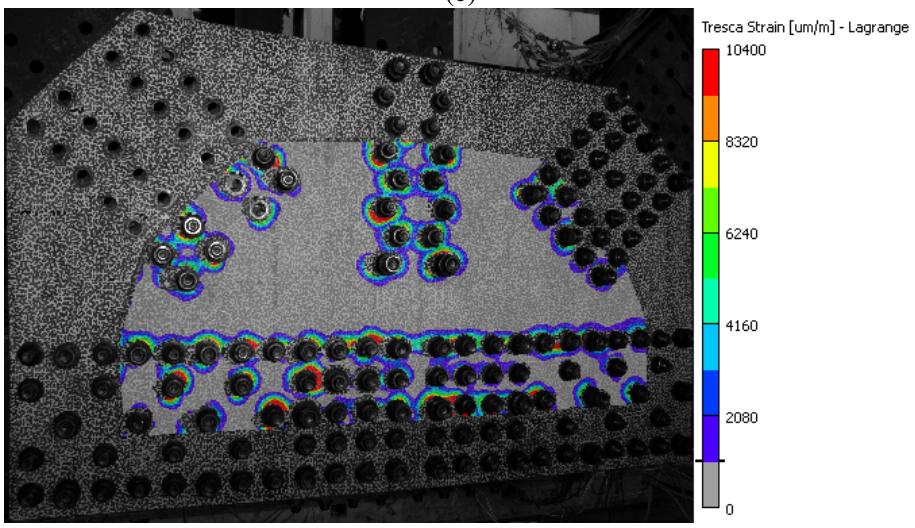

(d)

Figure 38 (continued)

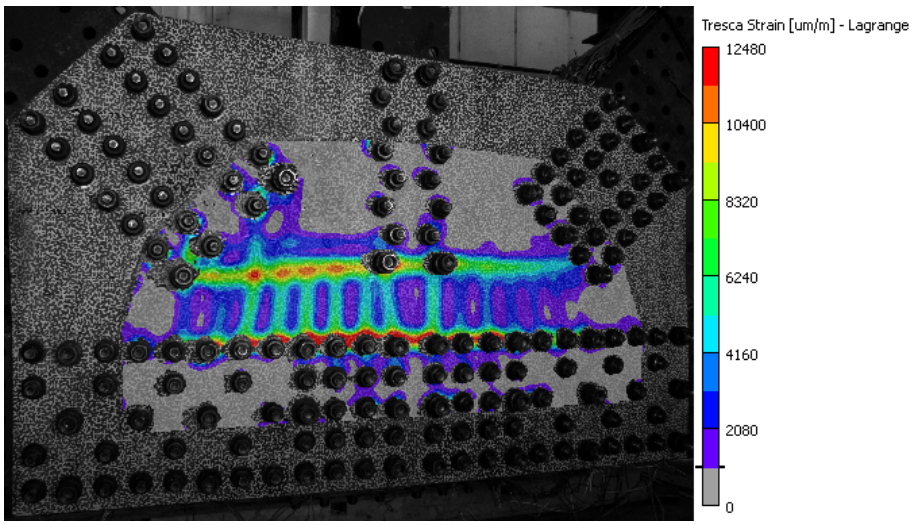

(e)

Figure 38 (continued)

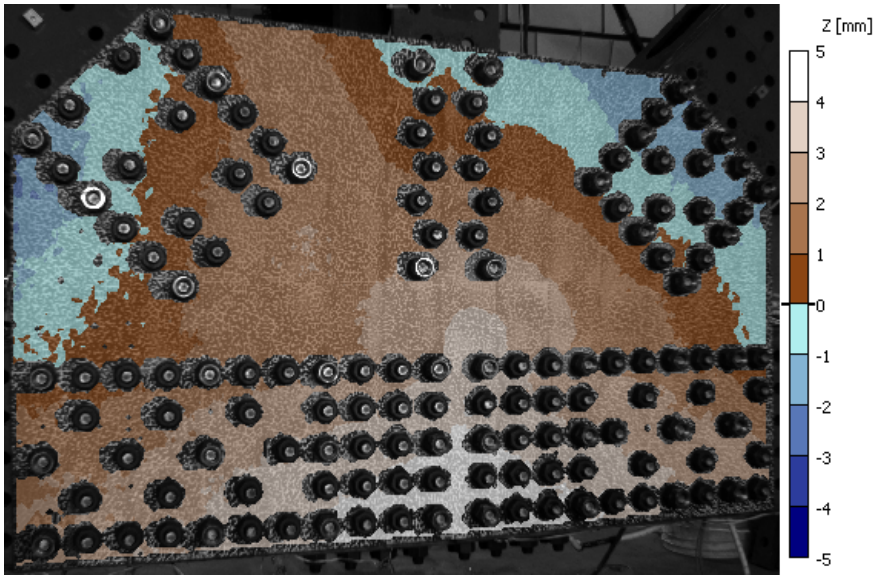

Figure 39: Out-of-plane shape of specimen GP490-SS3 at zero load (ALF = 0).

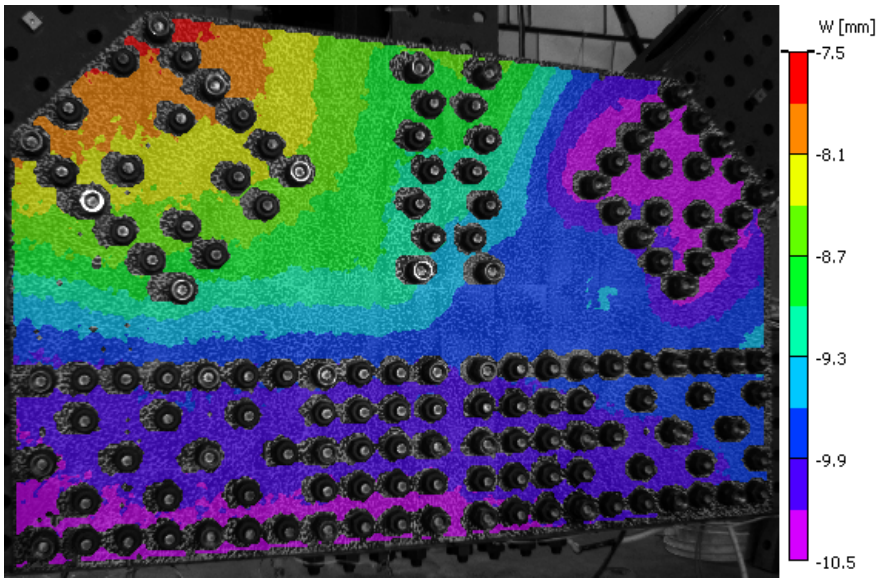

(a)

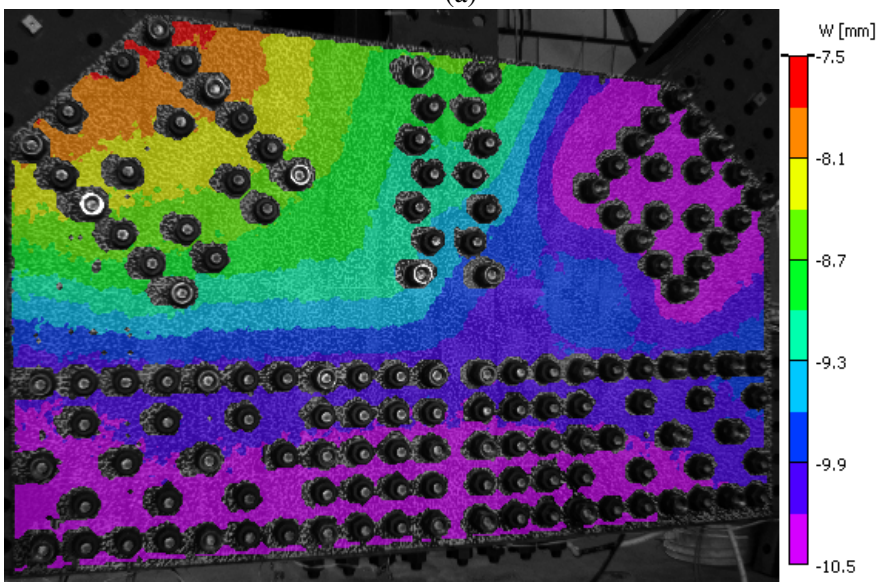

(b)

Figure 40: Out-of plane displacement (W) fields from the reference state to current plate shape for GP490-SS3 at ALF of (a) 0.59, (b) 0.61, (c) 0.63, and (d) 0.73 (failure).

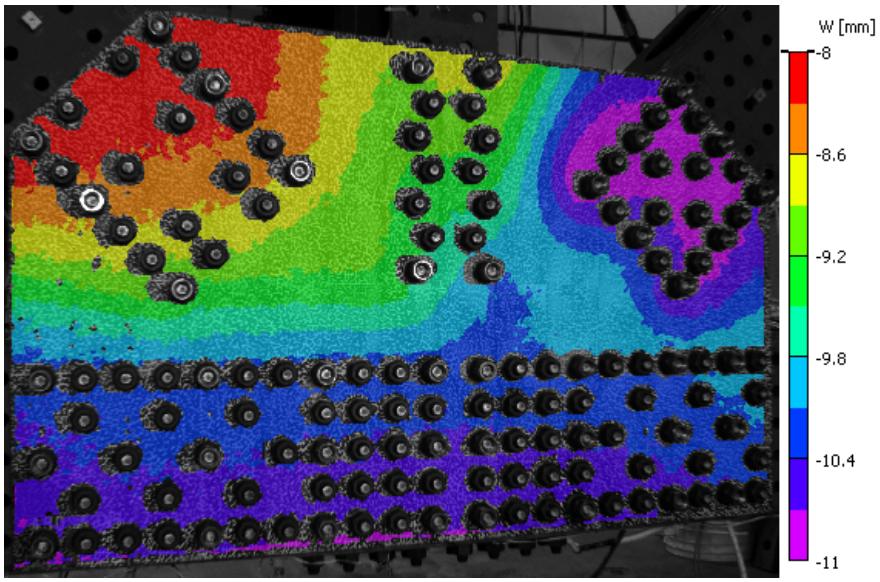

(c)

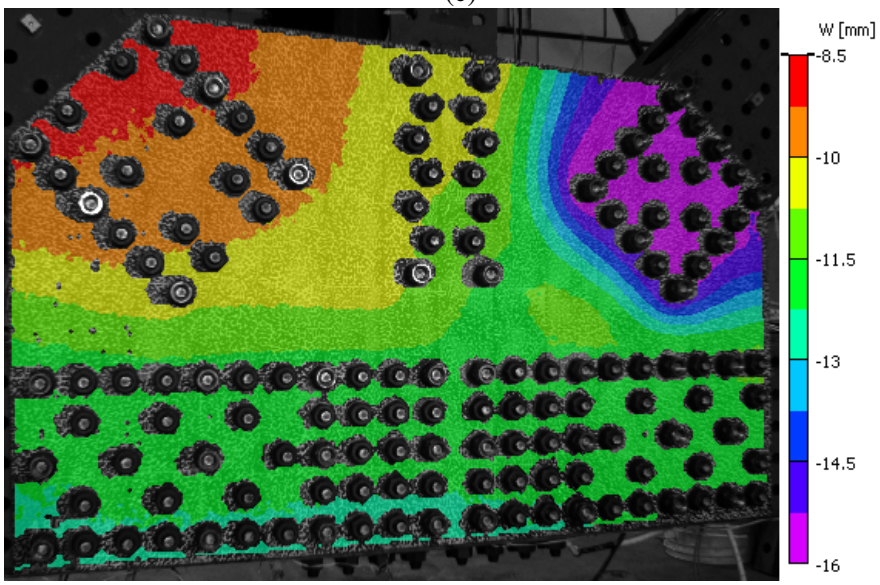

(d)

Figure 40 (continued)

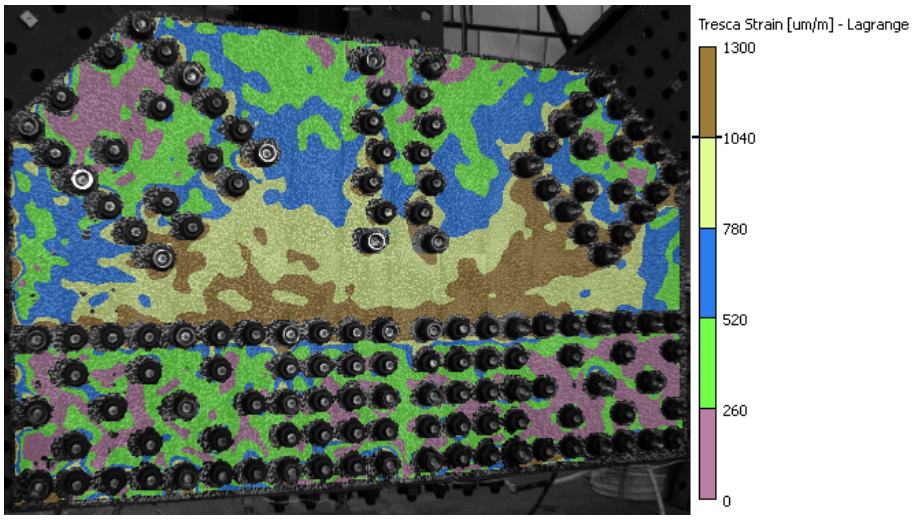

(a)

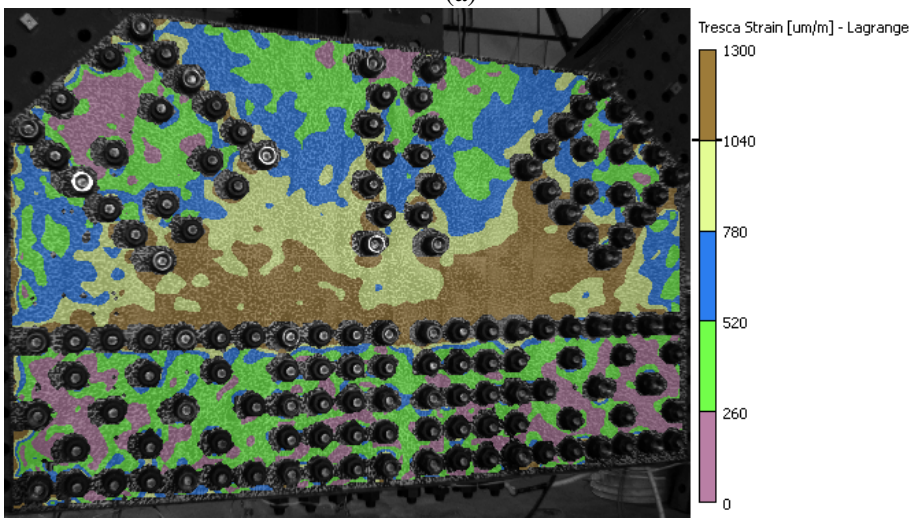

(b)

Figure 41: Maximum in-plane shear strain for GP490-SS3 at ALF of (a) 0.59, (b) 0.61, (c) 0.63, and (d) 0.73 (failure), with initial yield at 1040 μm/m.

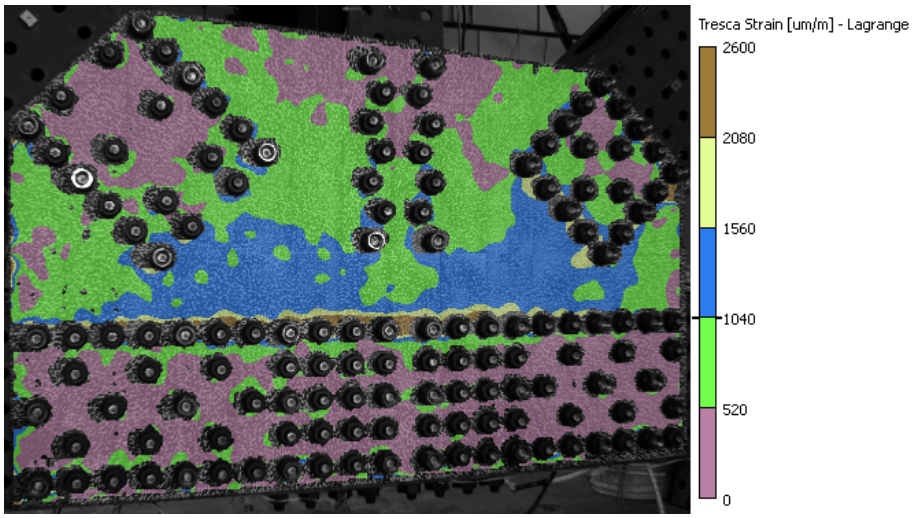

(c)

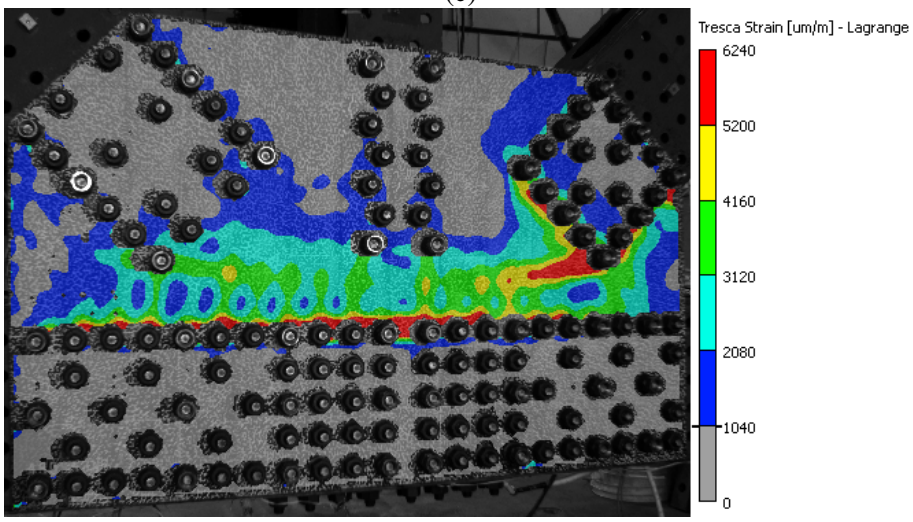

(d)

Figure 41 (continued)

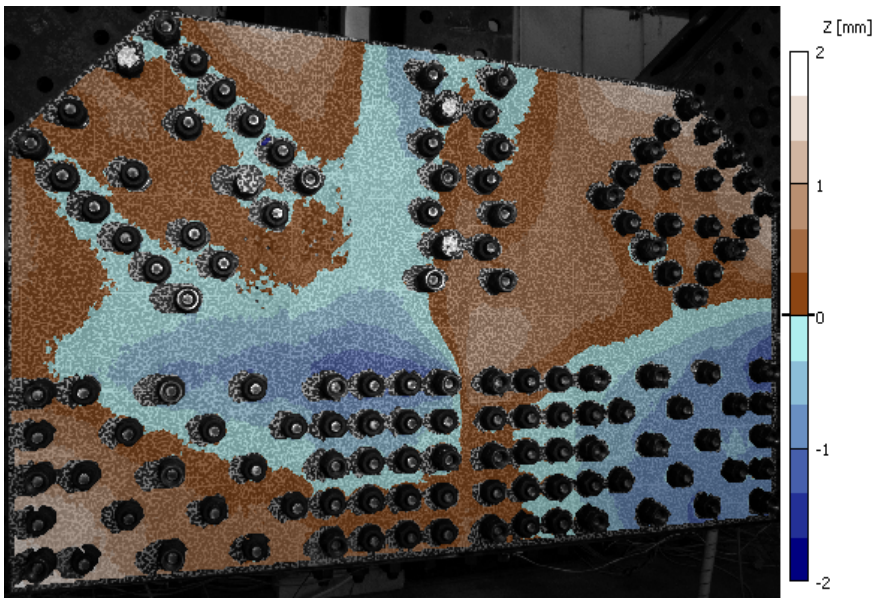

Figure 42: Out-of-plane shape of specimen GP490-SS3-1 at zero load (ALF = 0).

7.2.11 GP490-LS3-1

Figure 45 shows the initial shape of GP490-LS3-1 at the start of the failure test under no load. The location of Z = 0 mm was set using three points as described above. After the rotation, the plate has a slight saddle shape with the Tension Diagonal and West Chord in the positive Z-direction and the Compression Diagonal and East Chord in the negative Z-direction. Figure 46 shows the evolution of the Z-direction displacement from the initial shape in Fig. 45. The ALF values are in regards to the Tension Diagonal load (Table 4). During the test, the entire plate shifted toward the negative Z-direction from an early stage, until the final buckling of the Compression diagonal in the positive Z-direction (Fig. 46d). Figure 47 plots the maximum in-plane shear strains at the same four ALF levels shown in Fig. 46. The yield strain in terms of Tresca strain is approximately 1040 μm/m, based on standard material testing of the same material. Figures 47a–c have strain ranges predominately in the elastic range and use a pseudorandom color map. Figure 47d has a strain range predominately in the plastic strain range (spectrum color map) with grey being used for areas of the plate that have not yet reached the yield strain. The results show that the Tresca strains were concentrated between the ends of the Tension and Compression Diagonals from the early stages of loading, with the largest strains occurring at the end of the Tension Diagonal and along the Chord bolt lines. The strain field is more diffuse in the early stages of loading (Fig. 47a and b). In the later stages (Fig. 47c and d) more strain localizations are present. These begin by ALF = 0.68 (in Fig. 47c) extending from the Tension Diagonal bolt line to the Vertical bolt line, and later (in Fig. 47d) extending between the Tension and Compression Diagonal bolt lines though the end of the Vertical bolt line with various extensions down to the Chord bolt lines.

Attempts were made to apply a brittle coating to the outside face of the South gusset plate with limited success. In many cases, the coating did not flake off as intended even at the maximum strains achieved during the tests to failure. One of the tests where the coating was successful was for GP490-LS3-1. Figures 48 and 49 show the brittle coating results on the South face of the connection compared to the Tresca strains on the North face. In both figures, the brittle coating results for the South face are mirror images of the South plate, thus the Tension Diagonal is on the upper left and the Compression Diagonal is on the upper right. Also in both figures, the first image is of the brittle coating before testing began at zero load (ALF = 0). The second image in each figure is the brittle coating after the specified amount of loading in terms of ALF. The brittle coating was not calibrated so the strain level to cause flaking is not known quantitatively, but in the images the results of straining is a change from an initial grey or black color to a white in specific areas. For example, the distinct thin bands of white under the Tension Diagonal in Fig. 48a that do not appear in Fig. 48b. The third plot in each figure is a plot of the Tresca strain where the plastic strain range is shown in color and the strains below the expected yield for the material (1030 μm/m) is shown in grey. When comparing the results for the brittle coating and the DIC measurements two details should be kept in mind: (1) the brittle coating and DIC measurements are made on two different sides of the connection, and although the connection is designed as symmetric the out of plane motion (Fig. 46) could suggest some bending thus creating a difference in strain from the South to the North plate; (2) the spatial resolution of the strain system is on the order of the DIC

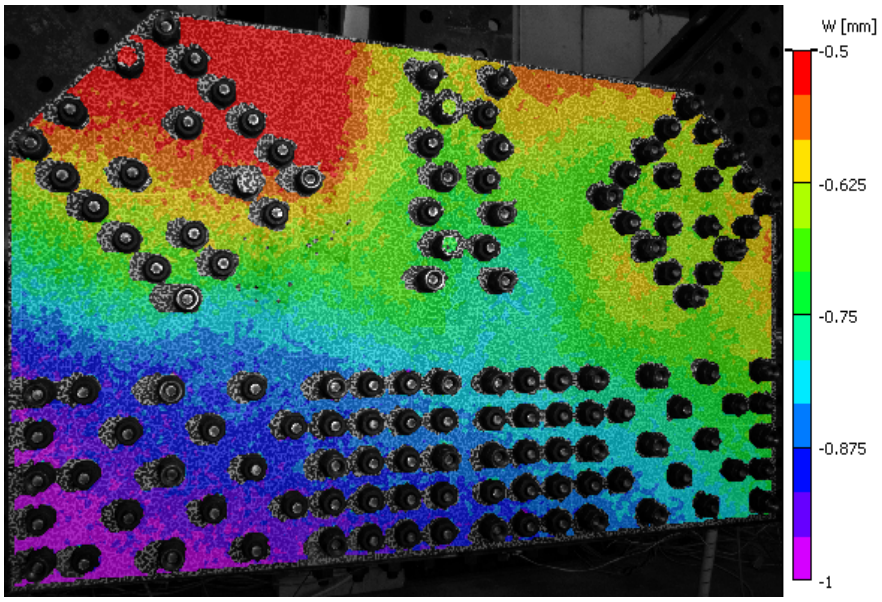

(a)

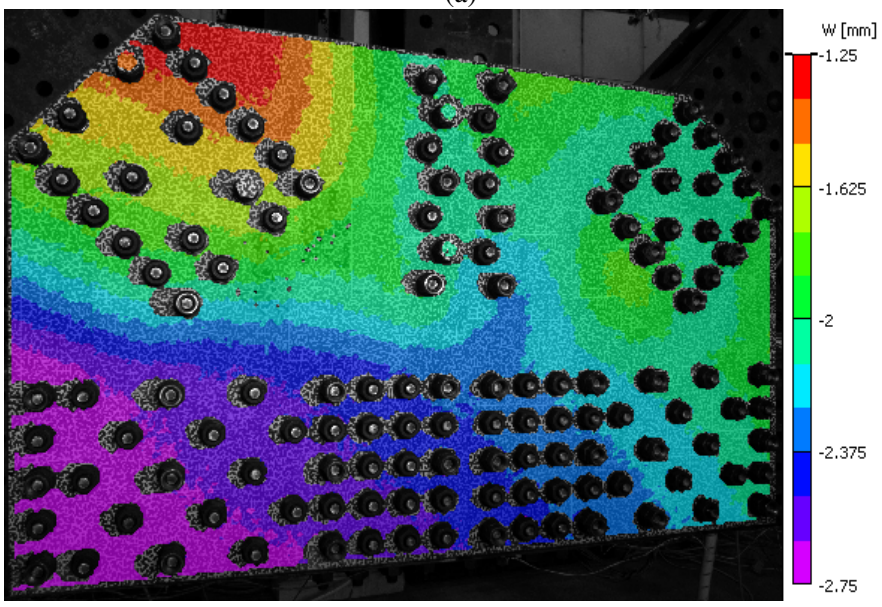

(b)

Figure 43: Out-of plane displacement (W) fields from the reference state to current plate shape for GP490-SS3-1 at ALF of (a) 0.19, (b) 0.45, (c) 0.69, and (d) 0.92 (failure).

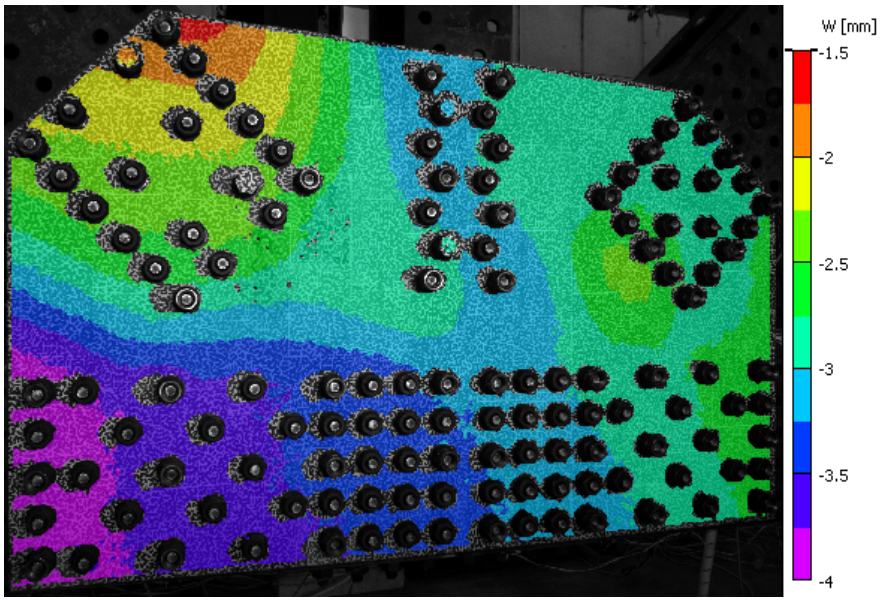

(c)

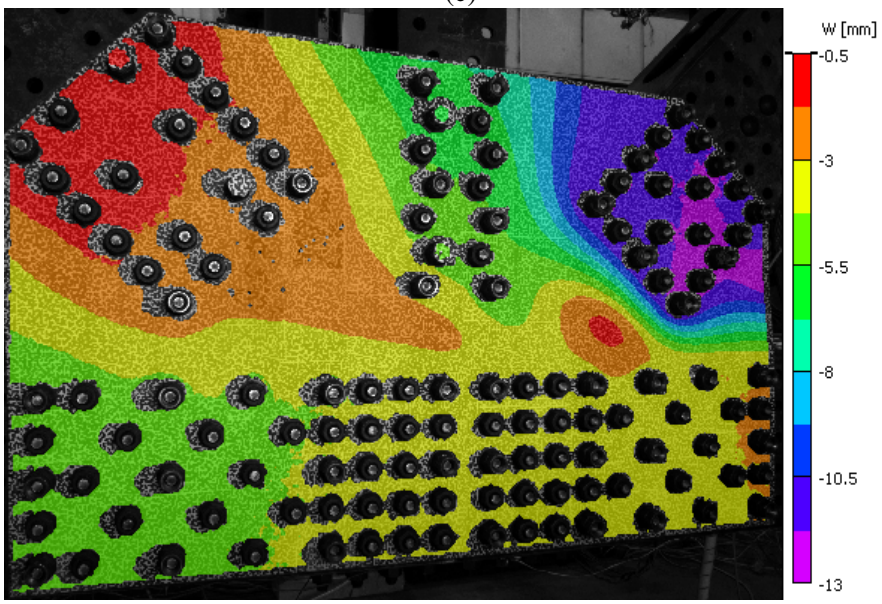

(d)

Figure 43 (continued)

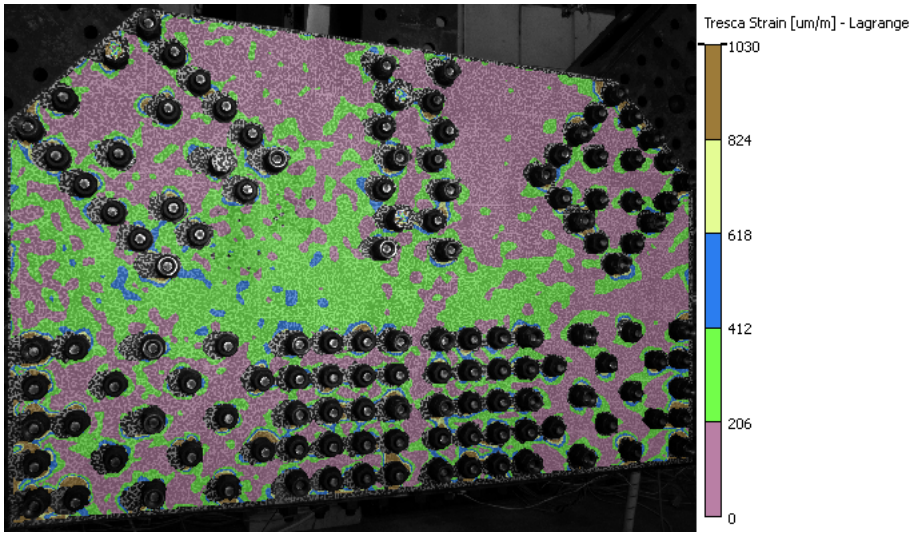

(a)

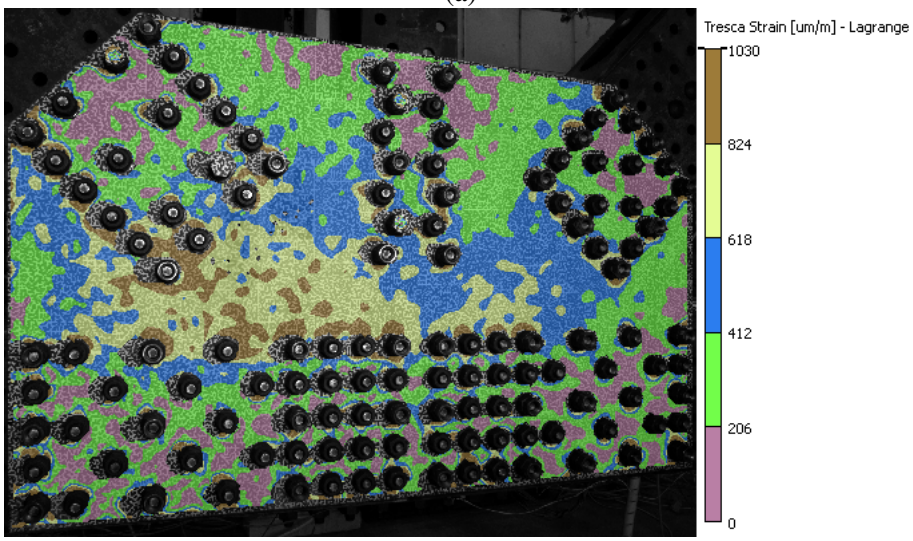

(b)

Figure 44: Maximum in-plane shear strain for GP490-SS3-1 at ALF of (a) 0.19, (b) 0.45, (c) 0.69, and (d) 0.92 (failure), with initial yield at 1030 μm/m.

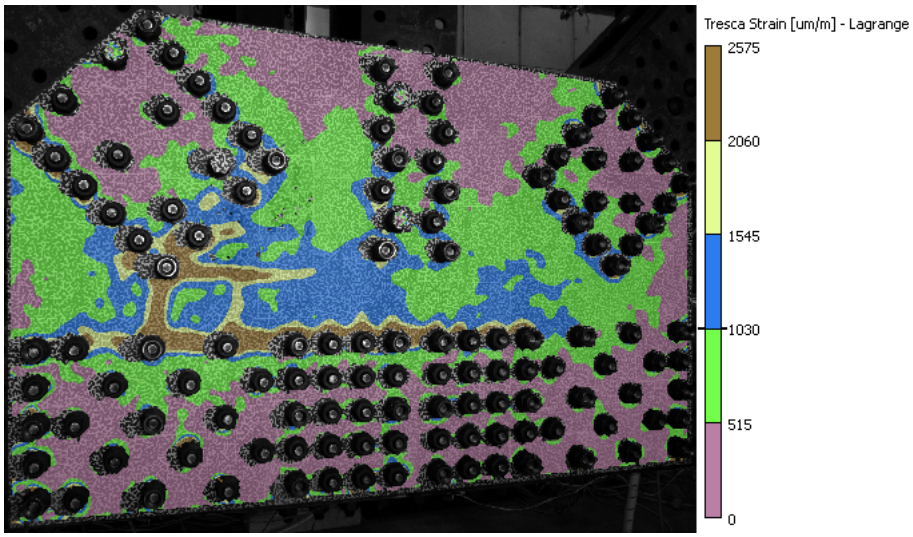

(c)

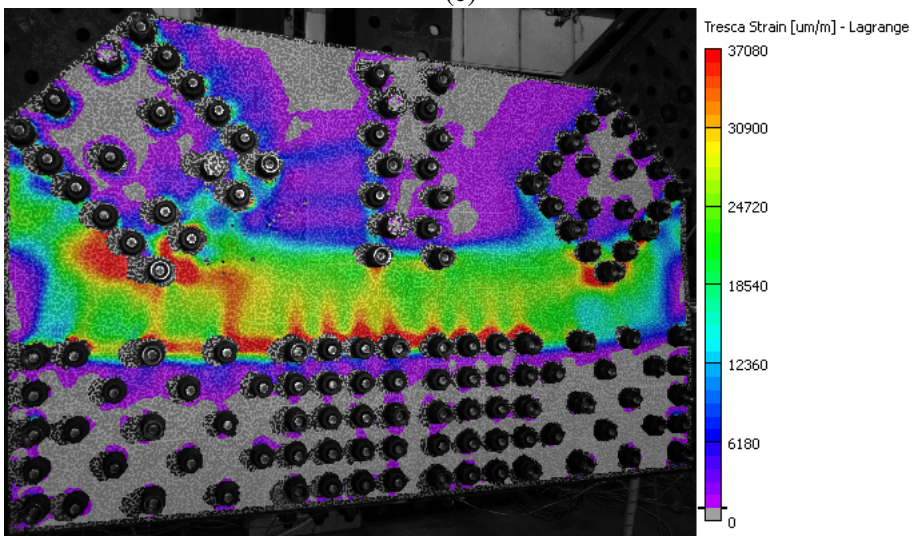

(d)

Figure 44 (continued)

subset spacing (average S = 5 mm, Table 5) while the brittle coating may capture much finer areas of high strain.

In Fig. 48b and c, the bands of high Tresca strain are located in similar position to some of the white lines on the brittle coating at the same load level. These areas along the East Chord bolt line, between the Chord and Vertical bolts, and between the lower Tension Diagonal bolts and the Vertical and East Chord. There also exists additional white lines in the brittle coating (Fig. 48b) extending from the Tension diagonal bolt closest to the Vertical and extending from the second bolt from the plate edge on the East Chord. These two lines do not have a clear corresponding band in Fig. 48c, which shows these areas are only being elastically deformed. There also exists an area of plastic strain in Fig. 48c above the West Chord that is somewhat diffuse, that does not correspond to any visible change in the brittle coating (Fig. 48b). The lower spatial resolution of the DIC versus the brittle coating may explain the white bands where the DIC measures only elastic strain, but does not explain the area that has DIC measured plastic strains where there is no change in the brittle coating. This latter result could be a result of the the out of plane shape near the Compression Diagonal (Fig. 45) which starts concave to the North and continues developing in that direction (Fig. 46), which suggests the South plate may be concave in the same location. This could result in some bending and increased tensile strains in the North plate and decreased tensile strains in the South plate below the Compression Diagonal.

Figure 49 shows similar behavior to Fig. 48 after the failure load (ALF = 0.88) had been reached and the connection had been unloaded. Most of the bands seen in the brittle coating (Fig. 49b) are also seen in the DIC results (Fig. 49c) although not to the same level of spatial refinement. Again there are areas below the Tension Diagonal that show bands that are not fully reflected in the DIC data. Although areas near the Compression Diagonal that show plastic strains in the DIC results (Fig. 49c) that are not reflected in the brittle coating image (Fig. 49b) are also visible in (Fig. 49), there also are some bands to the West of the Vertical that appear in both the brittle coating and DIC results.

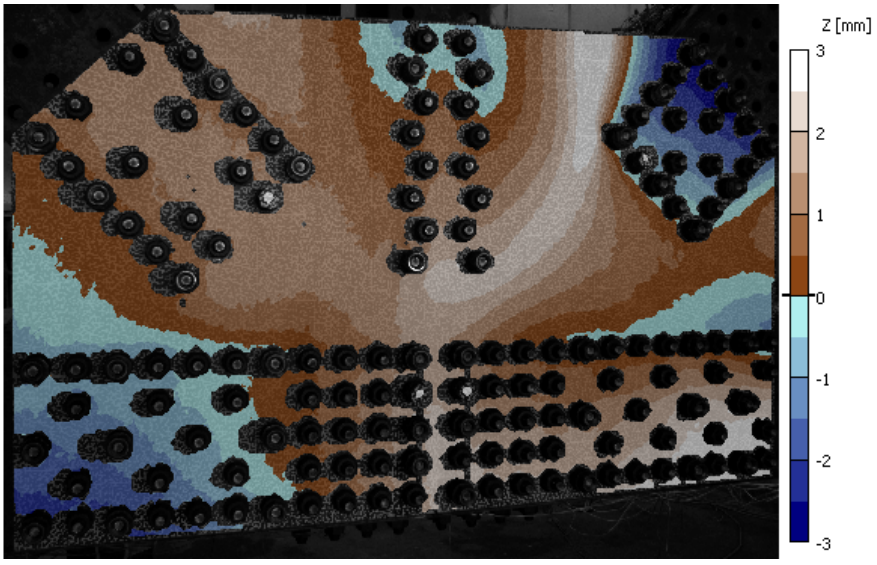

Figure 45: Out-of-plane shape of specimen GP490-LS3-1 at zero load (ALF = 0).

7.2.12 GP490-LS3-2

Figure 50 shows the initial shape of GP490-LS3-2, with two angles added on the upper plate edge and the West plate edge, at the start of the failure test under no load. The location of Z = 0 mm was set using three points as in the other cases. After the rotation, the plate has a slight saddle shape with the Tension Diagonal and West Chord in the negative Z-direction and the Compression Diagonal and East Chord in the positive Z-direction. Figure 51 shows the evolution of the Z-direction displacement from the initial shape in Fig. 50. The ALF values are in regards to the Compression Diagonal load (Table 4). During the test, the entire plate shifted toward the negative Z-direction from an early stage, through the final buckling of the Compression Diagonal in the negative Z-direction with a convex bulge of the plate under the Compression Diagonal (Fig. 51d). Figure 52 plots the maximum in-plane shear strains at the same four ALF levels shown in Fig. 51. The yield strain in terms of Tresca strain is approximately 1020 μm/m, based on standard material testing of the same material. Figures 52a–c have strain ranges predominately in the elastic range and use a pseudorandom color map. Figure 52d has a strain range predominately in the plastic strain range (spectrum color map) with grey being used for areas of the plate that have not yet reached the yield strain. The results show that the Tresca strains were concentrated between the end of the Compression Diagonal and the West Chord from the early stages of loading, with the largest strains occurring at the end of the Compression Diagonal and along the West Chord bolt lines (Fig. 52c). The strain field is more diffuse in the early stages of loading (Fig. 52a and b). In the later stages (Fig. 52c and d) more strain localizations are present, starting in Fig. 52c and extend between the Compression Diagonal bolt lines to the Vertical and West Chord bolt lines.

7.3 Comparison

Figures 53a–n replot the Tresca strain results shown at the highest ALF values in the Section 7.2, but on a common legend range with grey being used for areas of the plate that have strains $<$ 970 μm/m (the average yield value). Figure 53h is for GP307-SS3-4 referenced to the initial unloaded plate at maximum load. However, Fig. 53i and j are for GP307-SS3-shingle after the premature bolt failure (unloaded) referenced to the initial unloaded plate, and at maximum load after reassembly referenced to the reassembled (but deformed) unloaded plate, respectively. The total strain for GP307-SS3-shingle is the addition of the strains in Fig. 53j to the strains at the unloaded state just after the premature bolt failure in Fig. 53i. The predominant strain pattern at failure for most of the plates tested is bands of localized strain that extend between the adjacent bolt lines and along the top Chord bolt line. Two plates, GP307-SS3-1 in Fig. 53e and to a lesser extent GP307-LS3 in Fig. 53b, show buckling related strains being the dominant strains present. Only plates GP307-SS3-2 and GP307-SS3-3 (Figs. 53f and g, respectively), which have sections reduced in thickness as an analog to corrosion related section loss, show more uniform areas of high strain (in the reduced thickness areas). The only localized bands of strain seen in these two cases are of much lower magnitude between the Vertical and the diagonals (blue bands in Fig. 53g). One could separate the plates with distinct localized strain bands into two groups based on the maximum strain achieved using the middle value of the common range (17 460 μm/m) as a threshold. The plates with strains higher than 17 460 μm/m (Fig. 53c, d, h/j, and l) have undergone substantial shear strain, typically well in excess of the threshold, along the Chord bolt lines and/or in the plate areas between the two diagonals. The plates with maximum strains lower than 17 460 μm/m (Fig. 53a, k, m, and n) have developed some distinct localized strain bands, but the plate seems to have failed by buckling before the shear strain on the plate could become dominant.

8 SUMMARY

An overview of 3D digital image correlation measurements during testing of large structural connections has been presented. Twelve full-scale bridge gusset plate connections were tested with various geometries and boundary conditions (Ocel et al., 2012). These experiments are part of the NCHRP Project 12-84 “Guidelines for the Load and Resistance Factor Design and Rating of Riveted and Bolted Gusset Plate Connections for Steel Bridges”. The measurements described here are in regards to the tests performed to failure (i.e., maximum load carrying capacity of the connection). This report only presents a very small portion of the overall DIC measurements, but the remainder of the results will be made available.

The layout, calibration, and measurement procedure associated with the digital image correlation system were described in detail to aid in understanding of the results. A specially designed black on white pattern was applied to the samples for the correlation analysis to track throughout the loading process. During each of the twelve tests to failure, a series (typically about 150) of image pairs were taken for subsequent digital image correlation analysis. Although all of the image pairs were processed, only a very small portion of the results are presented here. In the Results (Section 7), an Example Case (Section 7.1) of the variables that are measured and derived from

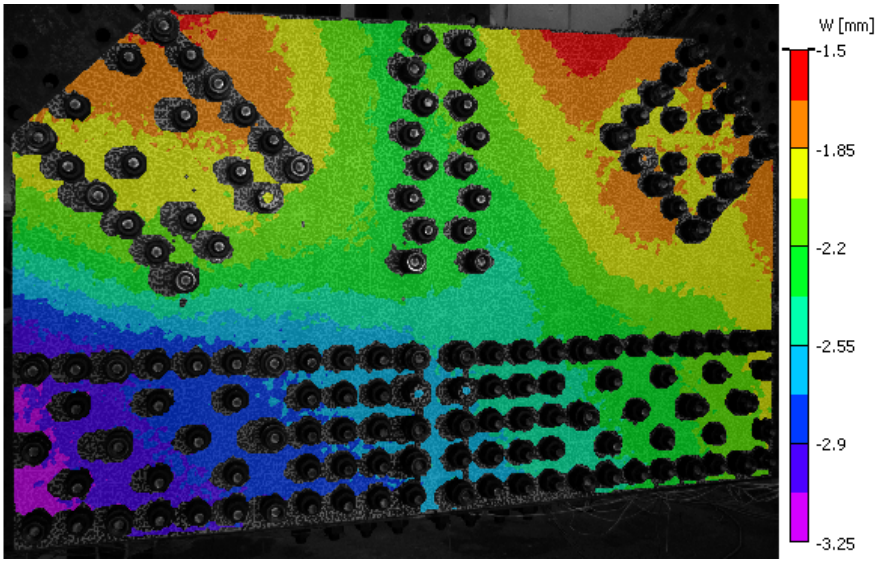

(a)

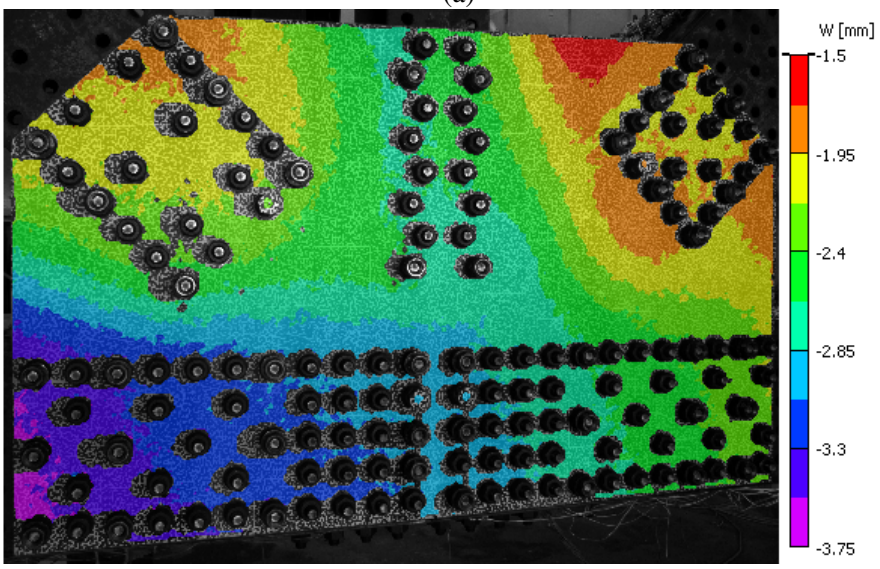

(b)

Figure 46: Out-of plane displacement (W) fields from the reference state to current plate shape for GP490-LS3-1 at ALF of (a) 0.43, (b) 0.53, (c) 0.68, and (d) 0.88 (failure).

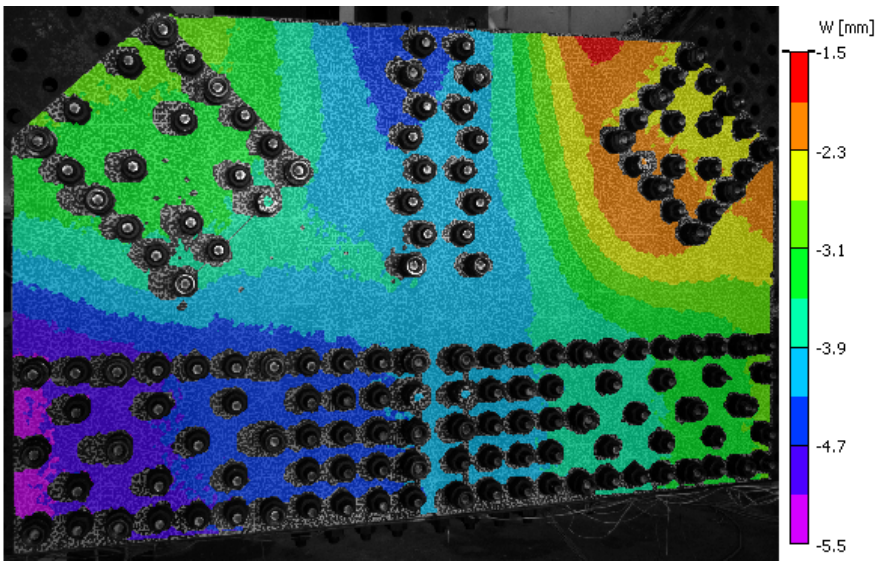

(c)

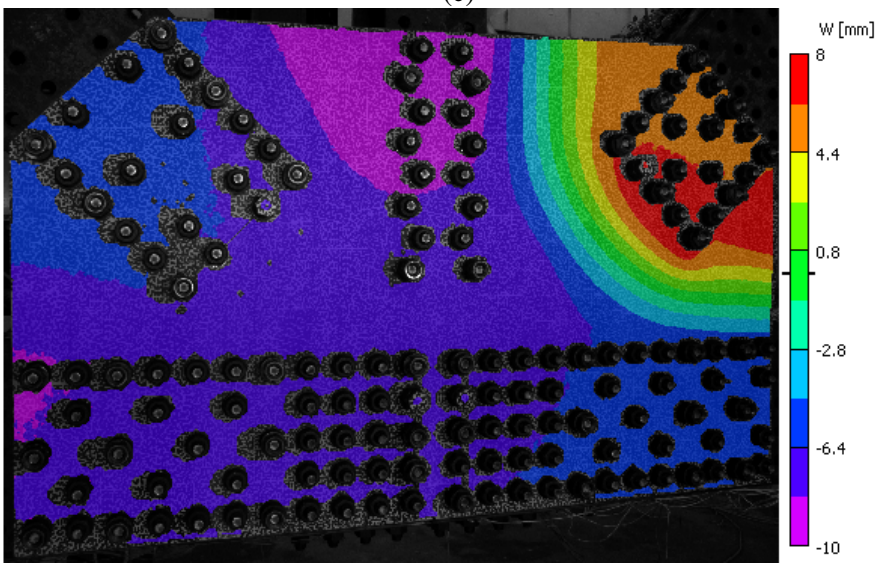

(d)

Figure 46 (continued)

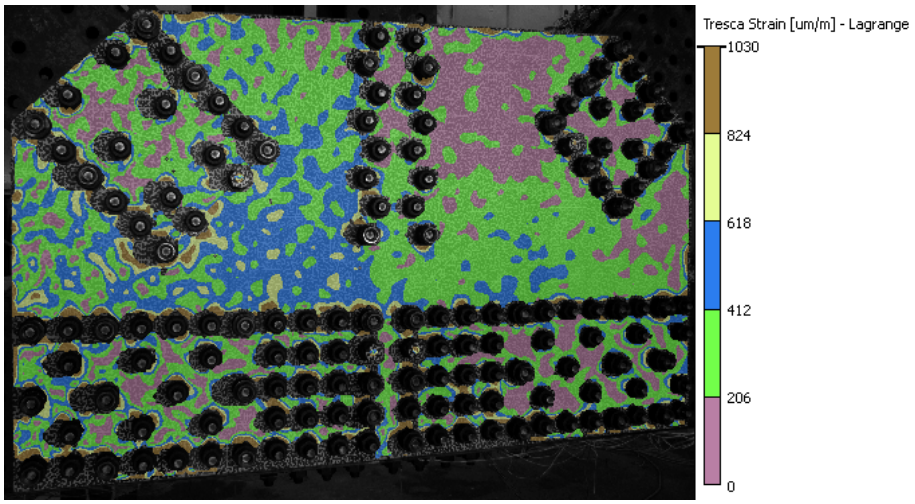

(a)

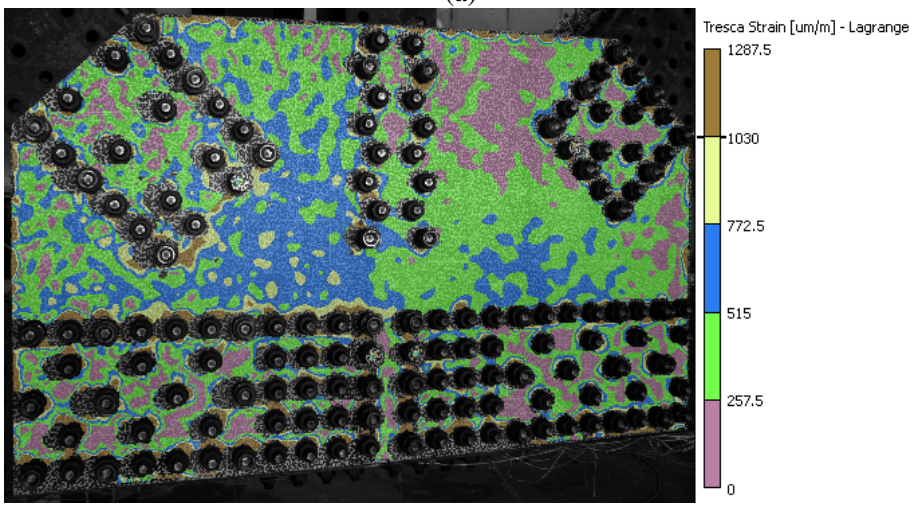

(b)

Figure 47: Maximum in-plane shear strain for GP-490LS3-1 at ALF of (a) 0.43, (b) 0.53, (c) 0.68, and (d) 0.88 (failure), with initial yield at 1040 μm/m.

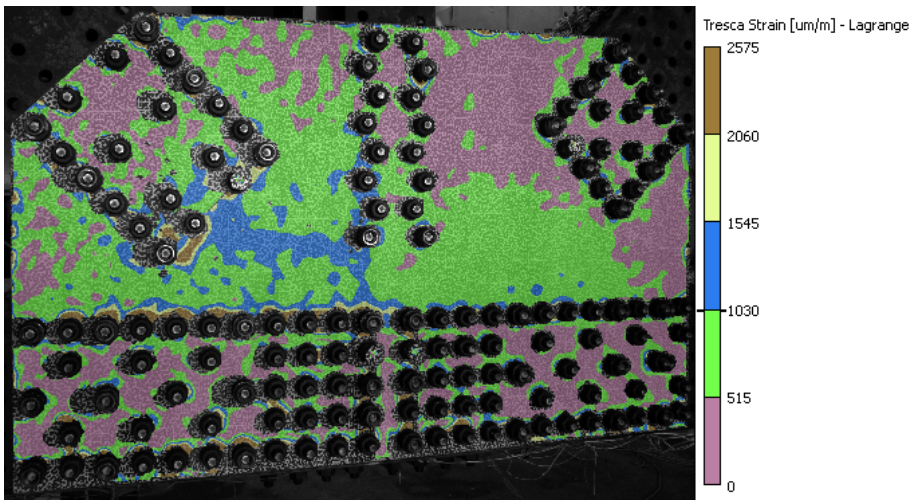

(c)

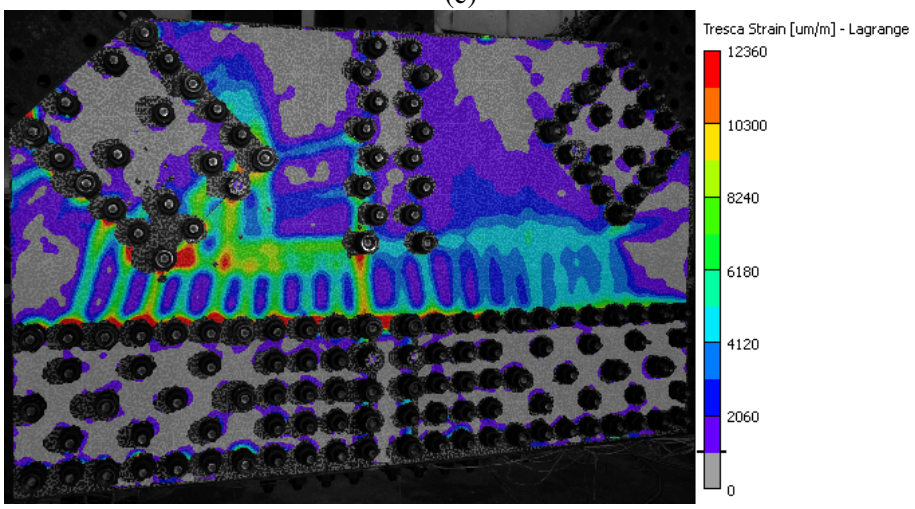

(d)

Figure 47 (continued)

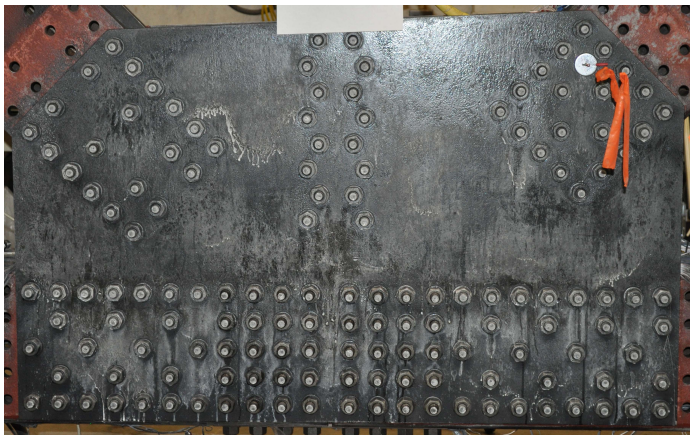

(a)

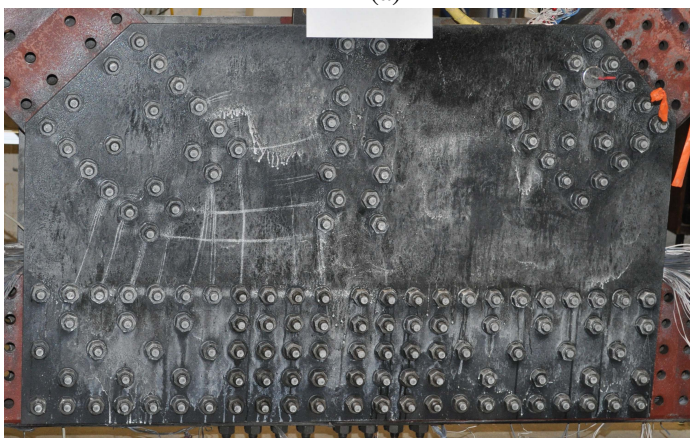

(b)

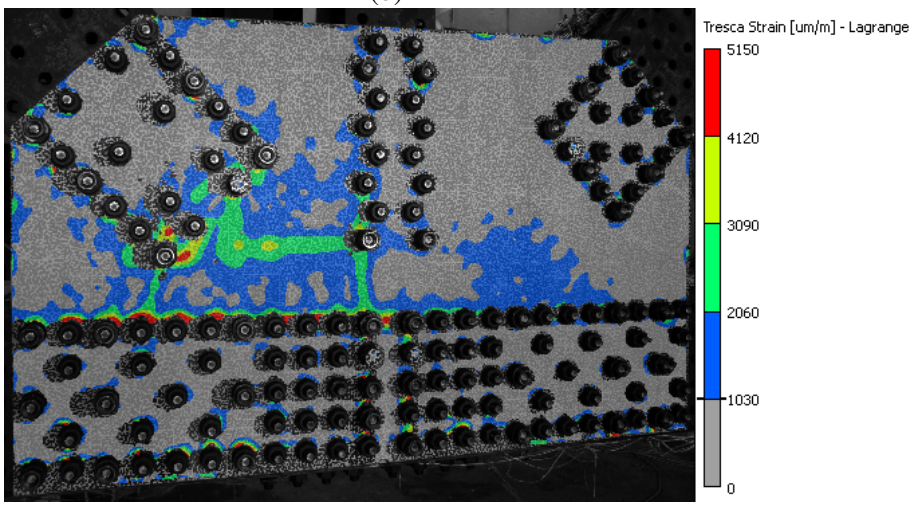

(c)

Figure 48: Comparison of brittle coating and maximum in-plane shear strain for GP490-LS3-1 connection. Mirror images of brittle coating on South gusset plate (a) unloaded initial condition and (b) at ALF = 0.75, and (c) maximum in-plane shear strain for North gusset plate at ALF = 0.75.

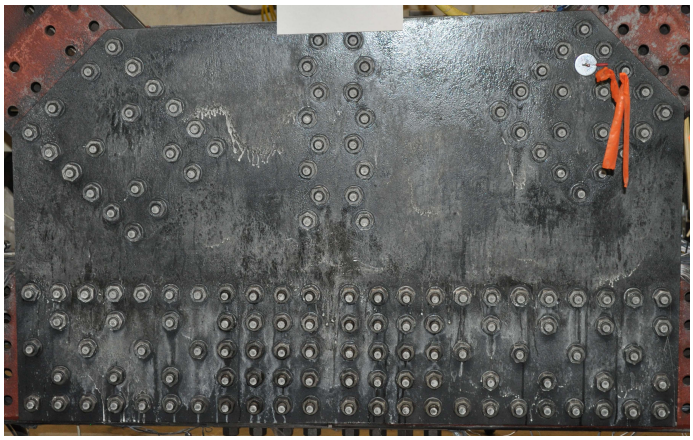

(a)

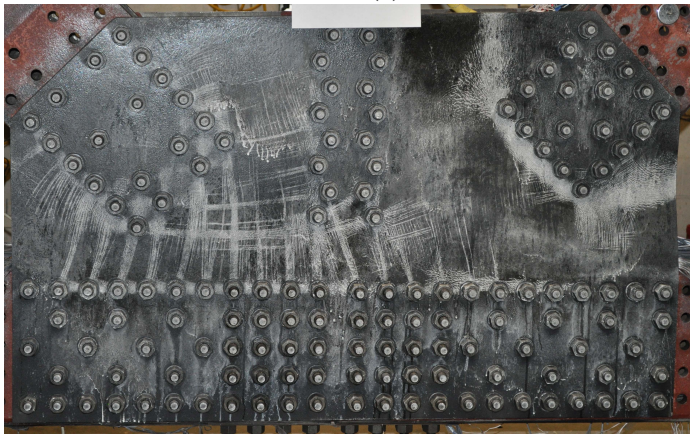

(b)

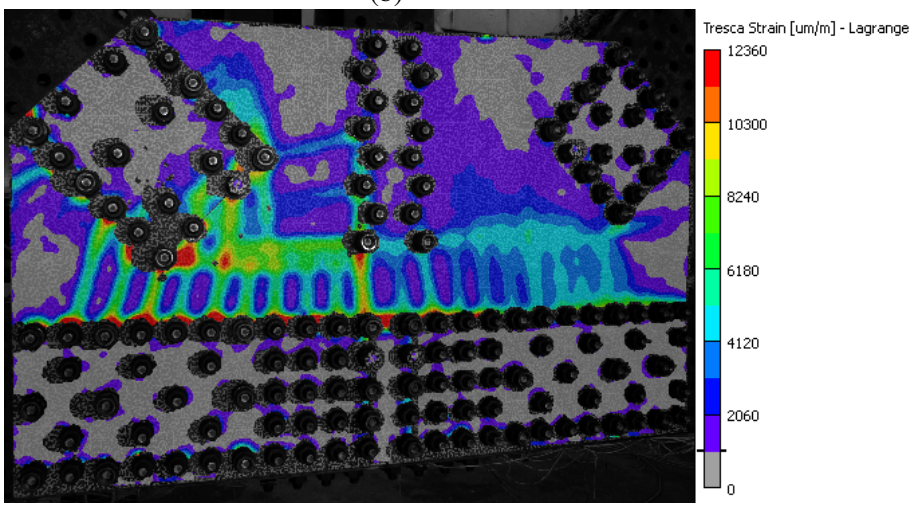

(c)

Figure 49: Comparison of brittle coating and maximum in-plane shear strain for GP490-LS3-1 connection. Mirror images of brittle coating on South gusset plate (a) unloaded initial condition and (b) unloaded after ALF = 0.88 (failure), and (c) maximum in-plane shear strain for North gusset plate at ALF = 0.88.

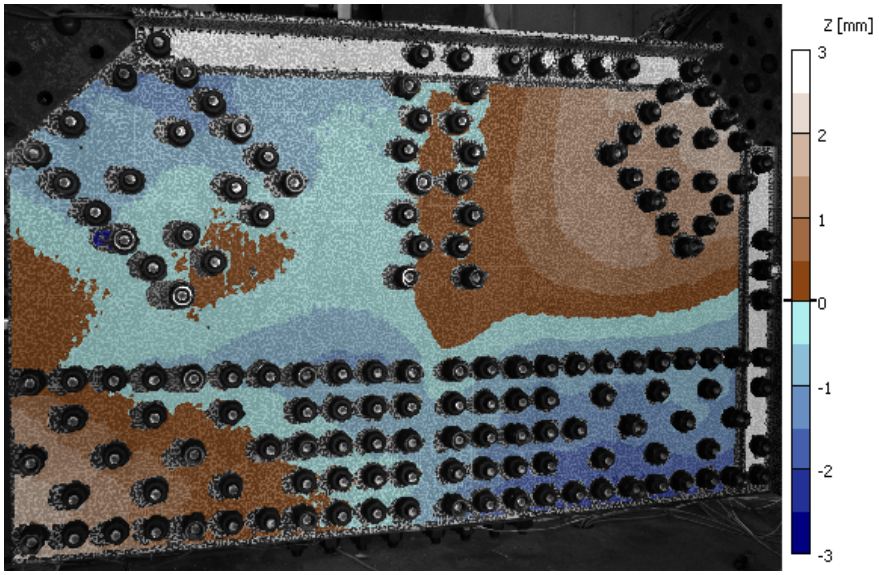

Figure 50: Out-of-plane shape of specimen GP490-LS3-2 (and reinforcement structural angles) at zero load (ALF = 0).

those measurements was presented for one plate (GP307-SL3) at two points during testing (i.e., the initial condition and at failure). These same data are available for every image pair from the initial condition through the failure condition of each plate tested. Since it is impossible to describe all of these results in a report format, it was decided to present just two additional subsets of the overall digital image correlation data.

The Key Points (Section 7.2) results, show the evolution of the out of plane shape and maximum shear strain field at four points in loading from the initial condition to failure. These are very useful in visualizing the mechanisms (buckling and/or shear failure of the plate) that lead to eventual failure of the connection. Often shearing of the plate dominated the early stages of loading, but by the point of failure there was an out of plane motion of the Compression Diagonal more typical of a buckling failure. This evolution is often seen as even more gradual when looking at all of the data for a given test. The evolution of maximum in-plane shear strain bands is seen quite clearly in many of the plates. These localized bands of deformation frequently extended from the bolt lines of one member to another through the large open areas of the plate, while these bands also occurred along the top bolt lines of the two Chord members.

The final section of the results again plots the failure strain fields of Section 7.2, but on a common contour scale to permit Comparison (Section 7.3) of the strain fields from one plate to another. It is in this section that one can more easily see the plates that failed after significant shearing versus the ones that failed with minimal or no shearing. The comparison also shows very clearly the effect of the plates with reduced thickness as an analog to section loss due to corrosion.

Overall the measurements showed reasonable uncertainties on the order of $\pm$ 175 μm/m of

maximum in-plane shear strain. The measured out of plane initial shapes of the plates typically matched qualitative inspections of the connection, and with the exception of one plate (GP307-LS3). These shapes were generally on the same order (about $\pm$ 4 mm) as measurements through other methods. The large (about $\pm$ 20 mm) out of plane twisted initial shape does not seem reasonable, and puts the calibration for plate GP307-LS3 into question. The same effect was not seen in the uncertainty analysis for the out of plane displacements from the initial shape or the maximum shear strains calculated at zero load. Further, the results for the deformed shapes and strains did not show a similar variation based on the location in the images suggesting the results were not effected as dramatically.

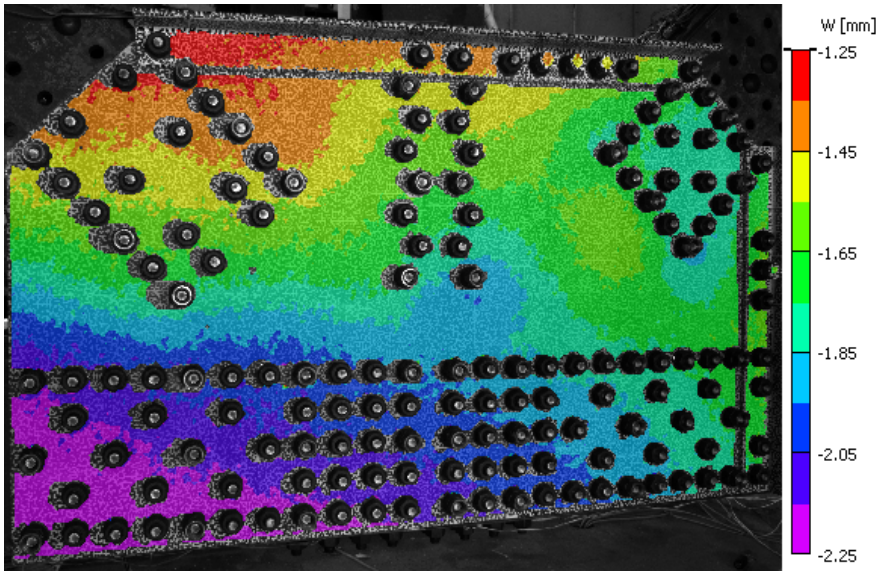

(a)

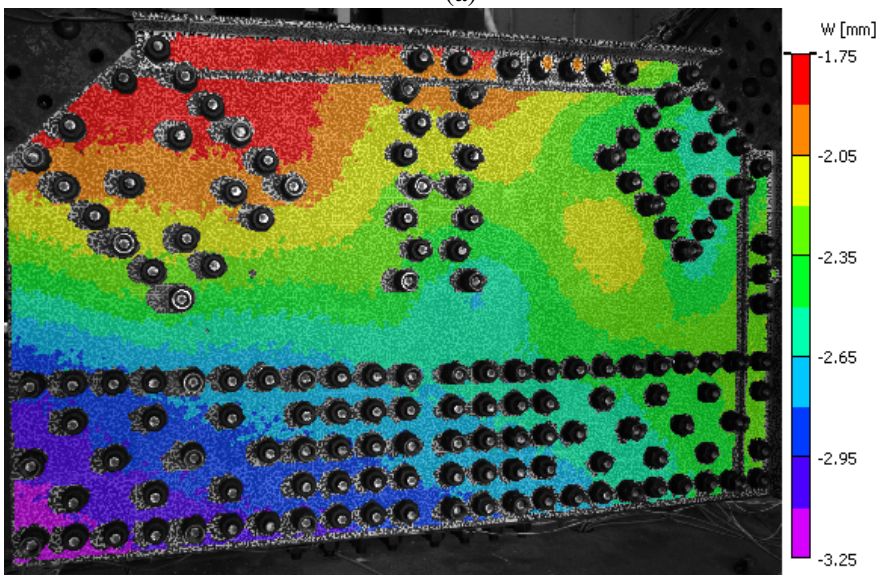

(b)

Figure 51: Out-of plane displacement (W) fields from the reference state to current plate shape for GP490-LS3-2 (and reinforcement structural angles) at ALF of (a) 0.31, (b) 0.48, (c) 0.68, and (d) 0.87 (failure).

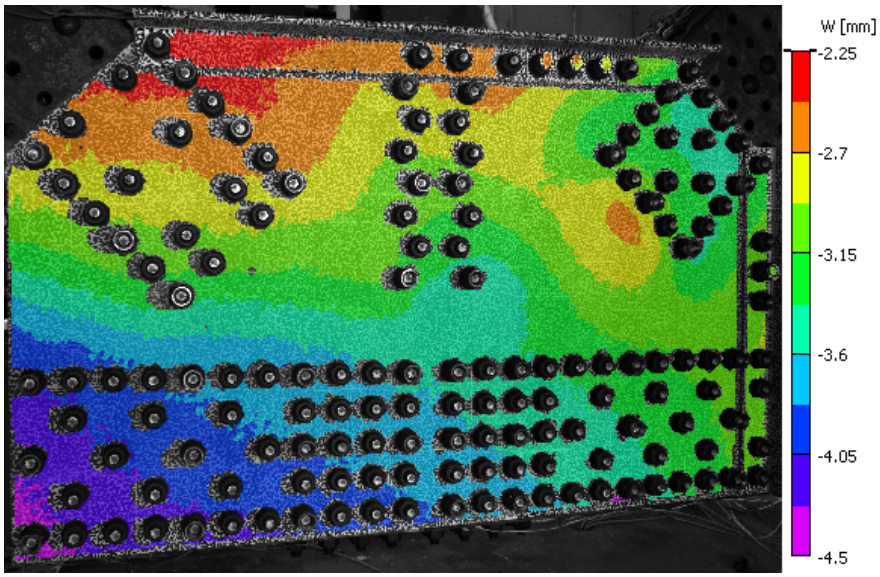

(c)

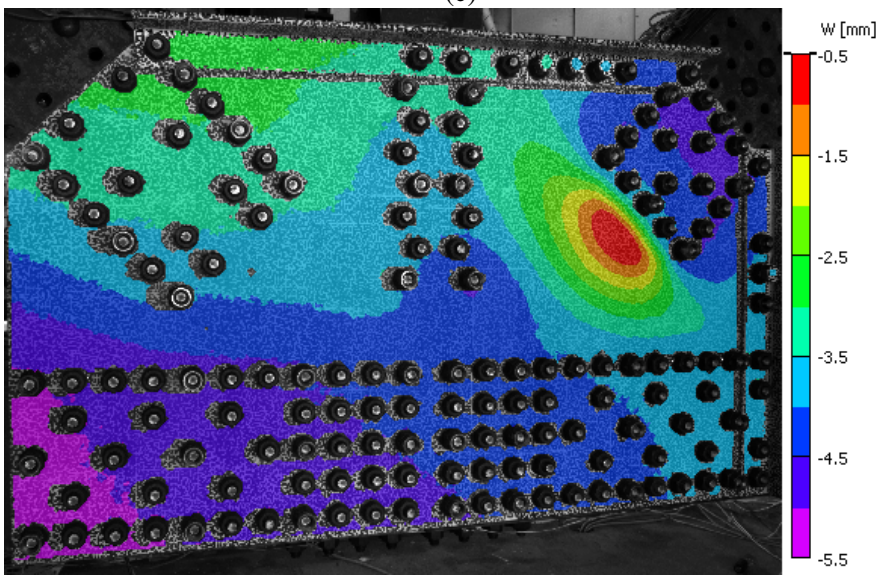

(d)

Figure 51 (continued)

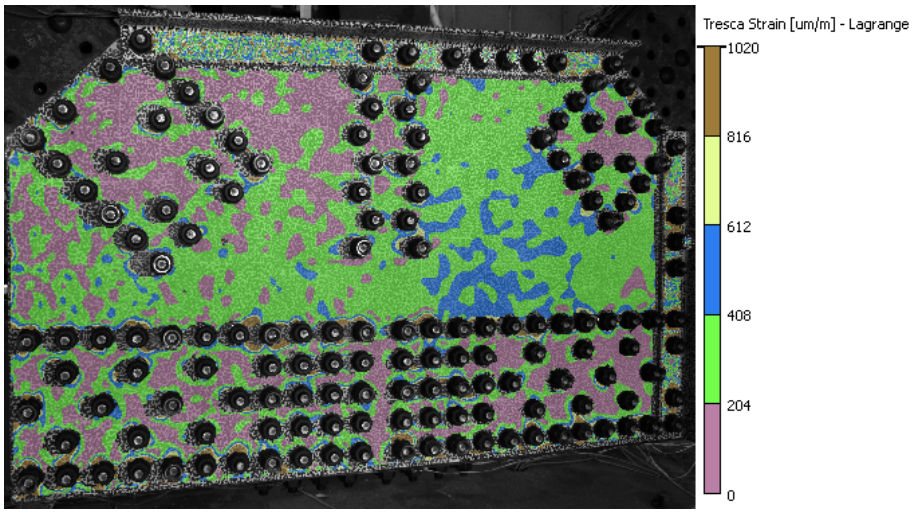

(a)

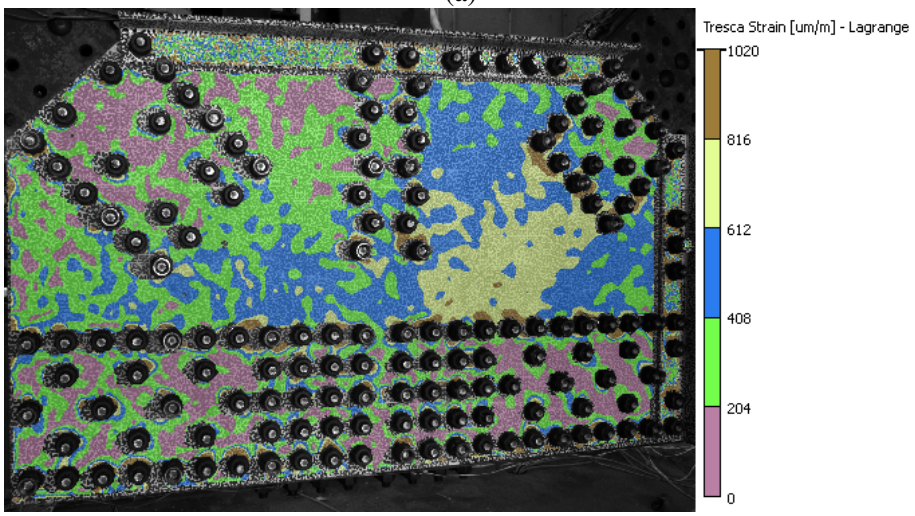

(b)

Figure 52: Maximum in-plane shear strain for GP490-LS3-2 (and reinforcement structural angles) at ALF of (a) 0.31, (b) 0.48, (c) 0.68, and (d) 0.87 (failure), with initial yield at 1020 μm/m.

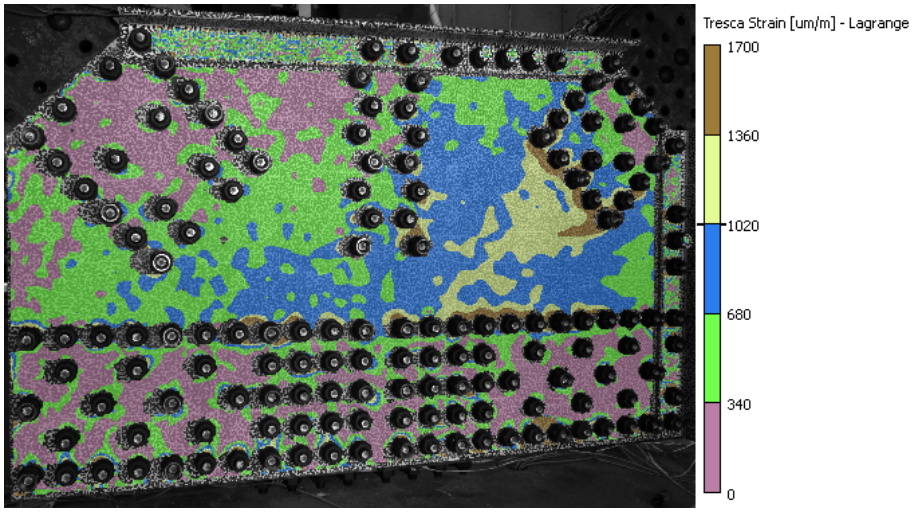

(c)

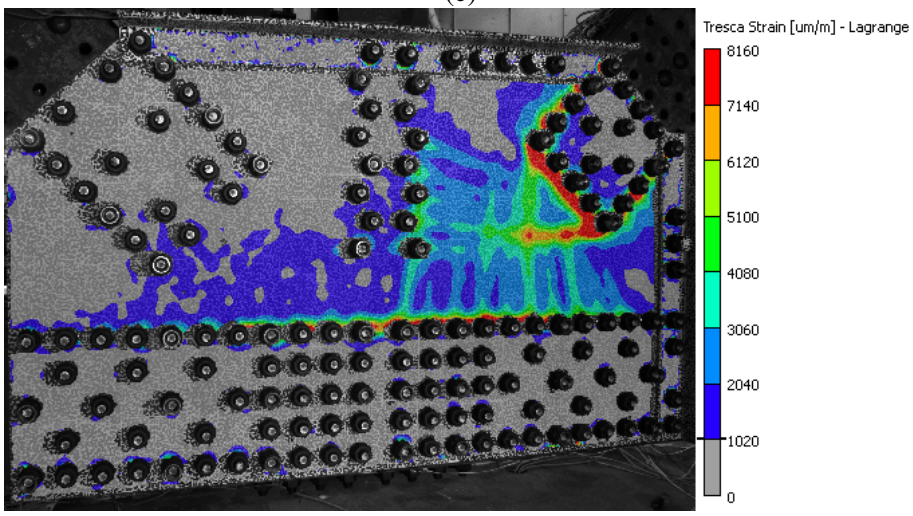

(d)

Figure 52 (continued)

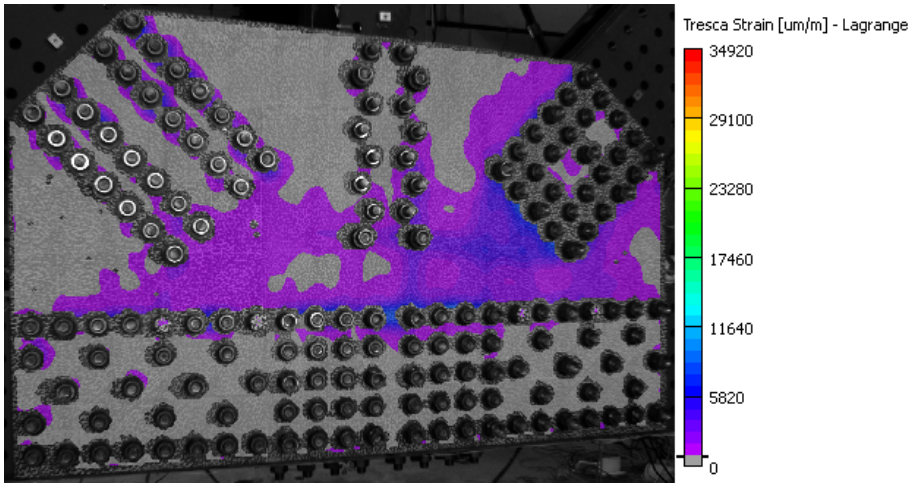

(a)

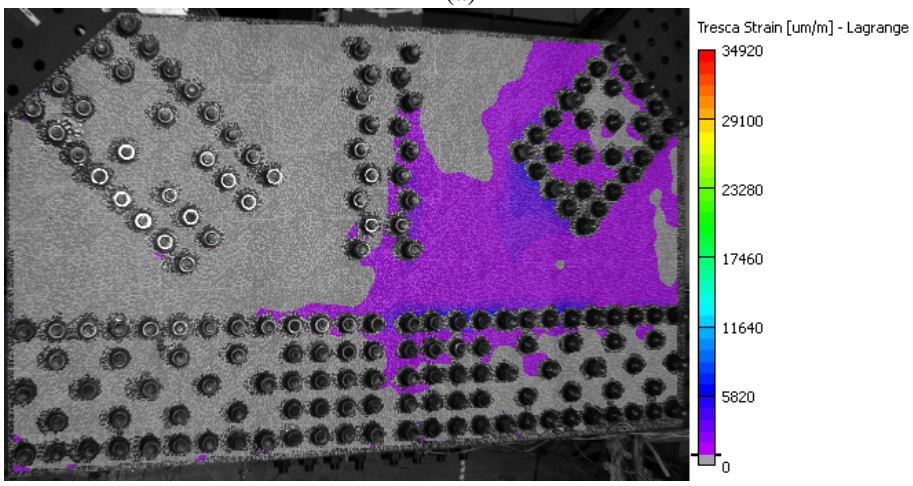

(b)

Figure 53: Failure strains on a common color scale range: (a) GP307-SS3, (b) GP307-LS3, (c) GP307-SL3, (d) GP307-SL4, (e) GP307-SS3-1, (f) GP307-SS3-2, (g) GP307-SS3-3, (h) GP307-SS3-4, (i) GP307-SS3-shingle (after premature bolt failure and unload), (j) GP307-SS3-shingle (referenced to the reassembled, but deformed, specimen) (k) GP490-SS3, (l) GP490-SS3-1, (m) GP490-LS3-1, and (n) GP490-LS3-2

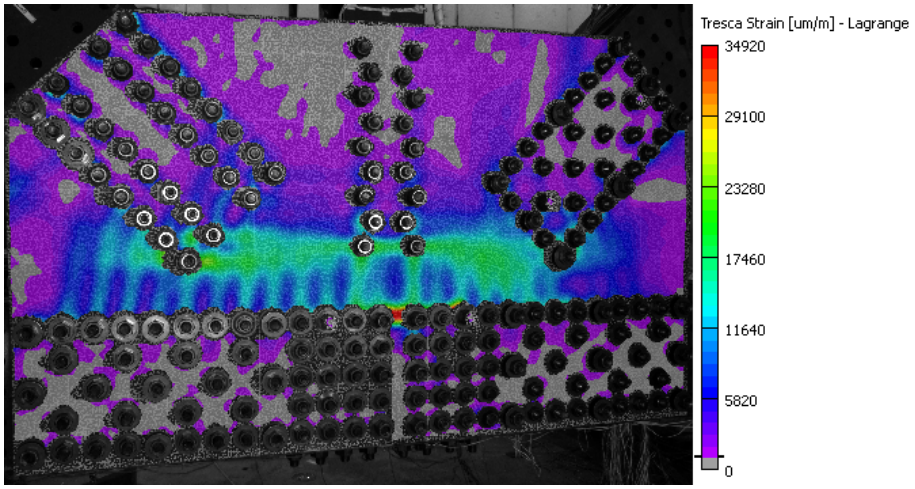

(c)

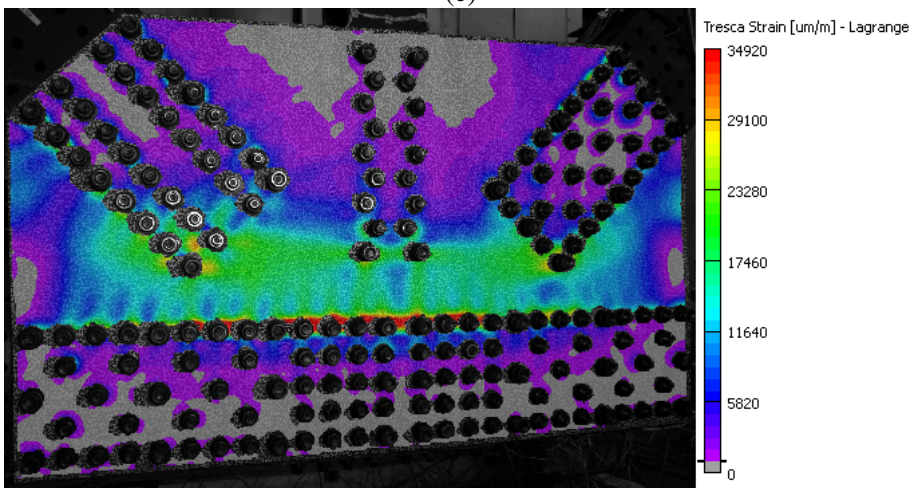

(d)

Figure 53 (continued)

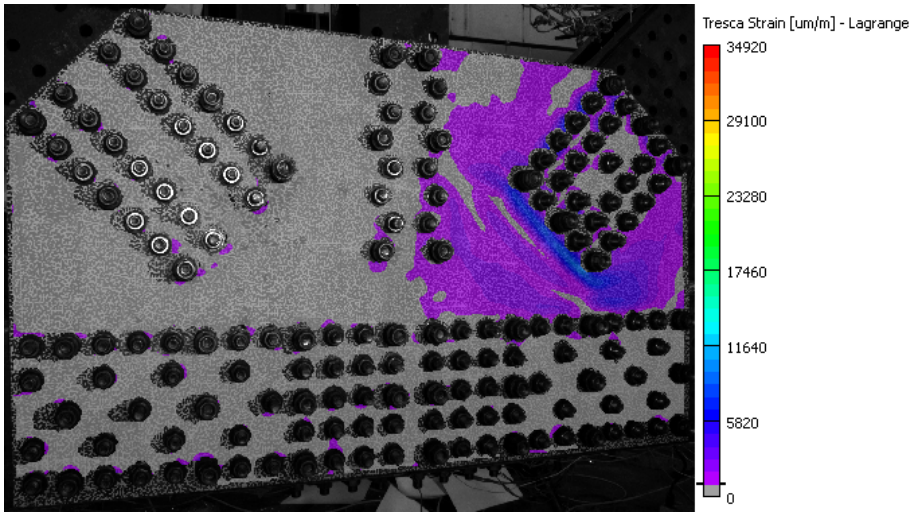

(e)

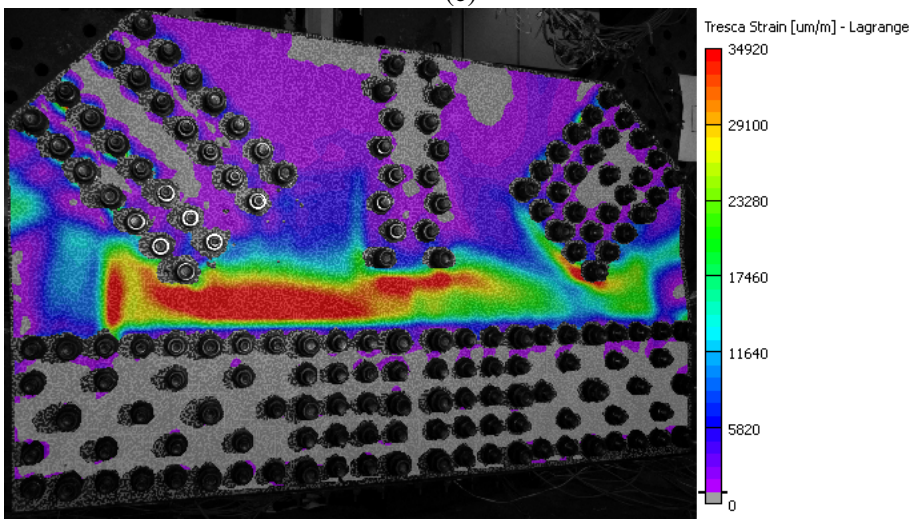

(f)

Figure 53 (continued)

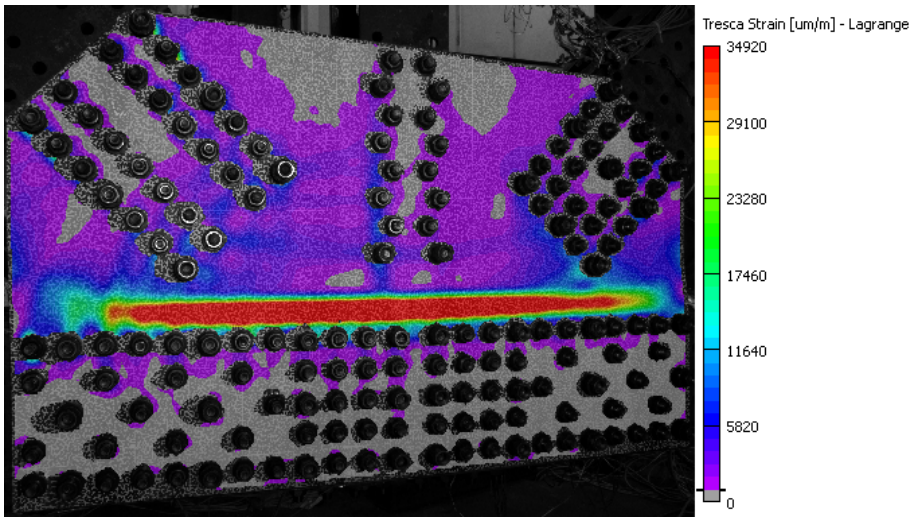

(g)

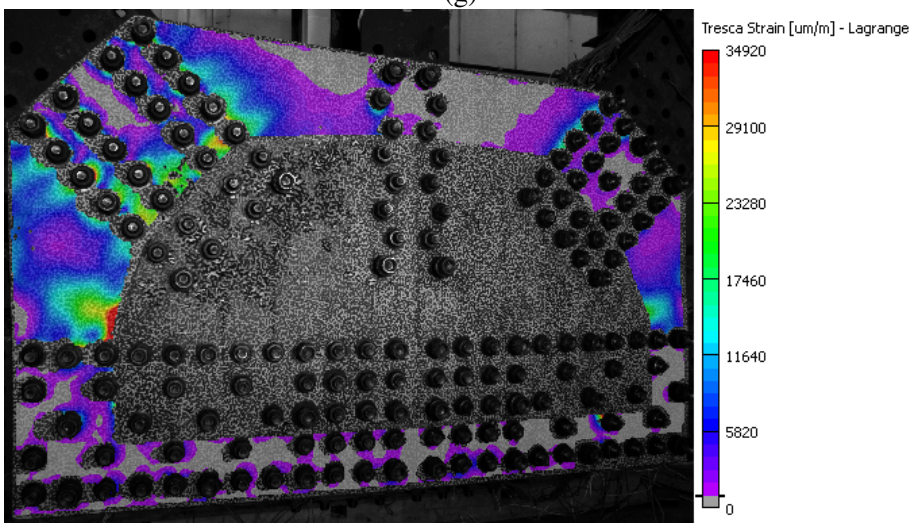

(h)

Figure 53 (continued)

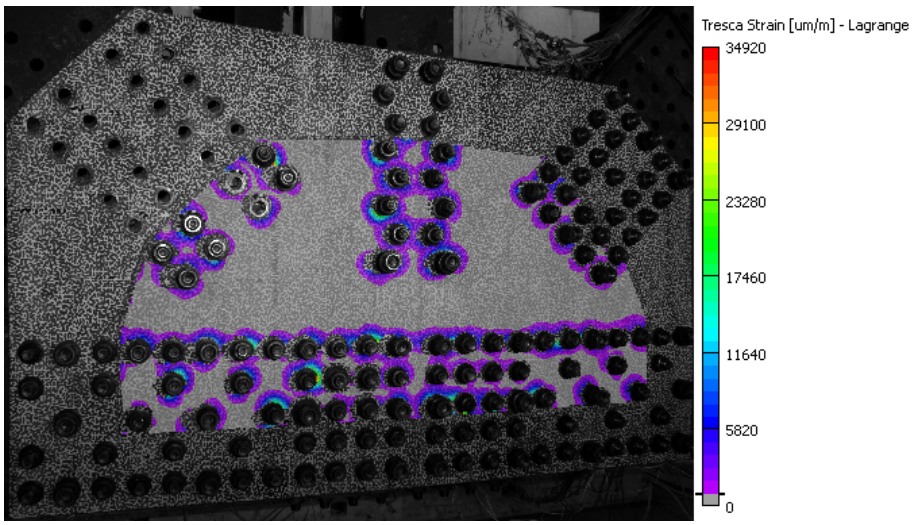

(i)

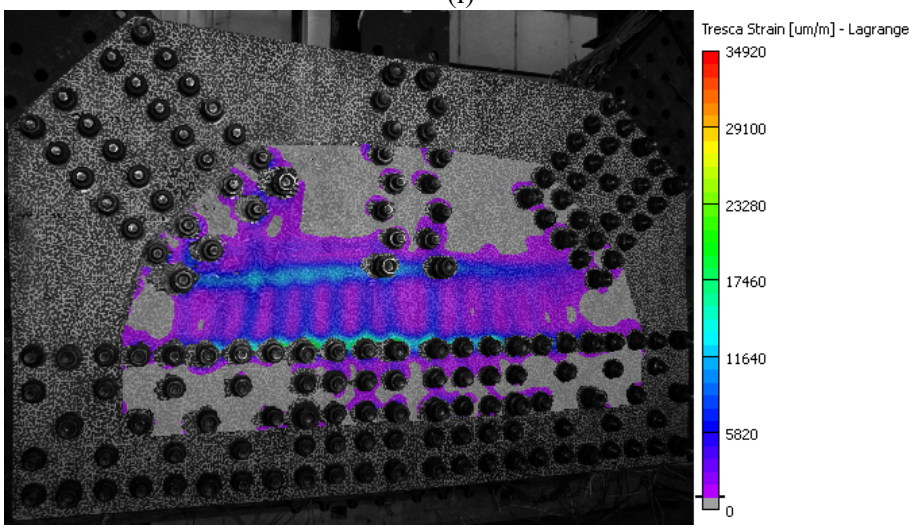

(j)

Figure 53 (continued)

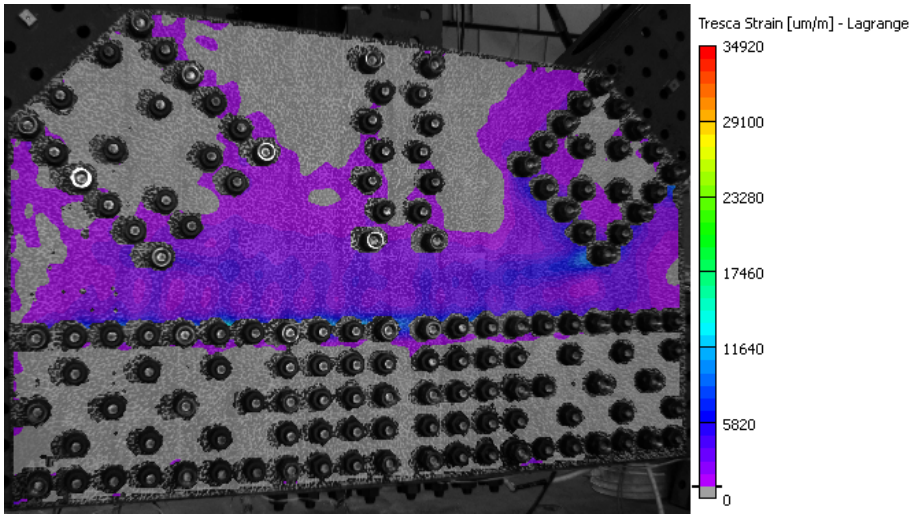

(k)

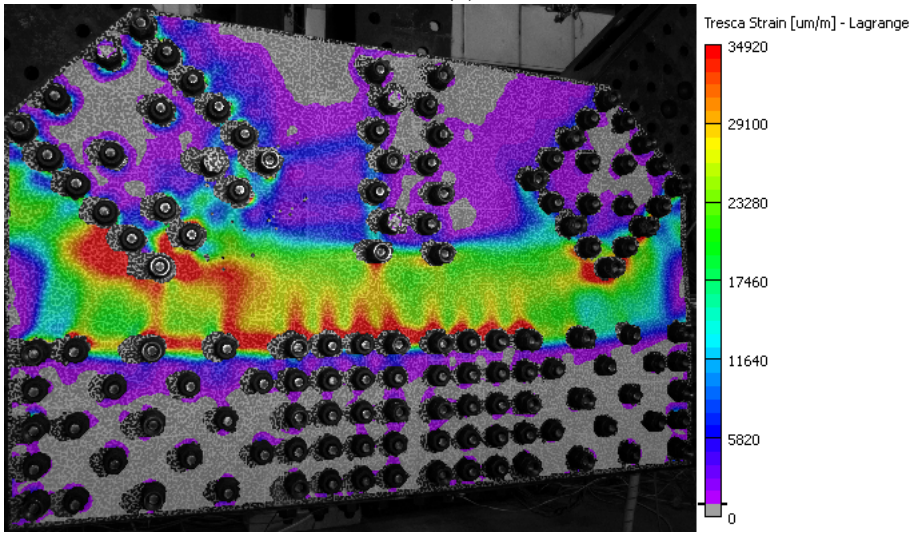

(l)

Figure 53 (continued)

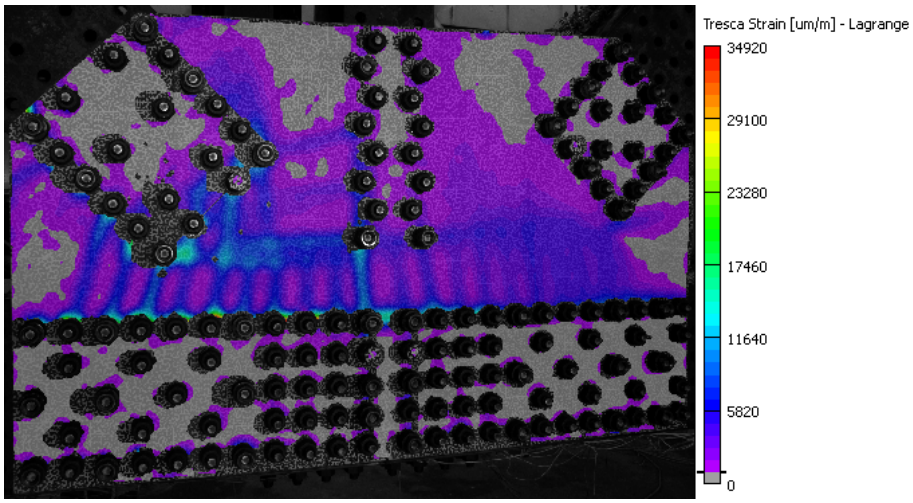

(m)

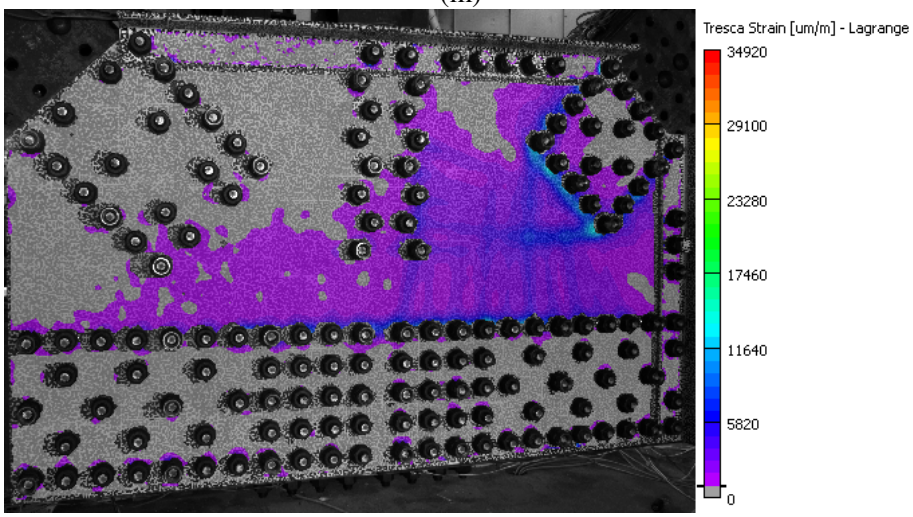

(n)

Figure 53 (continued)

References

De Roover, C., Vantomme, J., Wastiels, J., and Taerwe, L. (2002). Deformation analysis of a modular connection system by digital image correlation. *Experimental Techniques*, 26(6):37–40.

Hild, F., Roux, S., Guerrero, N., Eugenia Marante, M., and Flórez-López, J. (2011). Calibration of constitutive models of steel beams subject to local buckling by using digital image correlation. *European Journal of Mechanics A - Solids*, 30(1):1–10.

Iadicola, M. A., Zobel, R. S., and Ocel, J. M. (2012). Quantitative evaluation of digital image correlation as applied to large–scale gusset plate experiments. In Biondini, F. and Frangopol, D. M., editors, *Bridge Maintenance, Safety, Management, Resilience and Sustainability: Proceedings of the Sixth International IABMAS Conference, Stresa, Lake Maggiore, Italy, 8-12 July 2012*. Taylor & Francis.

Junda, C., Guanchang, J., and Libo, M. (2007). Applications of digital correlation method to structure inspection. *Tsinghua Science and Technology*, 12(3).

Kitagawa, A., Nakatani, M., Ashida, S., Tani, K., Ishihara, T., and Katada, T. (2007). Developments of full-field optical measurement methods for structure inspection. *Hitachi Zosen Technical Review*, 67(1).

Kohut, P., Holak, K., and Uhl, T. (2008). Application of image correlation for SHM of steel structures. In *Proceedings of the Fourth European Workshop on Structural Health Monitoring 2008*, pages 1257–1264.

Kujawińska, M., Bukalska, M., and Dymny, G. (2010). Hybrid digital image correlation/thermovision system for monitoring of civil engineering structures. In *10th International Conference on Quantitative InfraRed Thermography*.

Kujawinska, M., Malesa, M., Malowany, K., Piekarczuk, A., Tymińska-Widmer, L., and Targowski, P. (2011). Digital image correlation method: a versatile tool for engineering and art structures investigations. In Rodriguez-Vera, R. and Diaz-Uribe, R., editors, *22nd Congress of the International Commission for Optics: Light for the Development of the World*, volume 8011, pages R1–R8. SPIE.

Kujawińska, M., SitnikI, R., Dymny, G., Karaszewski, M., MichońskiI, K., Krzesłowski, J., Mularczyk, K., and Bolewicki, P. (2009). Remote on-line monitoring and measuring system for civil engineering structures. In *Proceedings of SPIE - The International Society for Optical Engineering*, volume 7389, page 2 vol., Bellingham, WA, USA. Society of Photo-Optical Instrumentation Engineers.

Malesa, M., Szczepanek, D., Kujawińska, M., Świercz, A., and Kołakowski, P. (2010). Monitoring of civil engineering structures using digital image correlation technique. In *EPJ Web of Conferences*, volume 6, page 31014.

McCormick, N. J. and Lord, J. D. (2010). Practical in-situ applications of DIC for large structures. In Mines, R.A.W. and DulieuBarton, J.M., editor, *Advances in Experimental Mechanics VII*, volume 24-25 of *Applied Mechanics and Materials*, pages 161–166. 7th International Conference on Advances in Experimental Mechanics, Univ Liverpool, Sch Engn, Liverpool, England, SEP 07-09, 2010.

Mentes, Y., Kim, Y. D., Zobel, R. S., Iadicola, M. A., White, D. W., Leon, R. T., and Ocel, J. M. (2011). Analytical and experimental assessment of steel truss bridge gusset plate connections. In *Proceedings of the* 28^{th} *International Bridge Conference, Pittsburgh, PA*, pages 8–16.

Ocel, J., Zobel, R., White, D., and Leon, R. (2012). FHWA full–scale testing of steel truss bridge gusset plate connections. In *Proceedings of the* 29^{th} *Annual International Bridge Conference, Pittsburgh, PA*.

Sadowski, T., Kneć, M., and Golewski, P. (2010). Experimental investigations and numerical modelling of steel adhesive joints reinforced by rivets. *International Journal of Adhesion and Adhesives*, 30(5):338–346. 3rd International Conference on Advanced Computational Engineering and Experimenting, Rome, Italy, JUN 22-23, 2009.

Smith, B. J., Kurama, Y. C., and McGinnis, M. J. (2011). Design and Measured Behavior of a Hybrid Precast Concrete Wall Specimen for Seismic Regions. *Journal of Structural Engineering - ASCE*, 137(10):1052–1062.

Souid, A., Delaplace, A., Ragueneau, F., and Desmorat, R. (2009). Pseudodynamic testing and nonlinear substructuring of damaging structures under earthquake loading. *Engineering Structures*, 31(5):1102 – 1110.

Sozen, S. and Guler, M. (2011). Determination of displacement distributions in bolted steel tension elements using digital image techniques. *Optics and Lasers in Engineering*, 49(12):1428 – 1435.

Wei, S. and Xiaoyuan, H. (2009). Experimental studies on application of digital image correlation in measuring field of civil engineering. *Journal of Nanjing University of Aeronautics & Astronautics*, 41(2).

Yoneyama, S., Kitagawa, A., Iwata, S., Tani, K., and Kikuta, H. (2007). Bridge deflection measurement using digital image correlation. *Experimental Techniques*, 31(1):34–40.

Yoneyama, S., Kitagwa, A., Kitamura, K., and Kikuta, H. (2005). Deflection distribution measurement of steel structure using digital image correlation. *Proceedings of the SPIE - The International Society for Optical Engineering*, 5880(1):G1–G8.